

WADD TECHNICAL REPORT 60-84

DO NOT DESTROY  
RETURN TO  
WADD LIBRARY

CATALOGED BY WWAD

59.551

AD-249410

ELECTRICAL PROPERTIES OF  
METAL-LOADED RADOMES

*Lloyd A. Robinson*

*Stanford Research Institute*

FEBRUARY 1960

WRIGHT AIR DEVELOPMENT DIVISION

## NOTICES

When Government drawings, specifications, or other data are used for any purpose other than in connection with a definitely related Government procurement operation, the United States Government thereby incurs no responsibility nor any obligation whatsoever; and the fact that the Government may have formulated, furnished, or in any way supplied the said drawings, specifications, or other data, is not to be regarded by implication or otherwise as in any manner licensing the holder or any other person or corporation, or conveying any rights or permission to manufacture, use, or sell any patented invention that may in any way be related thereto.

★

Qualified requesters may obtain copies of this report from the Armed Services Technical Information Agency, (ASTIA), Arlington Hall Station, Arlington 12, Virginia.

★

Copies of WADD Technical Reports and Technical Notes should not be returned to the Wright Air Development Division unless return is required by security considerations, contractual obligations, or notice on a specific document.

## ELECTRICAL PROPERTIES OF METAL-LOADED RADOMES

*Lloyd A. Robinson*

*Stanford Research Institute*

**FEBRUARY 1960**

Reconnaissance Laboratory  
Contract No. AF33(616)-5539  
Project No. 4161

WRIGHT AIR DEVELOPMENT DIVISION  
AIR RESEARCH AND DEVELOPMENT COMMAND  
UNITED STATES AIR FORCE  
WRIGHT-PATTERSON AIR FORCE BASE, OHIO

## FOREWORD

This report was prepared by Mr. Lloyd A. Robinson of Stanford Research Institute, Menlo Park, California, on Air Force Contract AF33 (616)-5539, under Project Nr. 4161, "Radome Techniques and Components." The contract efforts were accomplished under the cognizance of the Reconnaissance Laboratory, Wright Air Development Center (now designated Wright Air Development Division), with the technical work directed by Lt. Vernon Dunn and Capt. Frank Brown, in turn, as the task engineers. This report covers the period of March 1958 through April 1959.

## ABSTRACT

---

This is the final report on an investigation of the electrical properties of radomes containing metallic inclusions that may serve to reinforce the radome. This work is a continuation of that done on Contract AF 33(616)-3495, and emphasis has been placed on the resonant-wall type of radome.

The resonant-wall radome is described as a thick metal plate perforated by a number of dielectric-filled resonant cavities tuned to the operating frequency of the radome. It is electrically feasible to use this metal plate by itself, or in conjunction with any of several combinations of dielectric layers. Empirical design data are presented for resonant-wall radomes with a dielectric layer  $0.2 \lambda/\sqrt{\epsilon}$  to  $0.6 \lambda/\sqrt{\epsilon}$  thick in contact with a metal plate  $0.4 \lambda/\sqrt{\epsilon}$  to  $1.5 \lambda/\sqrt{\epsilon}$  thick. Here  $\lambda$  is the free-space wavelength, and  $\epsilon$  is the relative dielectric constant of the material filling the cavities and on the surface of the metal plate. Empirical design data are also presented for a metal plate  $0.2 \lambda/\sqrt{\epsilon}$  to  $1.6 \lambda/\sqrt{\epsilon}$  thick that is not covered by dielectric. The measured power transmission and insertion phase delay of three resonant-wall radomes are also presented as functions of the angle of incidence and polarization of the incident waves. Equivalent circuits for resonant-wall radomes are presented, approximate values for the circuit elements are deduced, and the electrical performance calculated from the equivalent circuits is compared with measured performance.

Finally, descriptions are given of the other metal-loaded radomes considered briefly on this contract. These are A-sandwich radomes with wire grids located at the skin-to-core interfaces; radomes containing self-resonant, perforated-metal sheets; and resonant-wall radomes using air-filled, ridge-loaded cavities.

## PUBLICATION REVIEW

The content of this report represents the scientific findings of an Air Force sponsored program. It does not direct any specific application thereof. The report is approved for publication to achieve an exchange and stimulation of ideas.

FOR THE COMMANDER:

  
E. B. WOODFORD  
Technical Director  
Reconnaissance Laboratory

## TABLE OF CONTENTS

---

SECTION	PAGE
I INTRODUCTION . . . . .	1
II RESONANT-WALL RADOMES . . . . .	5
Fundamental Considerations . . . . .	5
Empirical Design Data . . . . .	11
Measured Performance as a Function of Incidence Angle . . . . .	24
Equivalent Circuits of Resonant-Wall Radomes . . . . .	36
III OTHER METAL-LOADED RADOMES . . . . .	59
Ceramic A-Sandwich Radomes . . . . .	59
Resonant Perforated-Metal Sheets . . . . .	65
Resonant-Wall Radomes with Air-Filled Cavities . . . . .	81
IV CONCLUSIONS AND RECOMMENDATIONS . . . . .	85
Conclusions of the Study . . . . .	85
Recommendations for Future Work . . . . .	89
APPENDIX A PARALLEL-PLATE TRANSMISSION-LINE SET-UP FOR MEASURING THE ELECTRICAL PERFORMANCE OF FLAT-STRIP RADOME SAMPLES . . . . .	91
APPENDIX B CHARACTERISTIC ADMITTANCE OF RESONANT-WALL RADOMES . . . . .	103
BIBLIOGRAPHY . . . . .	107

## LIST OF ILLUSTRATIONS

---

Fig. 1	Several Resonant-Wall Radome Configurations . . . . .	2
Fig. 2	Nose Radome of the Resonant-Wall Type Covered with Dielectric . . . . .	3
Fig. 3	Maximum Operating Frequency of Resonant-Wall Radomes; Incidence Angle and Cavity Array as Parameters . . . . .	8
Fig. 4	Maximum Operating Frequency of Resonant-Wall Radomes; Dielectric Constant $\epsilon = \epsilon_2 = \epsilon_3$ as a Parameter . . . . .	8
Fig. 5	Maximum Operating Frequency of Resonant-Wall Radomes; Dielectric Constant $\epsilon_3$ as a Parameter ( $\epsilon_2 = 9$ ) . . . . .	9
Fig. 6	Maximum Operating Frequency of Resonant-Wall Radomes; Dielectric Constant $\epsilon_3$ as a Parameter ( $\epsilon_2 = 1$ ) . . . . .	9
Fig. 7	Resonant-Wall Radome Sample and Waveguide Test Sections . . . . .	12
Fig. 8	Metal Plate Thickness as a Function of Cavity Diameter for Resonant-Wall Radomes Without Surface Dielectric . . . . .	14-15
Fig. 9	Bandwidth and Transmission as Functions of Cavity Diameter for Resonant-Wall Radomes Without Surface Dielectric . . . . .	16
Fig. 10	Bandwidth and Transmission as Functions of Metal-Plate Thickness for Resonant-Wall Radomes Without Surface Dielectric . . . . .	18
Fig. 11	Cavity-Diameter and Bandwidth Contours for Resonant-Wall Radomes with Dielectric in Contact with One Surface . . . . .	19
Fig. 12	Resonant-Wall Radome Sample for Test in a Parallel-Plate Transmission Line .	24
Fig. 13	Measured Transmission and Phase Delay of Resonant-Wall Radome Sample A . .	27-28
Fig. 14	Measured Insertion Loss of Resonant-Wall Radome Sample A . . . . .	30
Fig. 15	Measured Bandwidth and Transmission of Resonant-Wall Radome Sample A . . . .	31
Fig. 16	Measured Transmission and Phase Delay of Resonant-Wall Radome Sample B . .	33-34
Fig. 17	Measured Insertion Loss of Resonant-Wall Radome Sample B . . . . .	35
Fig. 18	Measured Bandwidth and Transmission of Resonant Wall Radome Sample B . . . .	36
Fig. 19	Equivalent Circuit of Resonant Wall Radomes Without Surface Dielectric . .	37
Fig. 20	A Factor Used in Calculating the Characteristic Admittance of Resonant-Wall Radomes . . . . .	40
Fig. 21	Calculated Performance of a Resonant Wall Radome Sample for Perpendicularly Polarized Waves . . . . .	44
Fig. 22	Calculated Performance of a Resonant-Wall Radome Sample for Parallel-Polarized Waves . . . . .	45
Fig. 23	Comparison of Calculated and Measured Performance of Resonant Wall Radome Sample A (Simplest Circuit) . . . . .	47
Fig. 24	Comparison of Calculated and Measured Performance of Resonant-Wall Radome Sample B (Simplest Circuit) . . . . .	48
Fig. 25	Comparison of Calculated and Measured Performance of Resonant-Wall Radome Samples A and B for Perpendicularly Polarized Waves (Modified Circuit) . .	50

▼

LIST OF ILLUSTRATIONS *Continued*

Fig. 26	Equivalent Circuit of Resonant-Wall Radomes with Dielectric in Contact With One Surface . . . . .	52
Fig. 27	Comparison of Calculated and Measured Performance of Resonant-Wall Radome Sample C . . . . .	55
Fig. 28	Calculated Bandwidth, Reflection, and Transmission of Resonant-Wall Radome Sample C . . . . .	57
Fig. 29	4-Sandwich Radomes Containing Perforated Metal Sheets and Wire Grids . . . . .	60
Fig. 30	Transmission Curves for Metal-Loaded 4-Sandwich Radomes ( $\epsilon_r = 4$ ) . . . . .	61
Fig. 31	Transmission Curves for Metal-Loaded 4-Sandwich Radomes ( $\epsilon_r = 2$ ) . . . . .	61
Fig. 32	Approximate Wire Grid Dimensions for Radomes D, E, and G . . . . .	64
Fig. 33	Various Ridge-Loaded Apertures with Centers Forming Hexagonal Arrays . . . . .	67
Fig. 34	Ridge-Loaded Circular Aperture Shape Used for Samples . . . . .	68
Fig. 35	Cutoff Wavelength of Quadruply Ridged Circular Waveguide . . . . .	69
Fig. 36	Waveguide Cavity Using Ridge-Loaded Circular Waveguide . . . . .	70
Fig. 37	Correction on Cutoff Wavelength Due to the Presence of Fillets at Ridge Bases .	71
Fig. 38	Block Diagram of Equipment to Measure Transmission vs. Frequency . . . . .	72
Fig. 39	Flat-Strip Samples of Resonant Perforated-Metal Sheets . . . . .	72
Fig. 40	Measured Resonance Frequency of Flat Metal Strips Perforated by Circular Apertures . . . . .	74
Fig. 41	Measured Resonance Frequency and Bandwidth of Flat Metal Strips Perforated by Ridge-Loaded Apertures . . . . .	76
Fig. 42	Flat-Panel Sample of a Resonant Perforated-Metal Sheet . . . . .	77
Fig. 43	Measured Resonance Frequency and Bandwidth of the Flat Panel Perforated Metal Sheet . . . . .	78
Fig. 44	Measured Transmission vs. Incidence Angle for the Flat Panel Perforated Metal Sheet . . . . .	79
Fig. 45	Summary of Resonance-Frequency Data for Resonant Perforated Metal Sheet Samples . . . . .	82
Fig. 46	Parallel-Plate Transmission-Line Set-Up . . . . .	91
Fig. 47	Block Diagram of the Parallel-Plate Transmission-Line Set-Up . . . . .	92
Fig. 48	Coordinate System for Horizontally Polarized Waves in the Parallel-Plate Transmission-Line . . . . .	96
Fig. 49	Rectangular Waveguides Terminated by Circular Waveguides . . . . .	105

## LIST OF TABLES

---

Table 1	Dimensions of Resonant-Wall Radome Samples Tested in Waveguide . . . . .	13
Table 2	Dimensions of Resonant-Wall Radome Samples A and B in Physical Units . . . . .	26
Table 3	Dimensions of Resonant-Wall Radome Samples A and B in Terms of Wavelength . . . . .	25
Table 4	Dimensions of Resonant-Wall Radome Sample C in Terms of Wavelength . . . . .	56
Table 5	Design Parameters for Metal-Loaded A-Sandwich Radomes with $\epsilon_r = 4$ . . . . .	62
Table 6	Design Parameters for Metal-Loaded A-Sandwich Radomes with $\epsilon_r = 2$ . . . . .	62
Table 7	Dimensions of Flat-Strip Samples Perforated by Circular Apertures . . . . .	73
Table 8	Dimensions of Samples Perforated by Ridge-Loaded Circular Apertures . . . . .	75
Table 9	Dimensions of Parallel-Plate Transmission-Line Set-Up . . . . .	93

## SECTION I

### INTRODUCTION

Radomes mounted on high-speed aircraft and missiles must operate at high temperatures and be able to withstand severe rain-erosion conditions. These needs have resulted in a trend toward the use of inorganic materials such as ceramics, glass and glass-bonded mica in the construction of radomes. Such materials have already been used successfully for some missile radomes, but their tensile strength does not appear to be adequate to withstand the severe stresses that will be encountered in the large radomes required for aircraft of the future. As a complement to the search for high-strength radome materials, it is appropriate to investigate methods of increasing the strength of currently available inorganic radome materials. Therefore, the present study is being carried out to determine the electrical performance of radomes containing various metal inclusions that may serve as reinforcing members.

During a previous contract it was shown that several types of metal-loaded radomes were promising from the electrical standpoint.<sup>1\*</sup> Of these, the resonant-wall radome appeared to be the most promising from the mechanical standpoint since a relatively large percentage of the radome is metal. The basic resonant-wall radome consists of a thick metal plate perforated by dielectric-filled resonant cavities all tuned to the same frequency, as shown in Figs. 1(a) and 1(e). It is also electrically feasible to use the perforated metal plate in conjunction with layers of dielectric, as indicated in Figs. 1(b), 1(c), and 1(d).

---

\* References are listed at the end of the report.

Manuscript released by the author 4 April 1960 for publication as a WADD Technical Report.

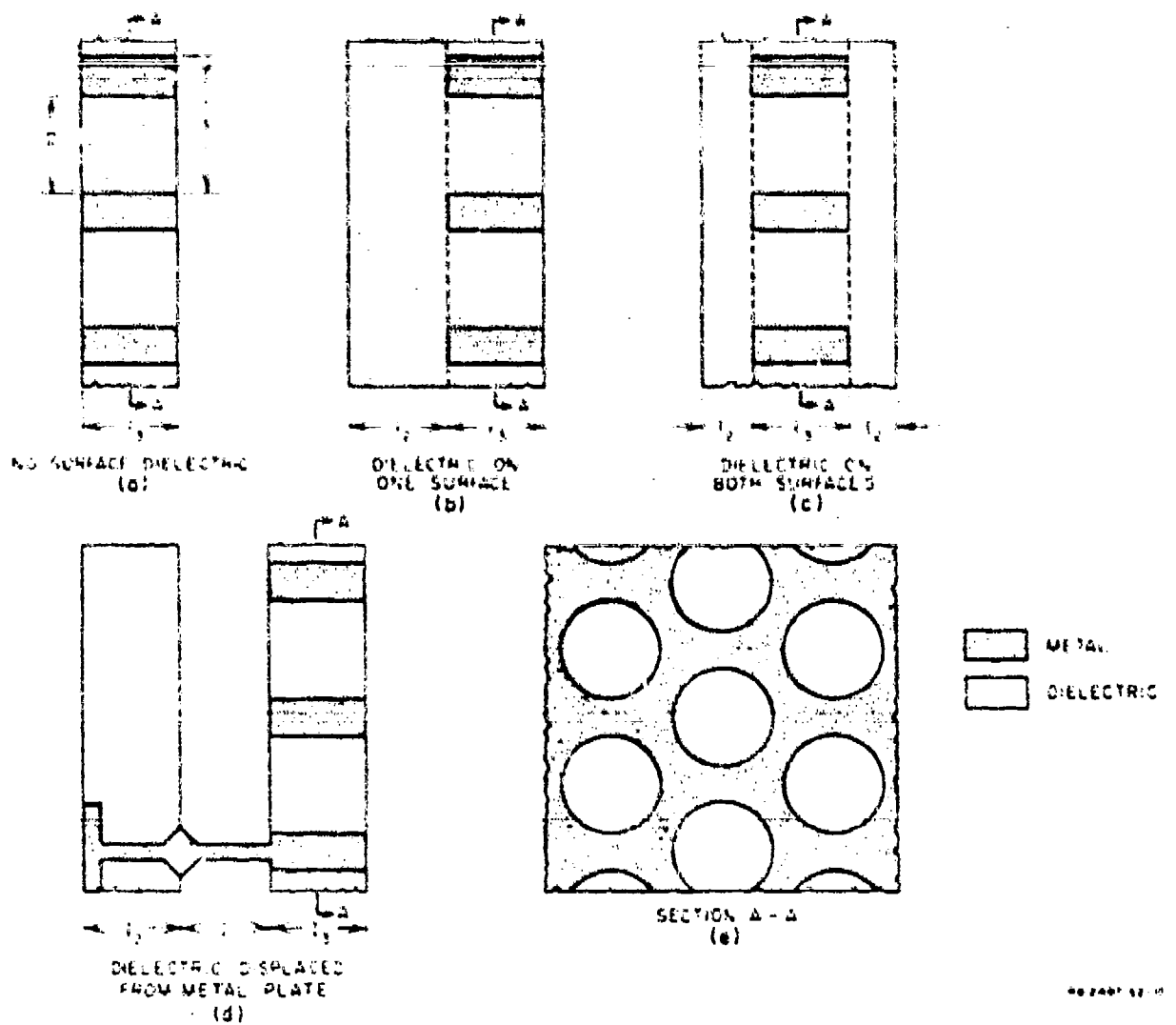


FIG. 1  
SEVERAL RESONANT-WALL RADOME CONFIGURATIONS

A nose radome of the resonant-wall type might be similar to that shown in Fig. 2.\* Except for the metal tip and the mounting ring, the outer surface would be covered with solid dielectric to provide protection against rain erosion. It has been suggested by WADC that a resonant-wall radome without the dielectric cover might have poor rain-erosion resistance because of the many dielectric-to-metal joints exposed. No dielectric is shown on the inner surface of the metal plate, since there is no mechanical reason to have it there. Under aerodynamic loading, a radome wall is subjected to both compressive and tensile loads. Since inorganic dielectrics

\* Hexagonal and square arrays of cavities can be laid out on conical radomes with total included vertex angles of 19.2 and 29.0 degrees, respectively. For other radome shapes the cavity layout would depart from a regular hexagonal or square array.

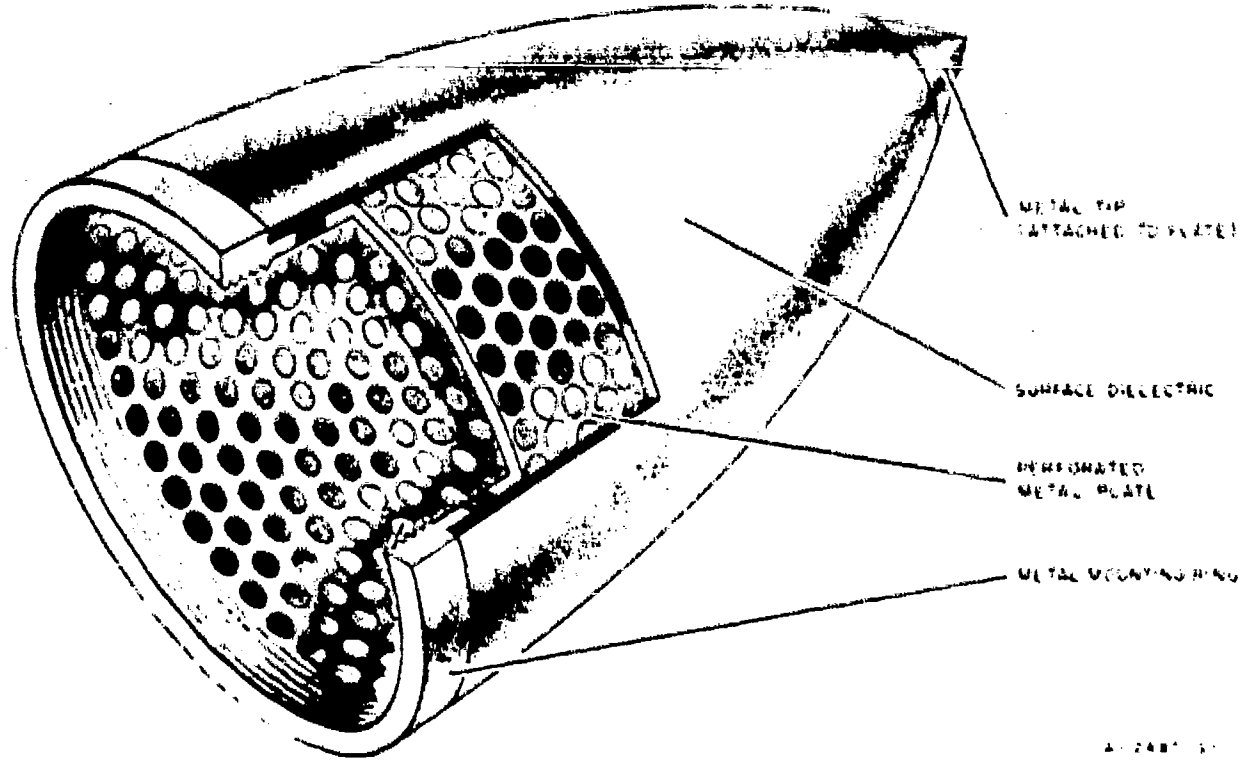


FIG. 2  
NOSE RADOME OF THE RESONANT-WALL TYPE COVERED WITH DIELECTRIC

have greater compressive strength than tensile strength, there might be some advantage in using the metal structure to place the dielectric shell or shells under compression, i.e., to pre-stress the radome.

In this report, empirical design data will be presented specifically for the radome configurations illustrated in Figs. 1(a) and 1(b). Sufficient information is contained in the data that a limited number of radomes of the configurations shown in Figs. 1(c) and 1(d) can also be designed. In addition to the design data, the measured power transmission and insertion phase delay are presented for one radome using the configuration of Fig. 1(a) operated at its first-order and second-order resonances, and for one radome using the configuration of Fig. 1(b). The use of approximate equivalent circuits for calculating the electrical performance of resonant-wall radomes is discussed, and the calculated performance of the above-mentioned radome samples is compared with the measured performance. In addition to the resonant-wall radomes with dielectric-filled cavities, which are the major subject of this report, brief consideration is given

to the following metal-loaded radomes: A-sandwich radomes containing wire grids, radomes containing resonant perforated-metal sheets, and resonant-wall radomes using air-filled, ridge-loaded cavities.

The metal inclusions considered here consist of elements whose center-to-center spacing is sufficiently small that only the principal transmitted and reflected waves need be considered, i.e., the metal inclusions do not radiate diffracted waves. Greater spacing for the loading elements is not considered since it is felt that diffracted waves would decrease the transmission efficiency of the radome, contribute to the side-lobe level of the antenna used with the radome, and contribute to the boresight error of the radome.

## SECTION II

### RESONANT-WALL RADOMES

#### FUNDAMENTAL CONSIDERATIONS

In order to obtain high transmission through a thick perforated metal plate it is necessary that the diameter of each aperture be sufficiently large that the dominant  $TE_{11}$  circular-waveguide mode can propagate through the apertures. Each length of circular waveguide, together with the reactive discontinuities at its ends, forms a resonant cavity that will have high transmission efficiency at its resonant frequency. Thus, the operating frequency must be above the cut-off frequency,  $f_{ce}$ , for the dominant mode as given by Eq. (1):

$$f_{ce} = \frac{11.80}{1.706\epsilon_3 D} \text{ kilomegacycles,} \quad (1)$$

where

$D$  = diameter of the cavities in inches

$\epsilon_3$  = relative dielectric constant of the material in the cavities.

In order for the resonant cavities to function as single-mode transmission lines, the first higher-order  $TM_{01}$  mode should be below cut-off. This condition requires

$$f < \frac{11.80}{1.306\epsilon_3 D} \text{ kilomegacycles} \quad (2)$$

Even if the  $TM_{01}$  mode can propagate in the cavities, however, it will not affect the radome performance unless the operating frequency of the radome is near a resonance of this mode. Since the  $TE_{11}$  and  $TM_{01}$  modes have different guide wavelengths, and since the two modes see different reactive discontinuities at the surfaces of the radome, it is possible in principle to separate their resonances by proper design. Thus, it should be possible to exceed the inequality of Eq. (2) slightly. It is not possible to

calculate the separation between the resonances of the two modes, however, since the reactive discontinuities at the radome surface differ by an unknown amount for the two modes. For one resonant-wall radome, designated as Radome B later in this report, the inequality of Eq. (2) was exceeded by about 25 percent, and evidence was observed of slight interference by the  $TM_{01}$  mode.

Another condition to be fulfilled by a resonant-wall radome is that the center-to-center spacing be sufficiently small that none of the incident energy will be transferred from the main beam of the antenna to diffracted waves. Diffracted waves are undesirable since they reduce the gain of the antenna and raise the side-lobe level, and may contribute to the boresight error of the radome. When the well-known criteria for no diffraction from a uniformly-spaced linear array are generalized for a two-dimensional, plane array of apertures, Eq. (3) results:\*

$$A \frac{s}{\lambda} < \frac{1}{\sqrt{\epsilon_2} + \sin \theta} \quad (3)$$

where

$s$  = center-to-center spacing of the cavities

$\lambda$  = free-space wavelength

$\epsilon_2$  = relative dielectric constant of material in contact with the surface of the metal plate

$\theta$  = angle of incidence of the impinging wave measured outside the radome with respect to the normal to the radome surface

$A = \begin{cases} 1 & \text{for cavities arranged in a square array} \\ 0.5\sqrt{3} & \text{for cavities arranged in a hexagonal array.} \end{cases}$

The upper frequency limit,  $f_{max}$ , at which a resonant-wall radome can be designed to operate satisfactorily will be taken as the highest frequency for which both Eqs. (2) and (3) are satisfied; and the lower frequency limit is  $f_{cc}$ . The maximum frequency bandwidth within which a

\* Equation (3) expresses the condition for no diffraction within a dielectric layer in contact with the perforated metal plate. If Eq. (3) is not satisfied, but the corresponding equation with  $\epsilon_2$  set equal to unity is satisfied, the waves diffracted in the dielectric will not radiate into space, but will be totally reflected at the dielectric-to-air interface. Even though these waves are not radiated directly, they may degrade the radome performance by exciting surface waves in the dielectric layer.

resonant-wall radome can be designed to operate is  $f_{max}/f_{co}$ , and is given by Eq. (4) or Eq. (5), whichever gives the smaller bandwidth:

$$\frac{f_{max}}{f_{co}} = \frac{1.706}{1.306} - \xi + 1.306 - \xi \quad (4)$$

$$\frac{f_{max}}{f_{co}} = \frac{1.706\sqrt{\epsilon_3}}{A(\sqrt{\epsilon_2} + \sin \theta)} \cdot \frac{D}{s} - \xi \quad (5)$$

where  $\xi$  is a negligibly small positive quantity such that the inequalities of Eqs. (2) and (3) are just satisfied

In practice, the actual usable bandwidth of a particular resonant-wall radome will be smaller than the limits specified by Eqs. (4) and (5). It will be shown later in this report that a resonant-wall radome designed to operate far from  $f_{co}$  will have a larger usable bandwidth than one designed to operate near  $f_{co}$ , since the electrical thickness of the cavities varies rapidly with frequency at frequencies near  $f_{co}$ . Thus, it will be assumed for the purposes of the following discussion that it is desirable to design the radome to have a resonance frequency as far from  $f_{co}$  as possible.

The frequency band within which the radome may be designed to operate changes with various radome parameters as shown in Figs. 3 through 6. In these figures, the horizontal line represents the maximum frequency for single-mode propagation in the cavities,\* and the sloping line represents the maximum frequency for no multiple scattering within the dielectric. The area below and to the left of these curves represents the region within which the radome may be designed to operate. Figure 3 shows that for a given ratio of wall thickness (between cavities) to cavity spacing, the ratio  $f_{max}/f_{co}$  is larger for the cavities in a hexagonal array than for the cavities in a square array, and for either cavity configuration, the ratio  $f_{max}/f_{co}$  is increased only slightly by reducing the maximum angle of incidence from 85 degrees to 60 degrees †. Figure 3 also illustrates that the mechanical requirement for thick walls between the cavities is

\* As has already been mentioned, it is possible to operate a resonant-wall radome with more than one mode above cut-off. If the results obtained with Radome B can be generalized to apply to all resonant-wall radomes, then extrapolation of the sloping lines to the tops of Figs. 3 through 6 would be justified.

† This is not to be confused with the fact that the usable bandwidth of the radome, within which the transmission coefficient is greater than a specified minimum value, will increase significantly as the maximum angle of incidence is reduced from 85 to 60 degrees.

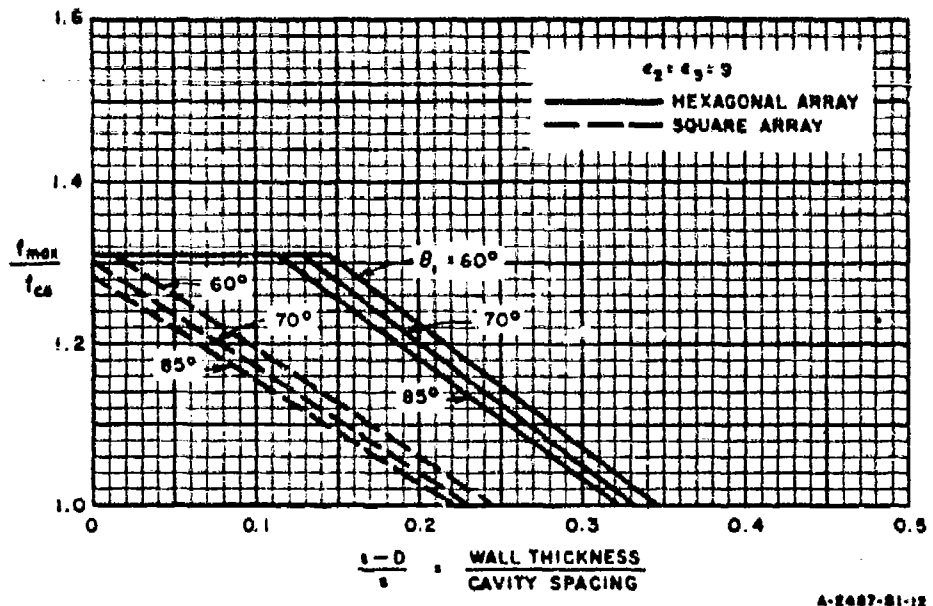


FIG. 3

MAXIMUM OPERATING FREQUENCY OF RESONANT-WALL RADOMES;  
INCIDENCE ANGLE AND CAVITY ARRAY AS PARAMETERS

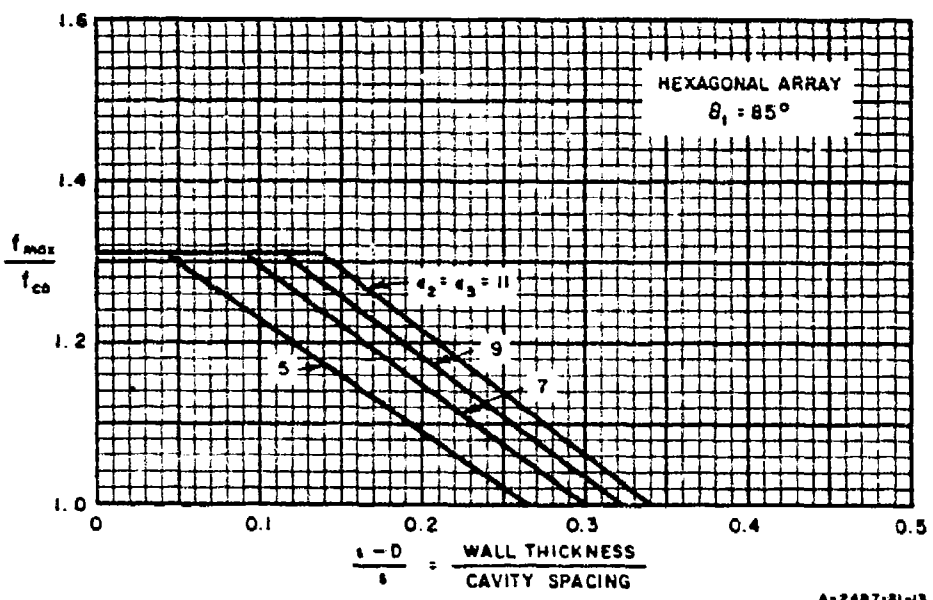


FIG. 4

MAXIMUM OPERATING FREQUENCY OF RESONANT-WALL RADOMES;  
DIELECTRIC CONSTANT  $\epsilon = \epsilon_2 = \epsilon_3$  AS A PARAMETER

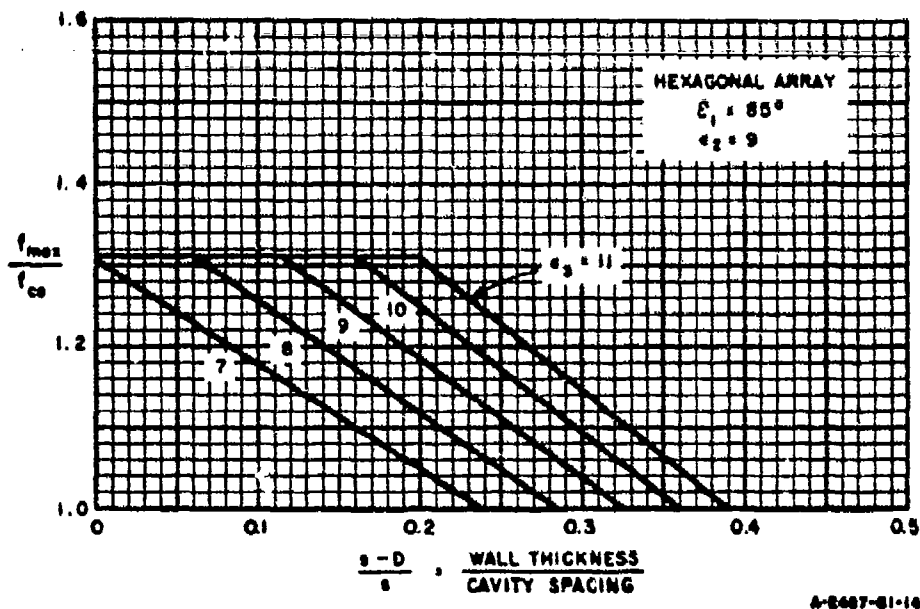


FIG. 5  
 MAXIMUM OPERATING FREQUENCY OF RESONANT-WALL RADOMES;  
 DIELECTRIC CONSTANT  $\epsilon_3$  AS A PARAMETER ( $\epsilon_2 = 9$ )

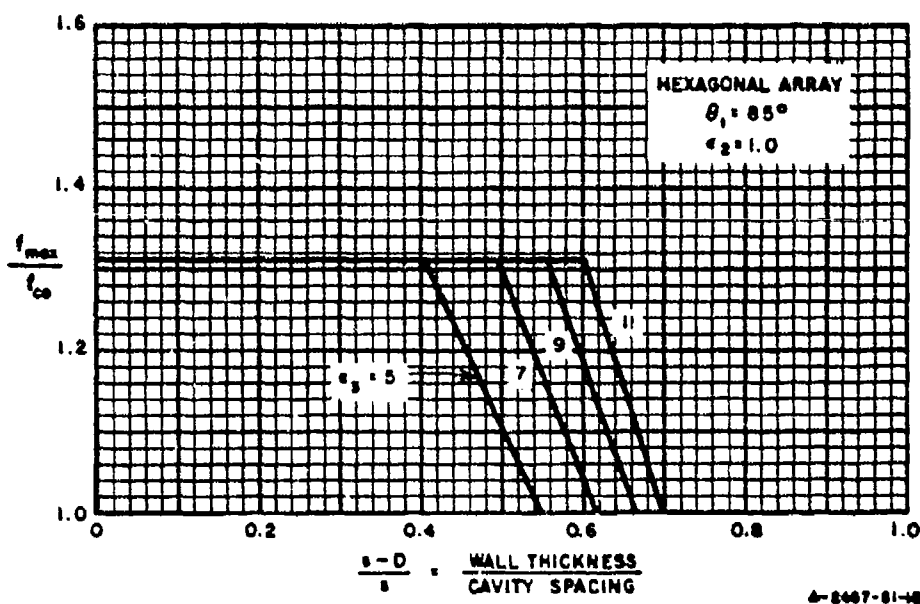


FIG. 6  
 MAXIMUM OPERATING FREQUENCY OF RESONANT-WALL RADOMES;  
 DIELECTRIC CONSTANT  $\epsilon_3$  AS A PARAMETER ( $\epsilon_2 = 1$ )

not compatible with the electrical requirement for the frequency bandwidth to be as large as possible. From this figure one can conclude that the usable bandwidth of a resonant-wall radome will be increased by using a hexagonal array of cavities instead of a square array, by restricting the maximum angle of incidence, and by decreasing the ratio of wall thickness to cavity spacing.

It is shown in Fig. 4 that for an  $(s - D)/s$  ratio greater than about 0.15, the ratio  $f_{\text{max}}/f_c$  increases as the dielectric constant of the material filling the cavities and covering the surface of the metal plate is increased. Caution must be used however, in drawing conclusions regarding the effect of changing  $\epsilon_2$  and  $\epsilon_3$  on the usable bandwidth of resonant-wall radomes since there are two effects to consider. One effect is that as the dielectric constant is increased, the radome can be operated farther from the cut-off frequency of the cavities so that the guide wavelength in the cavities (and thus the electrical thickness of the cavities) does not change as rapidly with frequency. This effect tends to increase the bandwidth of the radome as the dielectric constant is increased. The other effect is that as the dielectric constant increases, the difference between the impedance of the radome and that of free space increases, which tends to reduce the bandwidth of the radome. For resonant-wall radomes operating close to the cut-off frequency of the cavities, the first effect is likely to dominate, and for radomes operating far from the cut-off frequency of the cavities, the second effect is likely to dominate.\*

Changing only the dielectric constant,  $\epsilon_3$ , of the material filling the cavities has a greater effect on  $f_{\text{max}}/f_c$ , than changing both  $\epsilon_2$  and  $\epsilon_3$  together, as can be seen by comparing Figs. 4 and 5. This suggests that for a given surface dielectric chosen on the basis of mechanical properties, the widest bandwidth might be obtained by using a material of different dielectric constant to fill the cavities. It is not obvious whether  $\epsilon_3$  should be greater or less than  $\epsilon_2$  since the same problem of mixed effects discussed with respect to Fig. 4 also occurs here.

When the resonant-wall radome has one or both surfaces covered with dielectric, the cavities must be packed much closer together (in order to avoid exciting diffracted waves in the dielectric) than when the surfaces of the resonant-wall radome are not covered with dielectric, as can be

---

\* The usable bandwidth for a given minimum transmission efficiency will also depend on the dissipation loss within the dielectric, as well as on the dielectric constant.

seen by comparing Figs. 5 and 6 \* Thus, the walls between the cavities can be made thicker when the surfaces of the metal plate are not in direct contact with layers of dielectric than they can when the surfaces are in direct contact with dielectric layers.

## EMPIRICAL DESIGN DATA

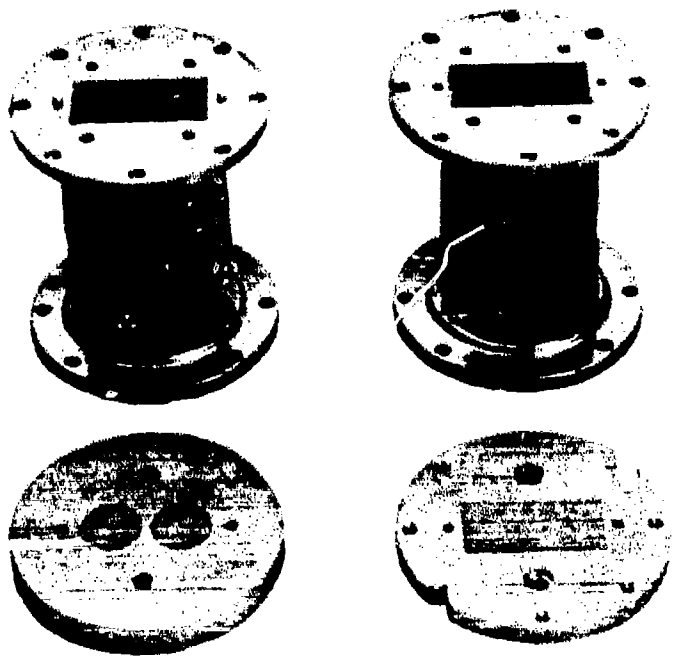
### MEASUREMENT TECHNIQUE

The insertion loss of several radome samples mounted in waveguide was measured as a function of frequency by conventional techniques. Some of the samples had a dielectric layer on one surface of the metal plate, while the rest of the samples did not have a dielectric layer on either surface. The data showed the way in which resonance frequency and bandwidth depend on the thickness of the metal plate and on the thickness of the surface dielectric. Only one value of dielectric constant, and one value of wall thickness between cavities was used in obtaining these data. Waveguide was used in these measurements since the samples could be smaller and more accurate data could be obtained than in free space; however, waveguide is subject to the limitations that only perpendicularly polarized waves are readily obtainable, and for a given waveguide width only one incidence angle can be obtained at a given frequency. The data taken with waveguide samples are intended to show what radome dimensions give the desired resonance frequency and bandwidth for perpendicularly polarized waves incident at wide angles. The electrical performance as a function of incidence angle and polarization must be determined using other techniques and larger samples.

One of the resonant-wall radome samples is shown partially disassembled at the bottom of Fig. 7. When inserted between the flanges of the waveguide shown at the top of Fig. 7, the cavities in the sample are mirrored in the walls of the waveguide so that the sample is equivalent to an infinite plane sample with the cavities in a square array. The wave incident on the sample is equivalent to two plane waves polarized perpendicular to the plane of incidence at angles  $\theta$  and  $-\theta$ , as explained in Appendix B of Ref. 1. The angle of incidence is related to the width,  $a$ , of the waveguide and the free-space wavelength,  $\lambda$ , by Eq. (6):

$$\sin \theta = \frac{\lambda}{2a} . \quad (6)$$

\* Note that Fig. 6 has a different scale factor on the abscissa than do Figs. 3, 4, and 5.



P-2487-SI-16

FIG. 7  
RESONANT-WALL RADOME SAMPLE AND  
WAVEGUIDE TEST SECTIONS

To obtain proper mirror-imaging of the cavities into a square array a special cross-section waveguide was fabricated, the two halves of which are shown in Fig. 7. At the center, where the radome samples are inserted, the width is exactly twice the height, and the inside dimensions taper to those of standard 2- by 1-inch waveguide at the ends.

The dimensions of the samples are shown in Table 1. Supramica 500 was used as the dielectric since this is a high-dielectric-constant material that can be readily machined. For simplicity, a square array of cavities was used since a hexagonal array cannot be mirrored properly in the waveguide walls without placing metal walls through some of the cavities. Since the bandwidth of resonant-wall radomes is narrowest for perpendicularly polarized waves incident at wide angles, the samples were made with resonance frequencies sufficiently low that the incidence angles were about 60 degrees.

TABLE I  
DIMENSIONS OF RESONANT-WALL RADOME SAMPLES TESTED IN WAVEGUIDE

Arrangement of cavities	Square array
Diameter of cavities, $D$	0.818 inch
Center-to-center spacing of cavities, $s$	0.936 inch
Ratio of $(s - D)/s$	0.126
Percent of metal plate replaced by dielectric	60 percent
Thickness of metal plate, $t_1$	0.5 to 2.0 inch
Thickness of surface dielectric, $t_2$	0.3 to 0.7 inch
Dielectric in cavities and on surface.	
Material	Suprasilica 500
Relative dielectric constant, $\epsilon$	6.4*
Loss tangent, $\tan \delta$	0.0033*
Cut-off frequency of cavities	3.35 kHz
Range of resonance frequencies	3.4 to 6.4 kHz
Inside cross section dimensions of special waveguide:	
Near radome sample	0.936 by 1.872 inch
At ends connecting to standard waveguide	0.872 by 1.872 inch

\* Values measured with the grain visible in the material perpendicular to the electric field. The value  $\epsilon = 6.9$  measured with the grain parallel with the electric field is in closer agreement with the value given by von Hippel.<sup>2</sup>

#### RESONANT-WALL RADOMES WITHOUT SURFACE DIELECTRIC

Data were taken at the first-order and second-order resonances of the samples that had no dielectric layer on either surface of the metal plate but had dielectric within the cavities. At the first-order resonance, the radome is approximately one-half guide-wavelength thick measured in the circular waveguides, thus the radome is somewhat analogous to a conventional half-wavelength radome. At the second-order resonance, the radome is approximately one guide-wavelength thick, analogous to a conventional full-wavelength radome.

The lower curve in Fig. 8 shows the required thickness,  $t_1$ , of the metal plate as a function of the diameter,  $D$ , of the cavities in the metal plate for the radome operated at its first-order resonance frequency. Each of the cavities is a length of circular waveguide through which energy is transferred in the dominant  $TE_{11}$  circular-waveguide mode. The cavities are somewhat less than one-half  $\lambda_{g3}$  thick because of the reactive discontinuities present at the air-to-radome interfaces. Here  $\lambda_{g3}$  is the guide wavelength of the  $TE_{11}$  mode in the cavities and is given by Eq. (7):

$$\lambda_{g3} = \frac{\lambda_3}{\sqrt{1 - \left(\frac{\lambda_3}{1.706 D}\right)^2}} \quad (7)$$

where  $\lambda_3 = \lambda/\sqrt{\epsilon_3}$  = the wavelength measured in the dielectric.

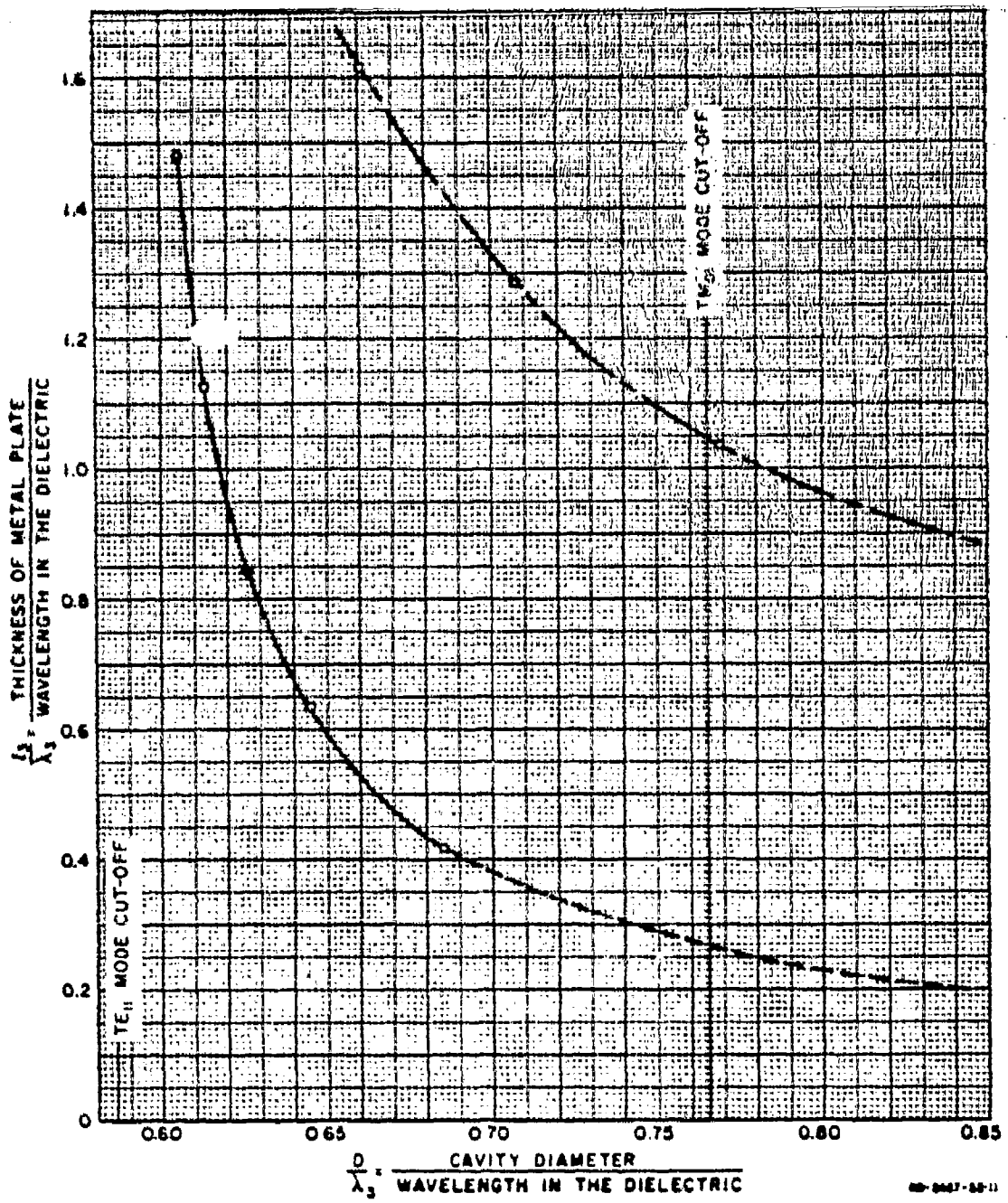


FIG. 8

METAL PLATE THICKNESS AS A FUNCTION OF CAVITY DIAMETER FOR RESONANT-WALL RADOMES WITHOUT SURFACE DIELECTRIC

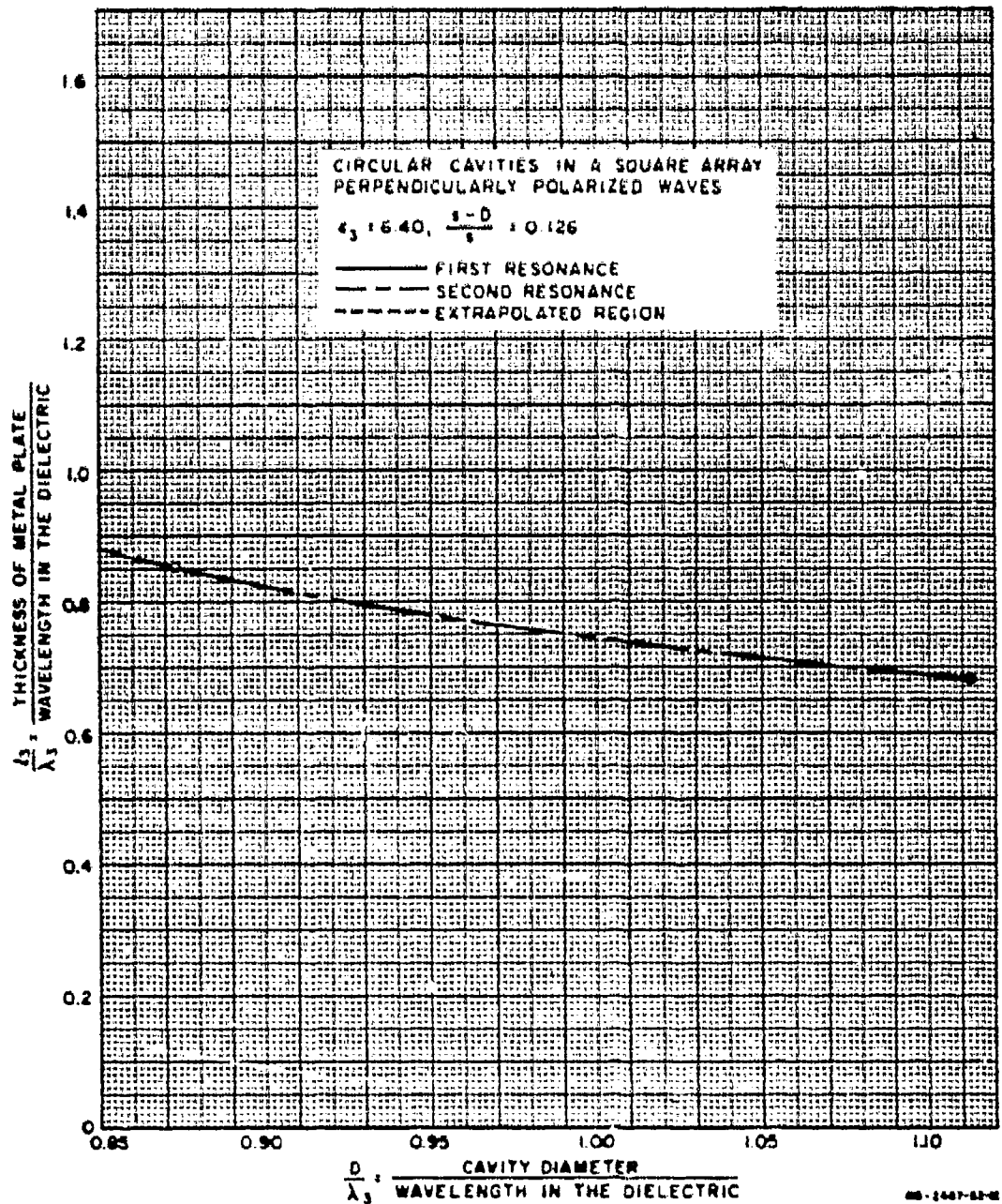


FIG. 8 (Continued)

METAL PLATE THICKNESS AS A FUNCTION OF CAVITY DIAMETER FOR RESONANT-WALL RADOMES WITHOUT SURFACE DIELECTRIC

Since the guide wavelength decreases as the cavity diameter is increased, the metal plate thickness required for the radome to be resonant at a given frequency also decreases as the cavity diameter is increased. For a given cavity diameter and operating frequency, other values for the thickness of the metal plate can be obtained by increasing the length of the cavities by  $n\lambda_g/2$ , where  $n$  is any positive integer. Measured values of metal plate thickness for the second-order resonance, i.e.,  $n = 1$ , are given by the upper curve in Fig. 8.\* The particular incidence angle at which these curves apply for each value of  $D/\lambda_g$  is shown by the lower curve in Fig. 9.

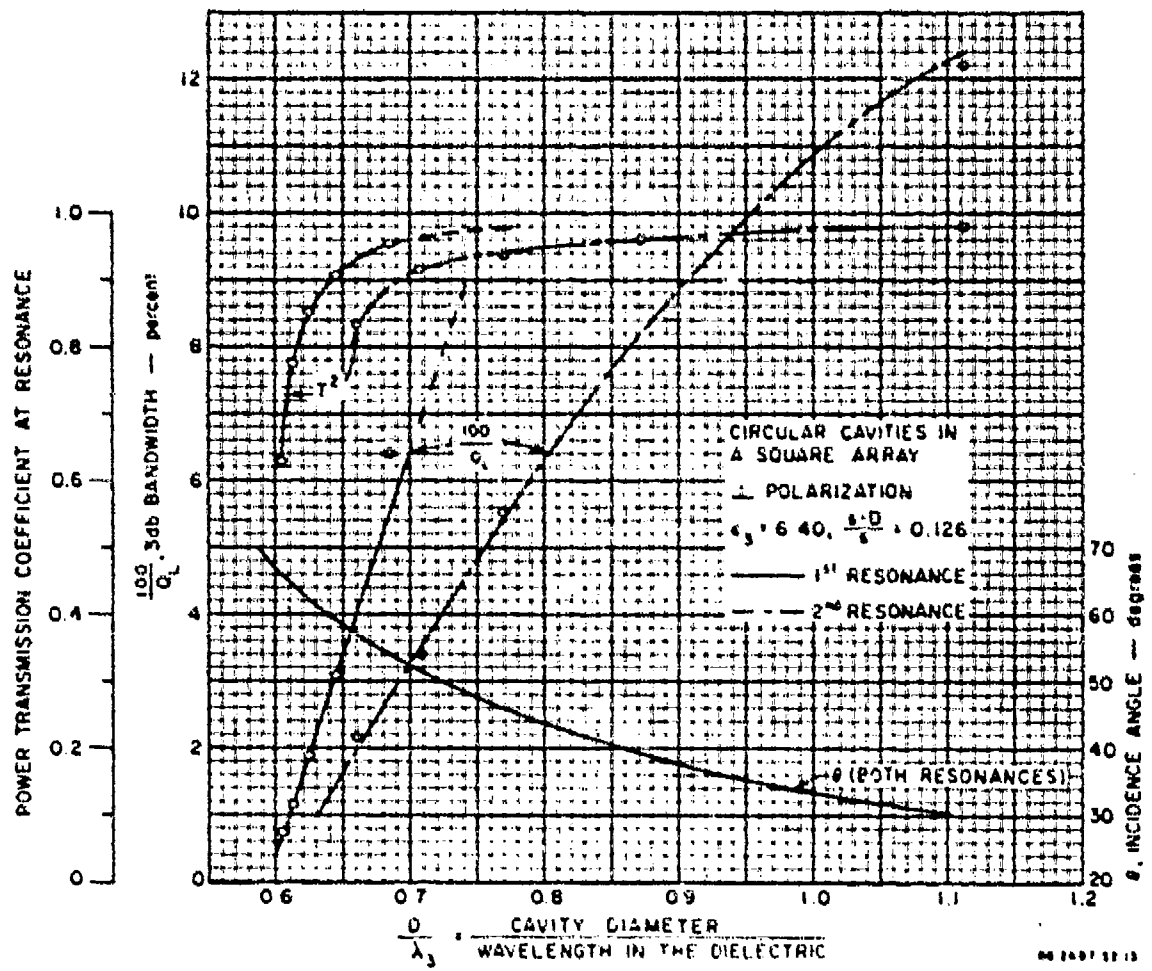


FIG. 9  
BANDWIDTH AND TRANSMISSION AS FUNCTIONS OF CAVITY DIAMETER FOR RESONANT-WALL RADOMES WITHOUT SURFACE DIELECTRIC

\* The extrapolated portion of the lower curve in Fig. 8 was obtained by subtracting one-half guide-wavelength from the upper curve.

As the cavity diameter is increased, the guide wavelength becomes less frequency-sensitive, because the resonant frequency of the radome is farther from the cut-off frequency for the  $TE_{11}$  mode. Therefore, the electrical length of the cavities, defined as  $l_y/\lambda_{g1}$ , becomes less frequency-sensitive as the cavity diameter is increased. In addition, the reactive discontinuities at the ends of the cavities probably decrease as the cavity diameter is increased. As a result of these effects, the bandwidth of resonant-wall radomes, when operated at either the first- or the second-order resonance, increases as the cavity diameter increases. The curves of Fig. 9 show that near the cut-off of the  $TE_{11}$  mode the bandwidth is nearly a linear function of cavity diameter.

At a given design frequency, if the cavity diameter is fixed and the metal-plate thickness is increased by  $\lambda_{g1}/2$  to obtain the second-order resonance, Fig. 9 shows that the resulting bandwidth is approximately half that for the first-order resonance. Although a given change in frequency results in the same percent change in electrical length of the cavities at both resonances, a larger change in terms of degrees occurs for the radome operated at the second-order resonance. This situation is analogous to the decrease in bandwidth resulting if the thickness of a conventional half-wavelength radome is increased to obtain a full-wavelength radome. Corresponding to the narrower bandwidth, the transmission coefficient is smaller at the second-order resonance than at the lowest-order resonance.

On the other hand, if—at a given design frequency—the metal-plate thickness is fixed and the radome is tuned to the first-order and the second-order resonances by varying the cavity diameter, the situation is more complex. The electrical length,  $l_y/\lambda_{g1}$ , of the cavities is greater at the second-order resonance, which tends to reduce the bandwidth; however, the guide wavelength is less frequency sensitive at the second-order resonance since the cavities are larger in diameter, which tends to increase the bandwidth. This latter factor has the greatest influence on the bandwidth since Fig. 10 shows that for a fixed metal-plate thickness, wider bandwidth and higher transmission are obtained at the second-order resonance than at the first-order resonance.

Resonant-wall radomes of the configuration illustrated in Fig. 1(d) can also be designed using the data presented in Fig. 8 provided that the layer of dielectric is a conventional half-wavelength radome. It would also be necessary for the spacing between the dielectric layer and the metal plate to be an appreciable fraction of the cavity spacing so that

the local fields at the surface of the metal plate would not extend into the dielectric layer significantly. If these conditions are fulfilled, both the metal plate and the dielectric sheet will be well matched as individual units, and the spacing between them will not be a critical dimension. The bandwidth of this combination would be only slightly less than that shown in Figs. 9 and 10, since the bandwidth of the perforated metal plate is significantly less than that of a half-wavelength radome. The transmission coefficient of the combination at resonance would be approximately the product of the transmission coefficients of the perforated metal plate and of the dielectric layer.

#### RESONANT-WALL RADOMES WITH DIELECTRIC ON ONE SURFACE

The data for the radome samples with dielectric on one surface are summarized in Fig. 11. In this figure, the solid lines are contours of constant cavity diameter, and the dashed lines are contours of constant 3-db bandwidth. The curves of Fig. 11 are normalized so that they can be

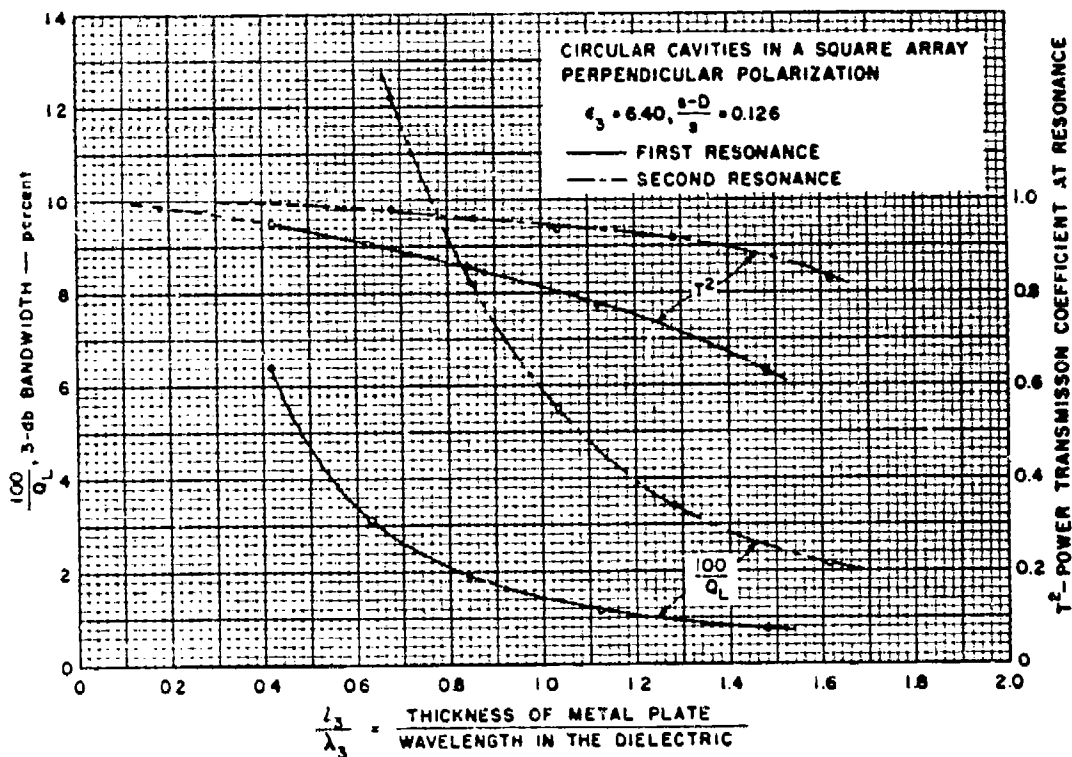


FIG. 10

BANDWIDTH AND TRANSMISSION AS FUNCTIONS OF METAL-PLATE THICKNESS FOR  
 RESONANT-WALL RADOMES WITHOUT SURFACE DIELECTRIC

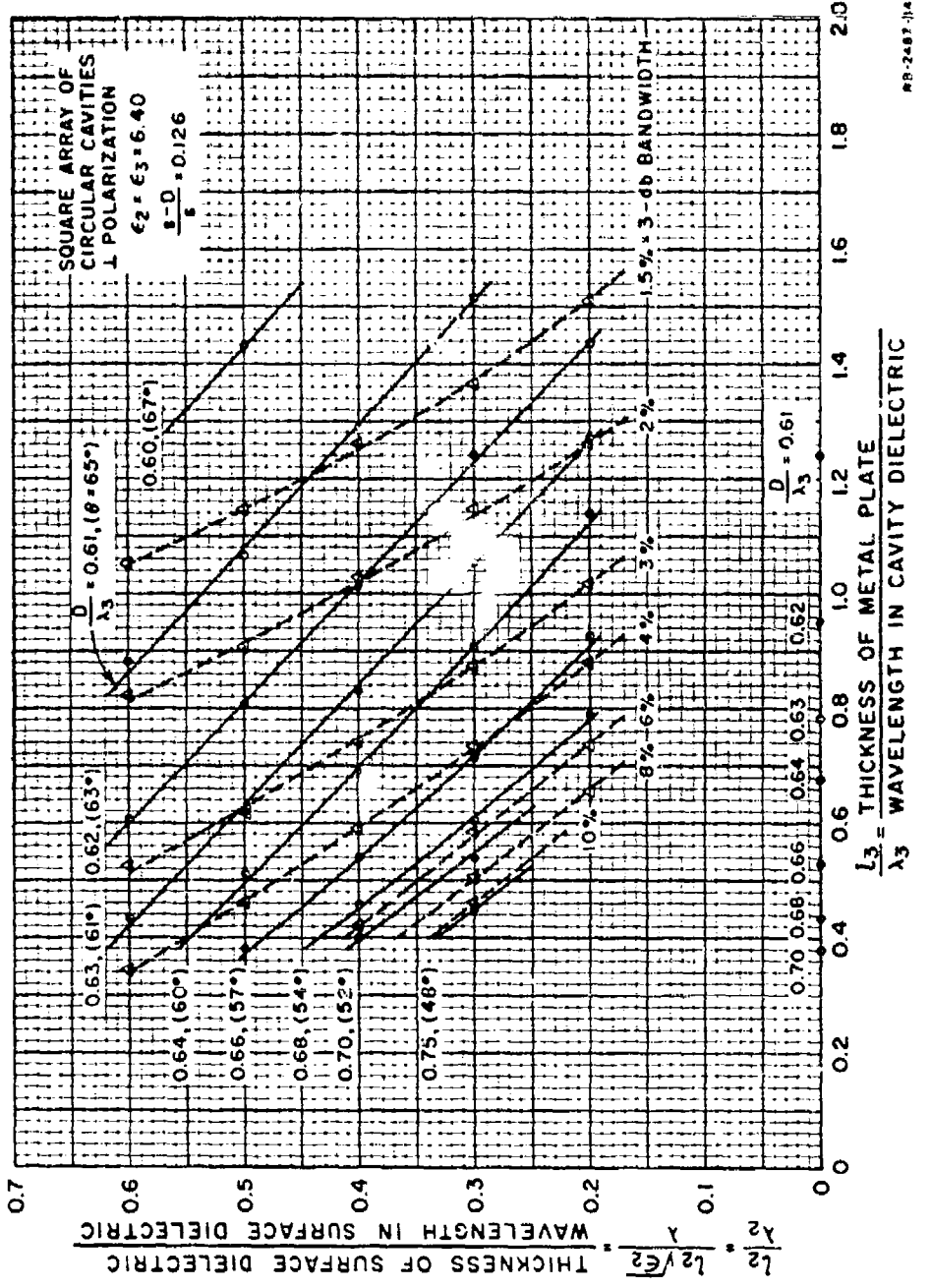


FIG. 11

CAVITY-DIAMETER AND BANDWIDTH CONTOURS FOR RESONANT-WALL RADOMES  
WITH DIELECTRIC IN CONTACT WITH ONE SURFACE

used to design resonant-wall radomes to operate at frequencies other than those used in testing the samples. The  $D/\lambda$ , ratio would be chosen on the basis of the bandwidth required, and the possible combinations of metal plate and surface dielectric thicknesses found from Fig. 11. If the same cavity layout, dielectric constant, and  $(s - D)/s$  ratio are used, the radome will be resonant at the desired frequency for perpendicularly polarized waves incident at the angle given on Fig. 11. It would also be possible to use the information contained in Fig. 11 to obtain approximate designs for resonant-wall radomes using a different dielectric and having the cavities in a hexagonal array, as will be explained on pp. 21 to 24.

Although the contour curves shown in Fig. 11 are nearly straight lines, which probably cover the region of practical interest, caution must be used in extrapolating the curves. It is known, for instance, that as the surface dielectric becomes thin and the local fields at the ends of the cavities cross the dielectric-to-air interface, the curves change slope rapidly to connect with the points along the abscissa. There may be a similar effect as the metal plate becomes thin and the local fields at the two ends of each cavity interact. These effects were not investigated in detail since neither  $l_2/\lambda_2$  or  $l_3/\lambda_3$  is likely to be small in an actual resonant-wall radome.

Note that for each value of cavity diameter, there is a value of dielectric thickness such that the resonance frequency of the radome is the same whether the dielectric layer is present or absent. This special value for the thickness of the dielectric layer can be found by drawing a line parallel to the ordinate, passing through the point along the abscissa for the particular value of cavity diameter. The intersection of this line with the respective  $D/\lambda_3$  contour gives the special value of  $l_2/\lambda_2$ . When this is done for various values of cavity diameter, it is found that  $l_2/\lambda_2$  ranges from 0.41 to 0.44. If adding a layer of dielectric of this thickness to one surface of the metal plate does not change the resonance frequency, then adding a second dielectric layer of this thickness to the other surface of the metal plate would not change the resonance frequency either. Thus, Fig. 11 supplies a limited amount of data for designing resonant-wall radomes with dielectric layers in contact with each surface of the metal plate, as shown in Fig. 1(c). Comparing Figs. 9 and 11, it is seen that adding one dielectric layer to the metal plate does not greatly change the 3-db bandwidth. Thus, it is not expected that adding the second dielectric would change the 3-db bandwidth significantly. It should be kept in mind that these data apply for perpendicularly polarized waves.

incident at a fixed angle, thus they do not provide sufficient information on which to base a comparison between the usable bandwidths of the various radome configurations considering a wide range of incidence angles and polarizations.

In addition to providing design data, Fig. 11 shows some of the general properties of resonant-wall radomes with dielectric on one surface. One conclusion that can be drawn is that in order to obtain the widest possible bandwidth the radome should be designed to operate as far from cutoff of the cavities as possible, i.e., with  $D/\lambda_3$  as large as possible. Another conclusion is that for a given  $D/\lambda_3$  ratio less than about 0.68, the bandwidth increases slightly as the thickness of the metal plate is decreased, but for larger  $D/\lambda_3$ , the bandwidth is independent of the thickness of the metal plate. A third conclusion is that the tolerance on the thickness of the metal plate would be less stringent than that on the thickness of the surface dielectric. This can be seen from Fig. 11 since the resonance frequency changes less with a given change in metal plate thickness than for the same change in the dielectric thickness.

#### GENERALIZATION OF THE DESIGN DATA

In obtaining the data presented in Figs. 8 through 11, only a limited number of the sample parameters were varied. Techniques for applying this design data to other resonant-wall radomes will now be considered briefly. Although the data were obtained with samples operating within the frequency range from 3.4 to 6.4 kMc, these data can be used to design resonant-wall radomes to operate at any frequency by normalizing the radome dimensions with respect to wavelength, as was done for Figs. 8 through 11. For greatest accuracy in applying these data, the dielectric constant, ratio of  $(s - D)/s$ , layout of the cavities, polarization, and incidence angle should be as specified on the figures. If these parameters are changed, the discontinuities at the ends of the cavities will change, and the actual resonance frequency will be only approximately equal to the desired value.\*

Next consider generalization of the bandwidth data. In discussing the bandwidth of resonant radomes it is convenient to use the concept of  $Q$  discussed in Ref. 1 (on pp. 113 to 117). For the convenience of the reader, the various  $Q$ 's of a resonant-wall radome will be reviewed briefly.

---

\* Techniques for determining the effect of changing the discontinuities at the cavity ends will be considered on pp. 38 to 43 and 52 to 54.

By definition, the  $Q$  of a resonant device is proportional to the ratio of the average stored energy divided by the energy lost per cycle. The un-loaded  $Q$ ,  $Q_0$ , of the radome is determined by dissipation loss in the metal surfaces and in the dielectric by the relation

$$\frac{1}{Q_0} = \frac{1}{Q_c} + \frac{1}{Q_d} \quad (8)$$

Here  $Q_c$  is the  $Q$  due to dissipation loss in the metal surfaces, and can be determined from Fig. VI-3 of Ref. 1, or from Montgomery.<sup>3</sup> The  $Q$  due to dissipation loss in the dielectric is

$$Q_d = \frac{1}{\tan \delta} \quad (9)$$

where  $\tan \delta$  is the loss tangent of the dielectric. For most combinations of metal and dielectric,  $Q_0$  is approximately equal to  $Q_d$ . The external  $Q$ ,  $Q_E$ , is that due to the energy coupled out of the ends of the cavities into space, and the loaded  $Q$ ,  $Q_L$ , is that due to all sources of energy loss, and is related to  $Q_E$  and  $Q_0$  by Eq. (10):

$$\frac{1}{Q_L} = \frac{1}{Q_0} + \frac{1}{Q_E} \quad (10)$$

The loaded  $Q$  of a radome sample can be readily determined by measuring the insertion loss of the sample as a function of frequency. The  $Q_L$  is then found using Eq. (11):

$$Q_L = \frac{f_r}{f_u - f_l} \quad (11)$$

where  $f_r$  is the resonance frequency as indicated by minimum insertion loss, and  $f_u$  and  $f_l$  are the upper and lower frequencies, respectively, at which the insertion loss is 3 db greater than at  $f_r$ . The 3-db bandwidth of the radome is, by the usual definition, equal to  $100/Q_L$  percent. Assuming that the loss tangent of the dielectric and the conductivity of the metal used in the sample are known, the  $Q_E$  of the sample can be calculated using Eqs. (8), (9), and (10).

Equations were derived in Ref. 1 for the external  $Q$  of resonant-wall radomes with constricted coupling apertures at the ends of the cavities. Although these equations do not give the correct numerical value for the  $Q_g$  of the radomes being considered here, they do suggest that for  $D/\lambda_3$  and  $l_3/\lambda_3$  held constant,

$$Q_g = AF \sqrt{\epsilon_3} \left(\frac{s}{D}\right)^2 \sec \theta \quad (12)$$

when perpendicularly polarized waves are incident on the radome, and

$$Q_g = AF \sqrt{\epsilon_3} \left(\frac{s}{D}\right)^2 \cos \theta \quad (13)$$

when parallel-polarized waves are incident on the radome, where  $\theta$  and  $A$  are as defined under Eq. (3), and  $F$  is a constant of proportionality.

Thus, once  $Q_g$  has been measured for one resonant-wall radome sample, the factor  $F$  can be evaluated and the 3-db bandwidth can be approximately determined for resonant-wall radomes with the same  $D/\lambda_3$  and  $l_3/\lambda_3$  ratios, but with different dielectric constant, loss tangent, conductivity, and cavity spacing, and operating at different incidence angles with waves of either polarization. If the  $Q_0$  of the radome is not changed, it is convenient to make one further approximation and substitute  $Q_L$  for  $Q_g$  in Eqs. (12) and (13). This approximation will be justified in the following paragraphs.

Finally, consider generalization of the transmission data. The power transmission coefficient of a resonant-wall radome at its resonance frequency can be calculated from the  $Q$ 's defined above using the well-known relations given in Eq. (14):

$$T^2 = \left(\frac{Q_L}{Q_g}\right)^2 \quad (a)$$

$$= \left(1 - \frac{Q_L}{Q_0}\right)^2 \quad (b) \quad (14)$$

$$= \left(1 + \frac{Q_g}{Q_0}\right)^{-2} \quad (c)$$

Thus, by the use of Eqs. (8) through (14) the transmission at resonance can be determined for resonant-wall radomes other than those used to obtain the design data of Figs. 8 through 11.

For radomes of practical interest,  $T^2$  is not much less than unity; thus Eq. (14a) shows that  $Q_L$  can be substituted for  $Q_0$  for some approximate calculations. If the loss tangent of the dielectric and the conductivity of the metal in the radome are not known, Eq. (14b) can be used to determine  $Q_0$  from the measured insertion loss at the resonance frequency. It should be pointed out, however, that small errors in the measured  $T^2$  at resonance can introduce large errors in the calculated value of  $Q_0$  if the insertion loss at resonance is small.

#### MEASURED PERFORMANCE AS A FUNCTION OF INCIDENCE ANGLE

Radome samples mounted in waveguide can be used to determine the dimensions required for the radome to be resonant at a given frequency, as was described on pp. 11 to 20. It is not convenient, however, to measure the electrical performance of radomes as a function of incidence angle and polarization using samples mounted in waveguide. The incidence angle and the polarization of the incident wave can be readily changed using flat radome panels in free space, but this method has the disadvantage that relatively large radome samples are required. As a compromise between the flexibility of free-space measurements and the small samples required for waveguide measurements, a measurement set-up using a parallel-plate transmission line has been developed. A flat-strip radome sample, such as that shown in Fig. 12, is mirrored in the conducting surfaces of

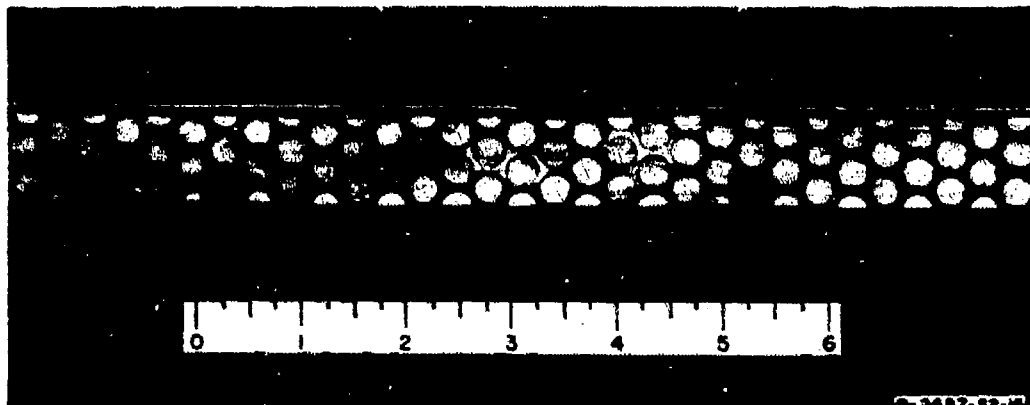


FIG. 12  
RESONANT-WALL RADOME SAMPLE FOR TEST IN A PARALLEL-PLATE TRANSMISSION LINE

the transmission line to simulate a flat-panel radome sample. Details of the measurement technique are described in Appendix A.

The physical dimensions of a resonant-wall radome sample tested in the parallel-plate transmission-line set-up are given in Table 2. The radome sample operated at the first resonance will be referred to as Radome A, and the sample operated at the second resonance will be referred to as Radome B. As presented here, Radomes A and B have the same physical dimensions, but are operated at different frequencies. They are referred to as separate radomes since they would not have the same physical dimensions if scaled to operate at the same frequency. The dimensions of Radomes A and B are given in Table 3 in terms of wavelength.

The measured power transmission coefficient and insertion phase delay of Radome A are shown in Fig. 13 for several frequencies. Of the curves shown, high transmission was obtained for waves polarized perpendicular to the plane of incidence over the widest range of incidence angles at a frequency of 8415 Mc. When the transmission of waves polarized parallel to the plane of incidence is also considered, the best operating frequency is 8450 Mc.\* At this frequency, at least 80 percent of the incident power is transmitted for incidence angles up to 70 degrees. As the incidence angle varies from 0 to 70 degrees, the insertion phase delay varies 56 degrees for perpendicularly polarized waves, and 68 degrees for parallel polarized waves. As is well known, the variation in insertion phase delay depends on the physical thickness of the radome as well as on the type of radome. Thus, for the purpose of this study, the insertion phase delay characteristics of the resonant-wall radomes will not be compared directly with those of conventional uniform-dielectric radomes since the two types of radomes would, in general, have different physical thicknesses. A more general comparison is obtained by comparing the variation in insertion phase delay of the radome with the variation in electrical thickness of an air path of the same physical thickness as the radome.<sup>†</sup> For Radome A,

\* For parallel polarized waves, the parallel-plate transmission-line set-up does not provide data on the electrical performance at small incidence angles, as explained in Appendix A. Also, the accuracy of the points shows at the smallest incidence angles for parallel-polarized waves is relatively poor. These are not serious limitations in testing the resonant wall radomes being considered here, since the electrical performance is expected to vary smoothly at small incidence angles, as indicated by the dashed curves extrapolated back to zero incidence angle.

<sup>†</sup> The insertion phase delay,  $\psi$ , of a radome is defined as the difference between the phase delay,  $\psi'$ , of a wave passing through the radome and  $(2\pi L/\lambda) \cos \theta$ , the electrical thickness of an air path of the same physical thickness,  $L$ , as the radome. If the resonance frequency of a radome does not change greatly with incidence angle,  $\theta$ , the phase delay  $\psi'$  will not change greatly with incidence angle. Thus it is to be expected that the variation in  $\psi$  with incidence angle will be of the same order of magnitude as the variation in  $(2\pi L/\lambda) \cos \theta$ .

**TABLE 2**  
**DIMENSIONS OF RESONANT-WALL RADOME SAMPLES A AND B**  
**IN PHYSICAL UNITS**

Arrangement of cavities	Hexagonal Array
Diameter of cavities, $D$	0.3125 inch
Center-to-center spacing of cavities, $s$	0.360 inch
Ratio of wall thickness between cavities to spacing of cavities, $(s - D)/s$	0.132
Thickness of metal plate, $l_3$	0.250 inch
Dielectric in cavities:	
Material	Alumina ceramic*
Relative dielectric constant, $\epsilon_3$	8.66†
Loss tangent, $\tan \delta_3$	0.0018†
Height of sample	0.900 inch
Length of sample	24 inches

\* Material supplied by Raytheon Manufacturing Company, Waltham, Massachusetts.

† Measured values.

**TABLE 3**  
**DIMENSIONS OF RESONANT-WALL RADOME SAMPLES A AND B**  
**IN TERMS OF WAVELENGTH**

	RADOME A	RADOME B
Order of resonance	First	Second
Resonance frequency at wide incidence angles (perpendicular polarization)	8.43 kMc	12.2 kMc
Free-space wavelength at resonance, $\lambda$	1.401 inches	0.968 inch
Wavelength in the dielectric at resonance, $\lambda_3$	0.476 inch	0.329 inch
Guide wavelength at resonance, $\lambda_{g3}$	1.058 inch	0.418 inch
Diameter of cavities, $D$	$0.65\epsilon \lambda_3$	$0.950 \lambda_3$
Thickness of metal plate, $l_3$	$0.525 \lambda_3$	$0.760 \lambda_3$
Electrical length of cavities, $l_3/\lambda_{g3}$	0.236	0.598
Center-to-center spacing of cavities, $s$	$0.257 \lambda$	$0.372 \lambda$
Thickness of radome, $L = l_3$	$0.178 \lambda$	$0.258 \lambda$

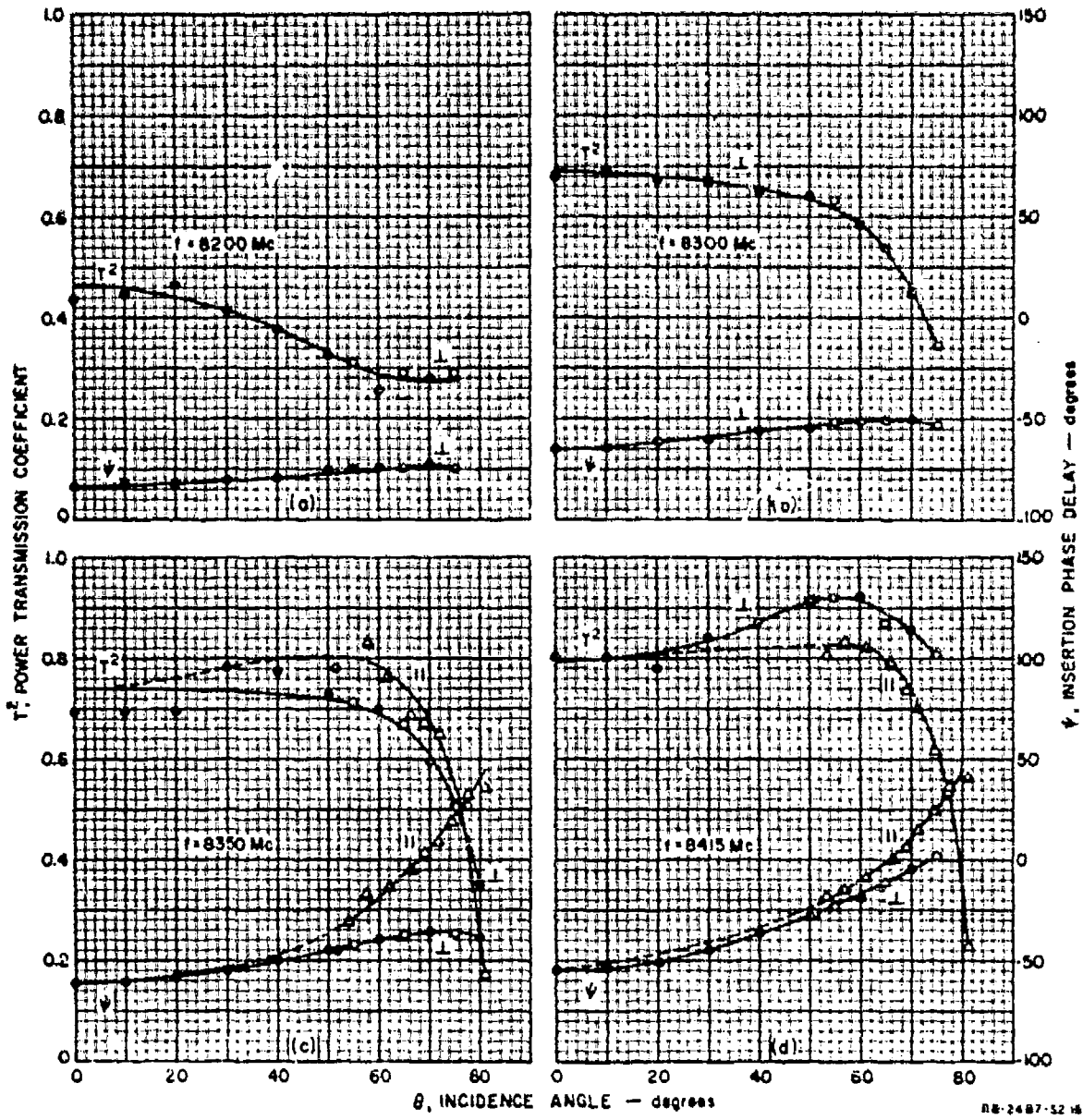


FIG. 13  
MEASURED TRANSMISSION AND PHASE DELAY OF RESONANT-WALL RADOME SAMPLE A

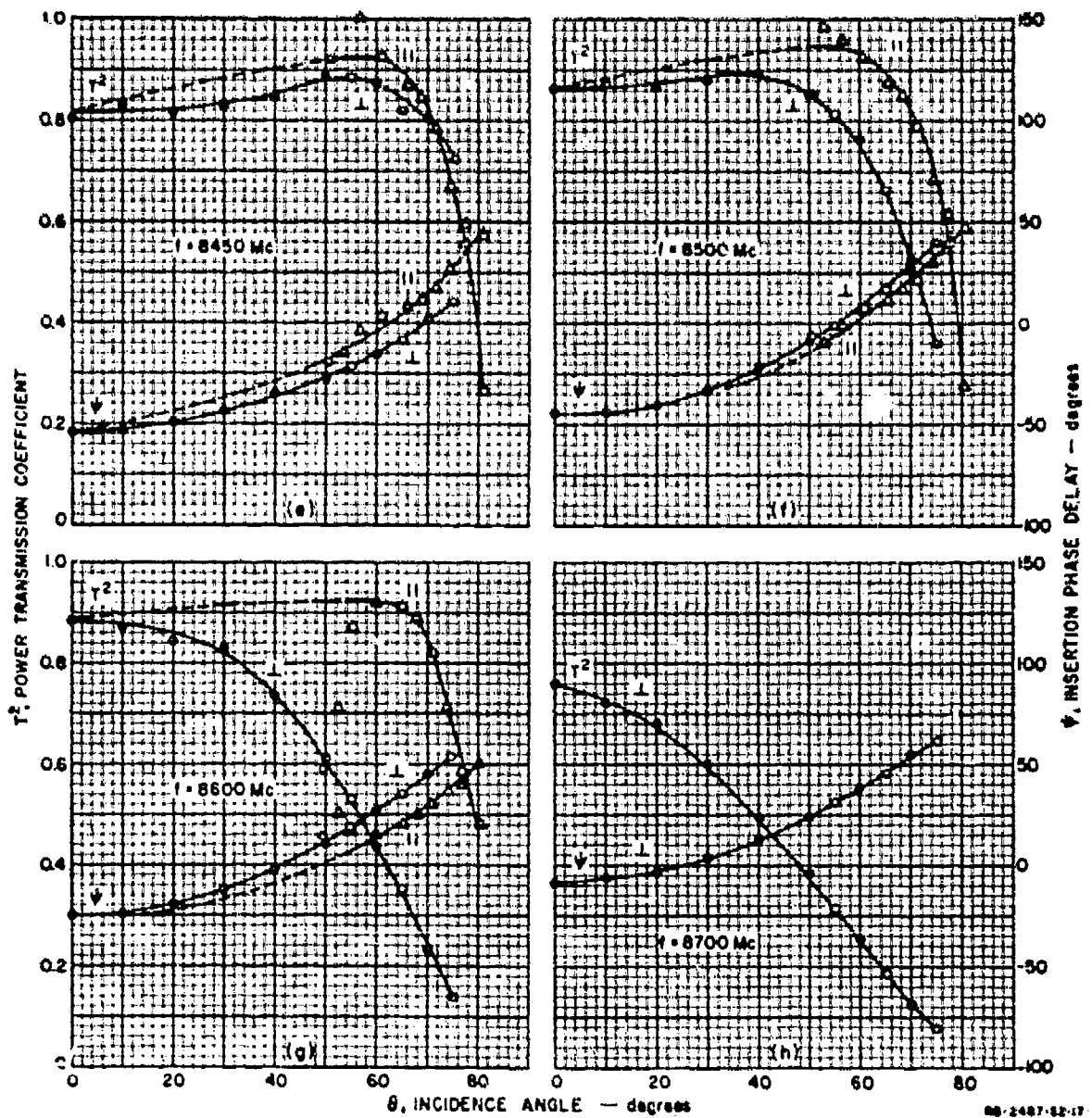


FIG. 13 (Continued)

MEASURED TRANSMISSION AND PHASE DELAY OF RESONANT-WALL RADOME SAMPLE A

the variation in insertion phase delay is greater than the variation in the electrical length of this air path by 14 degrees for perpendicularly polarized waves, and 26 degrees for parallel-polarized waves.

The performance of the radome as a function of frequency can be more readily visualized by means of Fig. 14. Figure 14(a) shows that the resonance frequency and bandwidth of the radome are functions of the incidence angle for perpendicularly polarized waves. The frequency response for small incidence angles is sufficiently broad that when the radome is operated at the resonance frequency for perpendicularly polarized waves incident at wide angles, high transmission is obtained over a wide range of incidence angles. Figure 14(b) shows that, for parallel-polarized waves, the insertion loss increases rapidly for incidence angles greater than 70 degrees over the frequency range of interest. Thus, the maximum incidence angle for which Radome A can be used is determined by the transmission coefficient for parallel-polarized waves.

Figure 14 can also be used to determine the bandwidth of the radome for given minimum transmission coefficient and range of incidence angles. The 3-db bandwidth\* and the transmission coefficient at resonance for perpendicularly polarized waves are plotted in Fig. 15 as functions of the incidence angle. The agreement between the measured points and the upper two curves in Fig. 15 supports the approximate generalization techniques suggested on pp. 21 to 24. The cosine curve was drawn through the measured bandwidth at  $\theta = 0$ , and agrees well with bandwidth at other incidence angles. The top curve was calculated using the  $Q_L$  found from the solid curve, and using a value of 500 for  $Q_0$ . This  $Q_0$  was measured with a single cavity mounted in rectangular waveguide in the process of measuring the dielectric constant and loss tangent of the alumina ceramic filling the cavities. The  $Q_0$  of the radome should not be significantly different from this value.

It is of interest to compare the bandwidth of this resonant-wall radome with that of a more familiar uniform dielectric radome, even though the radomes do not have exactly the same physical thickness. The 3-db bandwidth of Radome A for perpendicularly polarized waves incident at wide angles is smaller by a factor of 0.17 than that of a half-wavelength radome with a dielectric constant of  $\epsilon = 8.66$ . Although this factor does not

\* The bandwidth between the frequencies at which the insertion loss is 3 db higher than at resonance is considered here since this quantity is the best general measure of bandwidth. As explained on pp. 21 to 24, the 3-db bandwidth measured for one resonant-wall radome can be approximately applied to other resonant-wall radomes.

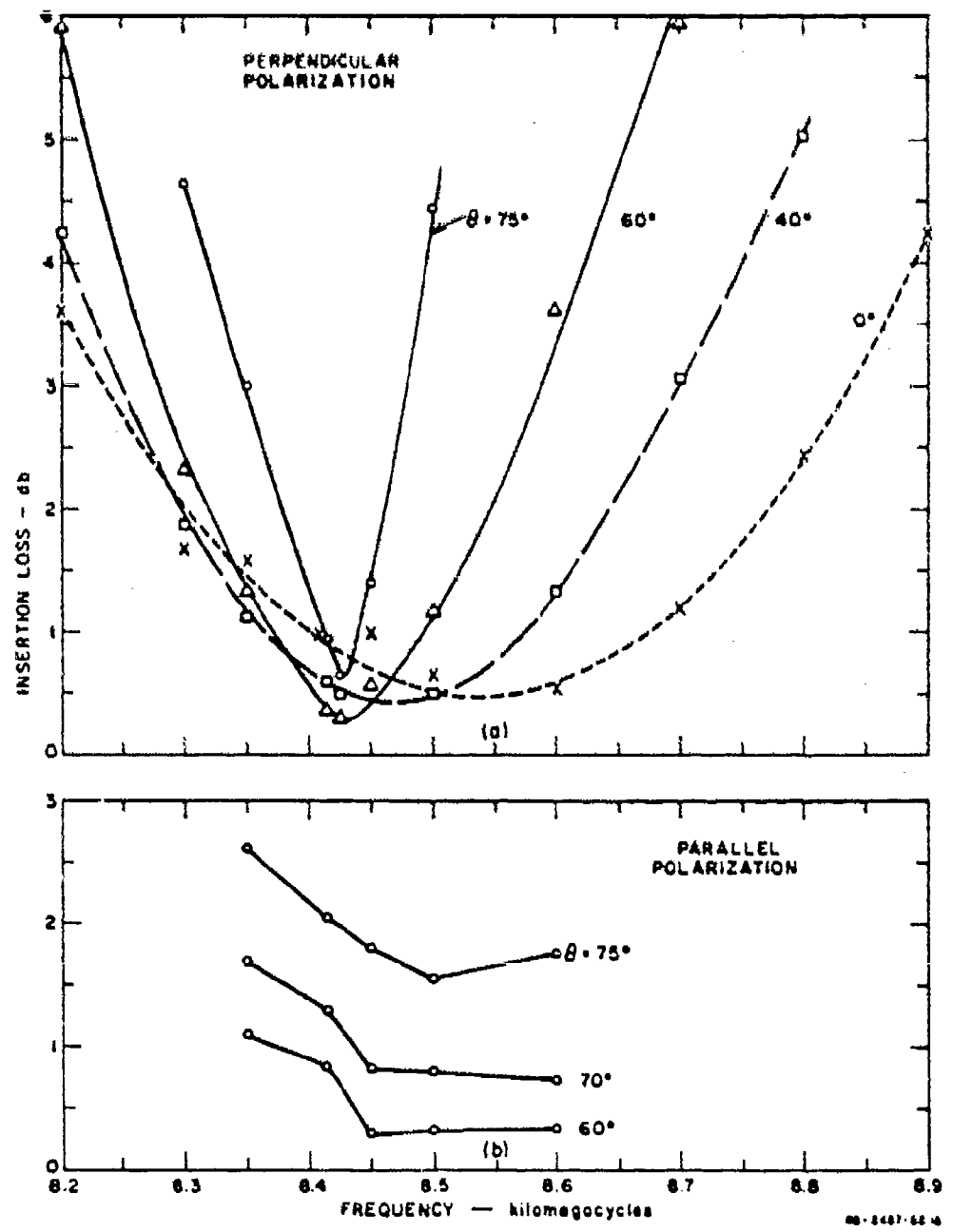


FIG. 14

WADD TR 60-84

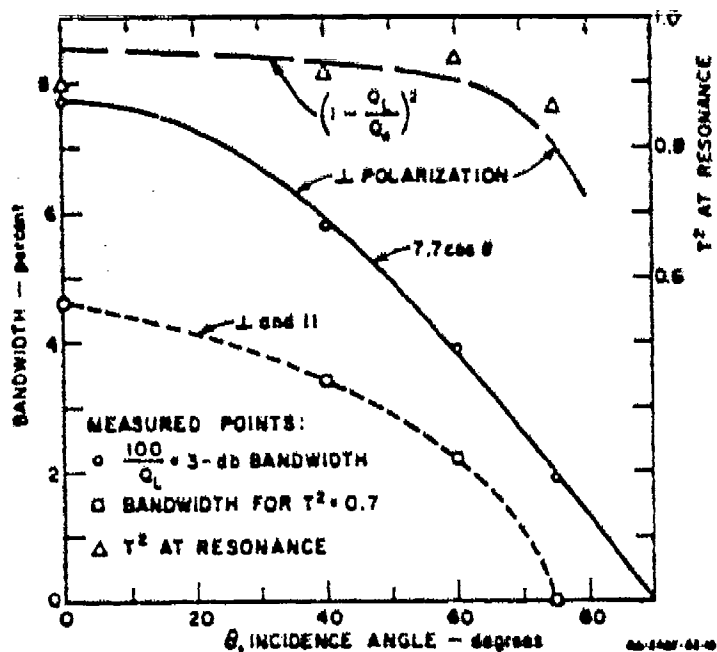


FIG. 15  
MEASURED BANDWIDTH AND TRANSMISSION OF  
RESONANT-WALL RADOME SAMPLE A

apply to all resonant-wall radomes, it does emphasize the fact that resonant-wall radomes are narrow-band structures.

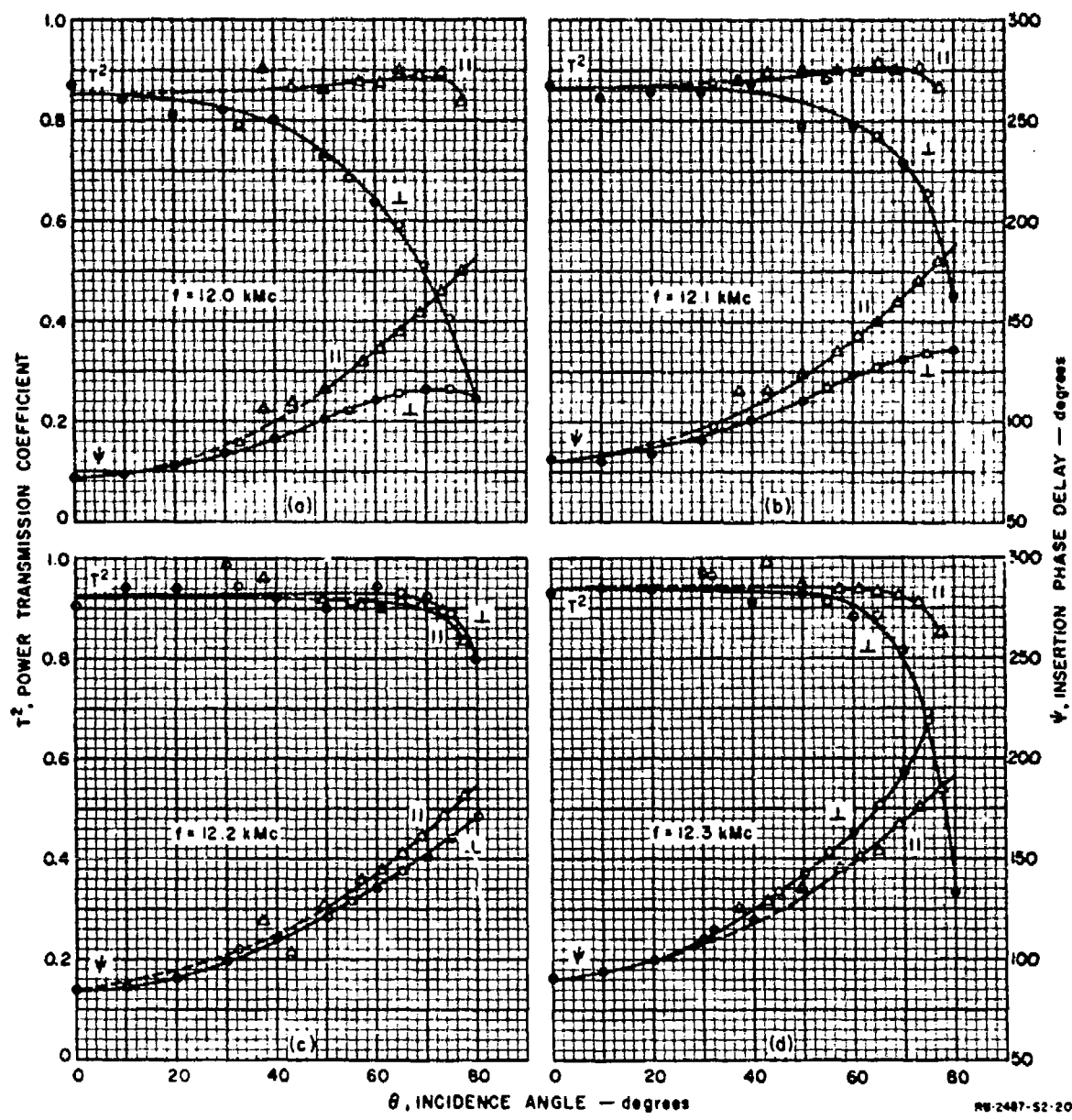
Also of interest is the bandwidth of the radome within which the transmission coefficient does not fall below a given minimum value. This minimum acceptable value will, of course, depend on the application for which the radome is intended. As a representative value, the bandwidth for a minimum power transmission of 70 percent for both perpendicularly and parallel polarized waves is shown by the lower curve in Fig. 15.

The resonance frequency and 3-db bandwidth predicted by Figs. 8 and 9 for perpendicularly polarized waves incident at  $\theta = 57$  are as follows. The predicted resonance frequency is 8.48 kMc, which is only 0.6 percent higher than the observed resonance of 8.43 kMc. This is good agreement considering that the approximate techniques of pp. 21 to 24 were used, but better accuracy would be desirable if the radome were to be used at incidence angles greater than 60 degrees. The predicted 3-db bandwidth is 4.0 percent, which is nearly equal to the observed value of 4.2 percent.

The measured power transmission coefficient and insertion phase delay of Radome B are shown in Fig. 16 for several frequencies. High transmission is obtained over the widest range of incidence angles at 12.2 kMc. At this frequency, at least 90 percent of the power is transmitted for incidence angles up to 70 degrees for either perpendicularly or parallel polarized waves incident on the radome. At least 80 percent of the power is transmitted for incidence angles up to about 80 degrees. As the incidence angle varies from 0 to 80 degrees, the insertion phase delay varies 86 degrees for perpendicularly polarized waves, and 102 degrees for parallel-polarized waves. These variations are 9 degrees and 25 degrees greater, respectively, than the variation in the electrical thickness of a layer of air of the same physical thickness as the radome.

The transmission of the radome at wide incidence angles is shown as a function of frequency in Fig. 17. It is seen that the transmission of perpendicularly polarized waves drops off as the frequency departs from 12.2 kMc, but the transmission of parallel-polarized waves is relatively independent of frequency. Figure 18 shows that for Radome B, as well as for Radome A, the 3-db bandwidth and the transmission at resonance vary with incidence angle as suggested by Eqs. (12), (13), and (14). Figures 8 and 9, together with the approximate techniques of pp. 21 to 24, predict the resonance frequency to be 12.37 kMc, and the 3-db bandwidth to be 9.8 percent for perpendicularly polarized waves incident at an angle of 35 degrees. Although data were not taken over a sufficiently wide frequency range to accurately determine the resonance frequency and bandwidth at such a small incidence angle, the predicted values seem to fit in very well with the values observed at wide incidence angles. The 3-db bandwidth of Radome B for perpendicularly polarized waves incident at wide angles is smaller by a factor of 0.47 than that of a full-wavelength radome with a dielectric constant of  $\epsilon = 8.66$ .

Comparing the electrical performances of Radomes A and B, it is seen that at their center frequencies Radome B gives high transmission for waves of either polarization over a wider range of incidence angles than does Radome A. Also, Radome B has a larger bandwidth than Radome A when operation out to a given incidence angle is considered. The 3-db bandwidth of Radome B is larger than that of Radome A by a factor of 1.43. The bandwidth of Radome B for  $T^2 = 0.7$  is twice that of Radome A at  $\theta = 70^\circ$ , and this difference increases for larger incidence angles.



The insertion phase delay of Radome B varies with incidence angle more than that of Radome A, since Radome B is the thicker of the two as measured in free-space wavelengths at the respective operating frequencies. It should be pointed out however, that Radome B is probably thinner than some of the other radome configurations suggested in Fig. 1, and thus could be expected to have less variation in insertion phase delay than some configurations. For both Radomes A and B, the insertion phase delay varies with incidence angle a few degrees more than does the electrical thickness of an air path the same thickness as the radomes. For uniform-dielectric half-wavelength and full-wavelength radomes, the insertion phase delay varies less than the electrical thickness of an air path the same thickness as the radome.\* Thus it appears that resonant-wall radomes of the type illustrated in Fig. 1(a) would have slightly higher boresight error than uniform-dielectric radomes of the same physical thickness.

The diameter of the cavities in Radome B, measured in terms of wavelength in the dielectric, is sufficiently large that the  $\text{TM}_{01}$  mode can propagate in the cavities, as well as the dominant  $\text{TE}_{11}$  mode. The  $\text{TM}_{01}$  mode will not couple to perpendicularly polarized waves incident on the radome, but it will couple to parallel-polarized waves. If a resonance of the  $\text{TM}_{01}$  mode occurs near the operating frequency of the radome, this mode might degrade the transmission or phase characteristics of the radome. While testing the sample of Radome B with waves containing both perpendicularly and parallel polarized components, a sharp dip in the

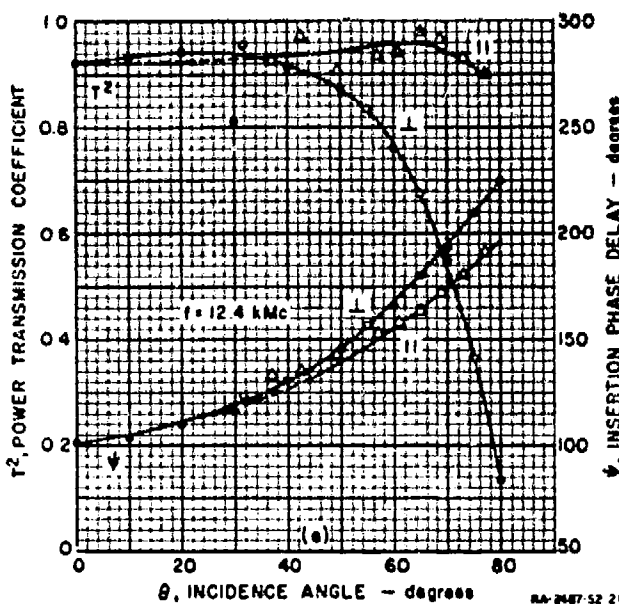


FIG. 16 (Continued)

MEASURED TRANSMISSION AND PHASE DELAY OF  
RESONANT-WALL RADOME SAMPLE B

\* For example, for a half-wavelength radome with  $\epsilon = 9.3$ , designed for maximum transmission at  $\theta = 85$  degrees, the variation in insertion phase delay for perpendicularly polarized waves as the incidence angle varies from 0 to 70 degrees is 12 degrees less than the variation in the electrical thickness of the air path. The corresponding figure for a full-wavelength radome with the same parameters is 22 degrees.

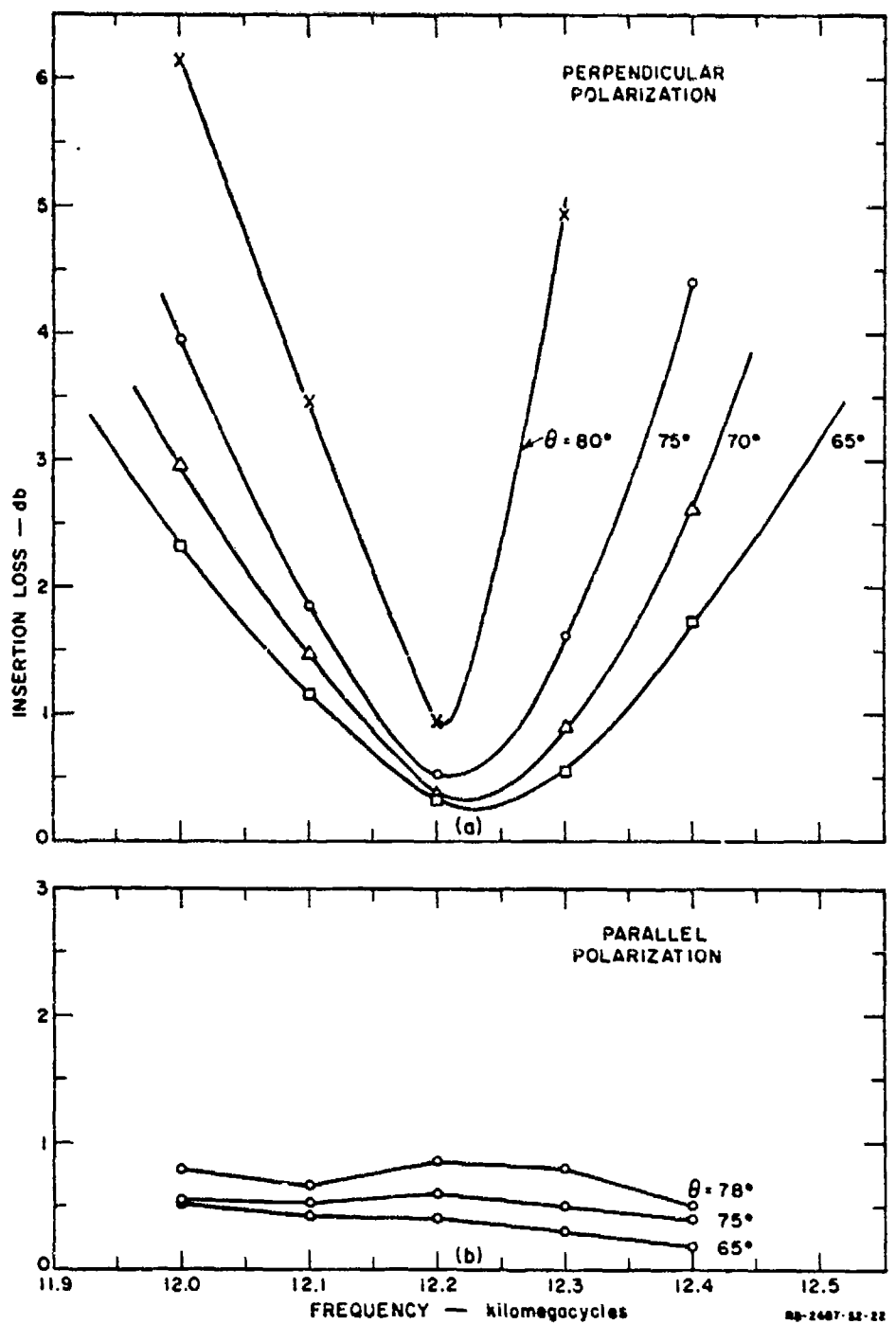


FIG. 17  
MEASURED INSERTION LOSS OF RESONANT-WALL RADOME SAMPLE B

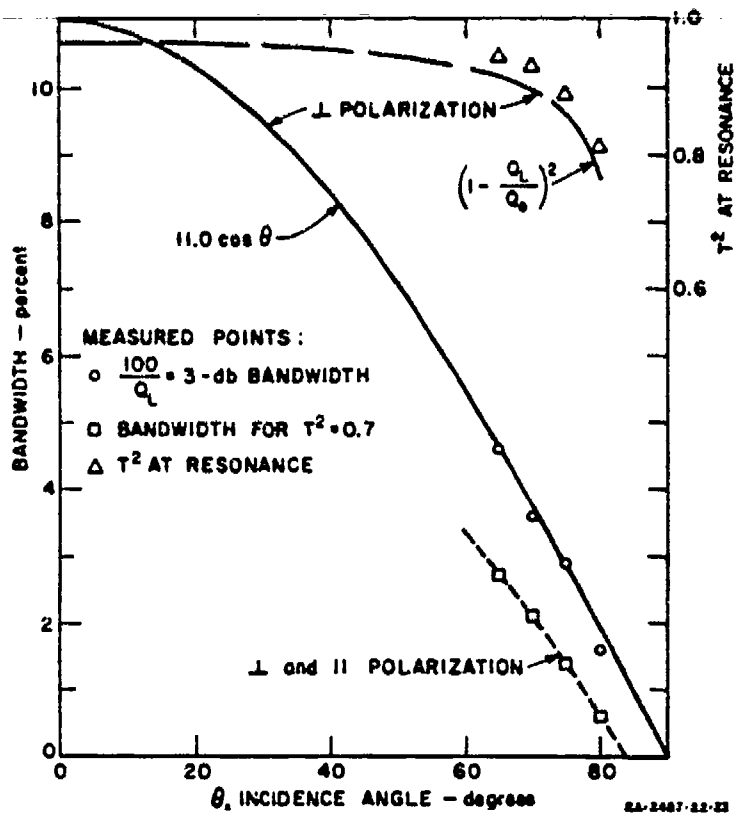


FIG. 18  
MEASURED BANDWIDTH AND TRANSMISSION OF  
RESONANT-WALL RADOME SAMPLE B

transmission vs. frequency curve was observed extending from about 12.5 to 12.7 kMc, with the power transmission dropping to about 43 percent at the lowest point. It is assumed that this dip is due to a resonance of the  $TM_{01}$  mode. For this particular radome, the  $TM_{01}$  mode did not interfere with the electrical characteristics within the frequency band where the radome is usable at wide incidence angles; thus detailed data on the shape of the dip were not taken. This demonstrates that Eqs. (2) and (4) do not necessarily have to be satisfied, provided care is taken to keep resonances of the  $TM_{01}$  mode away from the operating frequency of the radome. No data other than the preceding are presently available, however, for predicting the resonance frequency for the  $TM_{01}$  mode.

#### EQUIVALENT CIRCUITS OF RESONANT-WALL RADOMES

##### GENERAL

The transmission or reflection coefficients for a ray striking a particular point on a curved radome can be calculated assuming these

coefficients to be the same as those for an infinite plane panel of the same radome material with a plane wave incident at the same angle and with the same polarization as the ray in question. This assumption is justified for the usual case where the radii of curvature of the radome are large relative to the wavelength of the incident energy. The electrical performance for the plane-panel, plane-wave case can, in turn, be calculated using microwave filter theory, provided that an equivalent circuit is known for the radome panel. This approach was used extensively on the previous contract<sup>1</sup> to calculate the power transmission and insertion phase delay of radome panels containing metal structures whose equivalent circuits are known.

The resonant-wall radome, however, has not been analyzed theoretically to determine its exact equivalent circuit. Therefore, an experimental program was conducted to obtain design data for resonant-wall radomes. In addition, the power transmission and insertion phase delay were measured as functions of incidence angle and polarization of the incident wave for some specific radome designs. The information obtained from this program also made it possible to deduce equivalent circuits that describe the behavior of the radomes to a fair degree of approximation.

#### RESONANT-WALL RADOMES WITHOUT SURFACE DIELECTRIC

The physical similarities between the basic resonant-wall radome (i.e., one without surface dielectric) and other structures for which the equivalent circuits are known, suggested that the equivalent circuit of Fig. 19 might be used to describe the radome in question. This equivalent circuit can be valid only if the center-to-center spacing of the cavities is sufficiently small that none of the energy is transferred from the

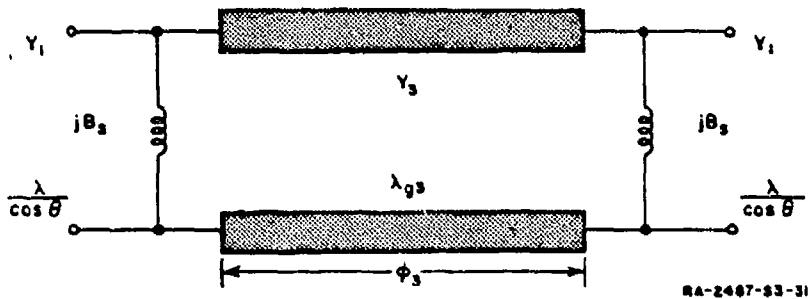


FIG. 19  
EQUIVALENT CIRCUIT OF RESONANT-WALL RADOMES WITHOUT SURFACE DIELECTRIC

incident wave to diffracted waves, i.e., Eq. (3) must be satisfied. It is assumed that in practice this equation would be satisfied to avoid deterioration of the antenna pattern used with the radome. It is also assumed, as a simplification, that the cavities are sufficiently close together that the surface of the radome appears isotropic to the incident wave. A well-defined criterion for isotropy in a structure of this kind does not exist.

Energy propagates through the metal plate by means of the many circular-waveguide transmission lines; thus, the metal plate can be represented as a transmission line of appropriate characteristic admittance,  $Y_3$ , electrical length,  $\phi_3$ , and attenuation constant,  $a_3$ . In the region of each air-to-radome interface, there are nonpropagating modes required to satisfy the boundary conditions at the surfaces of the radomes. Since energy is stored in these modes, their presence can be accounted for by the shunt susceptances in Fig. 19. Approximate values for the circuit parameters were deduced as follows.

It is seen intuitively that the nonpropagating fields in free space near one surface of the resonant-wall radome would be very similar to those on each side of a zero-thickness perforated metal sheet with the same aperture diameter and spacing as the radome. Thus, the expression for the susceptance,  $B_s$ , at each surface of the radome should contain one term equal to half the shunt susceptance of a zero-thickness perforated metal sheet. There will also be nonpropagating modes present inside the circular-waveguide cavities, which will contribute a second term to the expression for  $B_s$ . It will be shown later that it is also convenient to take these latter nonpropagating modes into account by shifting the reference planes, at which the equivalent circuit is taken as valid, out of the planes of the radome panel surfaces. Formulas are not available for calculating the equivalent shunt susceptance or the reference-plane shift due to the nonpropagating modes in the circular waveguides, and for initial calculations they were neglected completely. That is, the shunt susceptance at each surface of the metal plate was taken to be half that of a zero-thickness perforated metal sheet, as given by Eq. (15):

$$B_s = -\frac{A}{377} \cdot \frac{3}{2\pi} \cdot \left(\frac{s}{D}\right)^2 \left(\frac{\lambda}{D}\right) \left[1 - \left(\frac{1.706 D}{\lambda}\right)^2\right] \quad (15)$$

where, as before

$$A = \begin{cases} 1 & \text{for a square array of cavities} \\ 0.5 : 3 & \text{for a hexagonal array of cavities} \end{cases}$$

s = center-to-center spacing of the cavities  
D = diameter of the cavities  
 $\lambda$  = free-space wavelength.

Equation (15) was used for the case where the incident waves are polarized parallel to the plane of incidence as well as for the case where the incident waves are polarized perpendicular to the plane of incidence.

Equation (III-10) of Ref. 1, which gives the theoretical shunt susceptance of a thin perforated metal sheet with parallel-polarized waves incident on it, contains a term involving the squared sine of the angle of incidence. This term accounts for coupling through the apertures of a thin sheet by the equivalent of the  $TM_{01}$  circular-waveguide mode. For the present application, this term is not required since the resonant-wall radome is sufficiently thick that coupling through it by the  $TM_{01}$  mode would have negligible effect on the end susceptances.\*

The characteristic admittance,  $Y_3$ , of the metal plate containing the dielectric-filled cavities is another circuit parameter that has not been evaluated theoretically. The parameter  $Y_3$  can be calculated for any resonant-wall radome whose resonance frequency has been measured, subject to the assumption that the end susceptance,  $B_e$ , is known. This calculation makes use of the fact that the midplane admittance of a symmetrical structure is purely real at resonance, and is conveniently carried out using simple graphical constructions on the Smith chart. The parameter  $Y_3$  was evaluated for a resonant-wall radome, whose dimensions were given under Radome A in Tables 2 and 3. It was noted that the value of  $Y_3$  resulting from these calculations was nearly equal to the value obtained by suitably modifying a formula given by Marcuvitz.<sup>4</sup> These modifications are described in Appendix B, and the resulting formula is given by Eq. (16):

---

\* It actually makes little difference in the calculated power transmission and insertion phase delay whether this sine-squared term is included or neglected. The measured electrical performance agrees slightly better with that calculated neglecting the sine-squared term.

$$Y_3 = \frac{AC_3}{377} \left( \frac{s}{D} \right)^2 \cdot \left[ \frac{1 - \left( 0.426 \frac{D}{s} \right)^2}{2J'_1 \left( \frac{\pi D}{4s} \right)} \right]^2 \cdot \frac{\lambda}{\lambda_{g3}} \text{ whos} \quad (16)$$

where

$C_3$  = a constant of proportionality

$J'_1$  = first derivative of the Bessel function of the first kind of first order

$\lambda_{g3}$  = guide wavelength in the cavities, as given by Eq. (7).

The value of  $C_3$  suggested by Marcuvitz's formula is 1.522. The factor involving the Bessel function is plotted in Fig. 20.

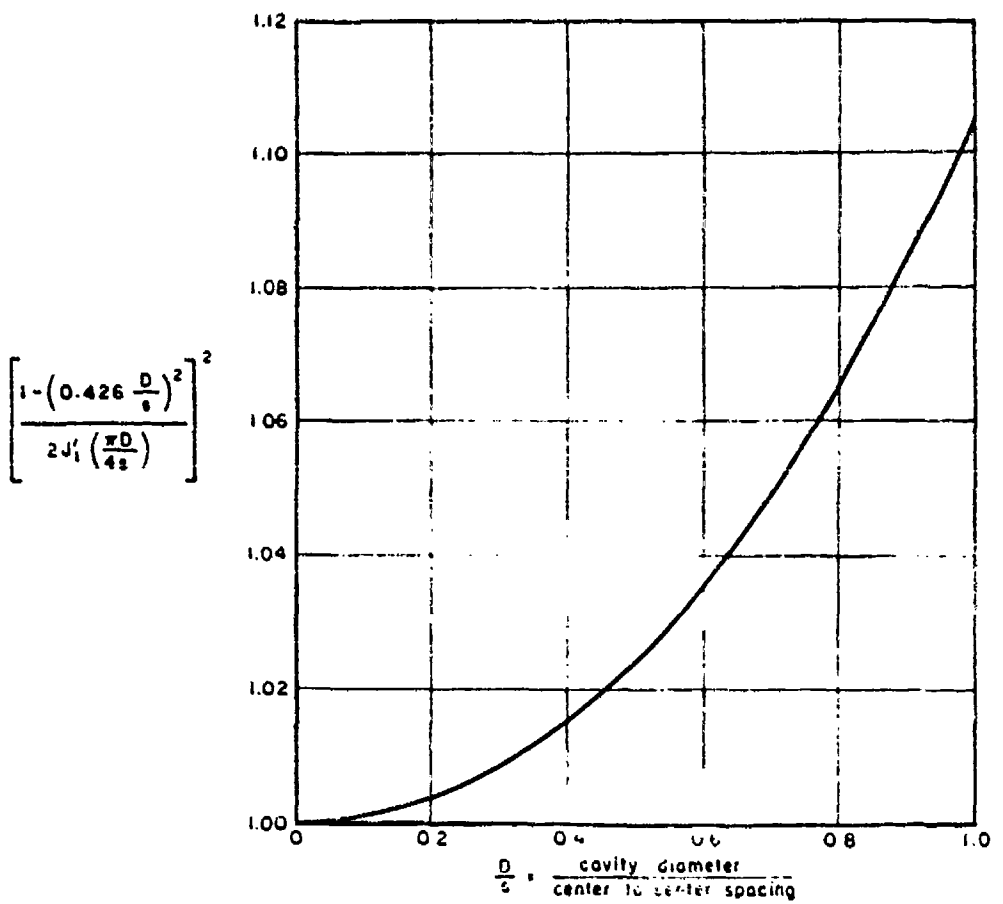


FIG. 20

A FACTOR USED IN CALCULATING THE CHARACTERISTIC ADMITTANCE  
OF RESONANT-WALL RADOMES

The product of the propagation constant within the cavities and the plate thickness is

$$\gamma_3 l_3 = a_3 l_3 + j\phi_3 \quad (17)$$

where

$$\phi_3 = \frac{2\pi l_3}{\lambda_{s3}} \text{ radians} \quad (18)$$

$\phi_3$  = electrical length of each cavity

$l_3$  = physical thickness of the metal plate.

The attenuation constant for the waves traveling through the cavities in the metal plate will be taken as equal to that for a wave in an infinitely long circular waveguide of diameter  $D$ , constructed with the same metal and dielectric as the radome. The actual attenuation constant will be only slightly different from the assumed value due to the nonpropagating modes at the cavity ends. Also, dissipation losses due to currents on the surfaces of the metal plate will be neglected since it is likely that they are small compared to those within the cavities. The attenuation constant is composed of two terms,

$$a_3 = a_d + a_c \quad (19)$$

where

$a_d$  = attenuation constant due to dissipation in the dielectric

$a_c$  = attenuation constant due to dissipation in the conducting walls of the cavity.

The attenuation constants  $a_d$  and  $a_c$  are given by Eqs. (20) and (21):<sup>5</sup>

$$a_d = \pi \frac{\lambda_{s3}}{\lambda_3} \cdot \frac{\tan \delta_3}{\lambda_3} \text{ nepers per inch for all dimensions in inches} \quad (20)$$

$$a_c = (1.5 \times 10^{-4}) \sqrt{\frac{\mu_r \rho}{P_c}} \sqrt{\frac{\epsilon_3}{\lambda}} \frac{\lambda_{s3}}{D \lambda_3} \left[ 0.420 + \left( \frac{\lambda_3}{1.706 D} \right)^2 \right] \quad (21)$$

where

- $\tan \delta_3$  = loss tangent of material filling the cavities  
 $\mu_r$  = relative permeability of the walls of the cavities  
 $\rho$  = resistivity of the walls of the cavities  
 $\rho_c = 1.724 \times 10^{-8}$  ohm-meter = resistivity of copper.

It is significant to note that for many combinations of dielectric and metal, most of the dissipation loss occurs in the dielectric. For example, the resonant-wall radome referred to as Radome B in this report is constructed of alumina ceramic with  $\tan \delta_3 = 0.0018$ , and of aluminum whose resistivity is approximately three times that of copper. For this radome,  $\alpha_d l_3 = 0.0055$ , and  $\alpha_c l_3 = 0.0006$ ; thus the dissipation loss in the metal is only 10 percent of the total. If the radome had been constructed of nonmagnetic stainless steel whose resistivity is 53 times that of copper, then  $\alpha_c l_3$  would have been 0.0026, and the dissipation loss in the metal would have been 32 percent of the total. The values of  $\alpha_c l_3$  quoted above, which were calculated assuming smooth metal surfaces, might be increased by a factor of up to about 1.6 by roughness of the metal surfaces.<sup>47</sup>

The power transmission coefficient and insertion phase delay of a resonant-wall radome without dielectric on its surface can be readily calculated from the equivalent circuit of Fig. 19. A convenient method for performing these calculations is the general-circuit-parameter method. The general circuit parameters,  $A$ ,  $B$ ,  $C$ , and  $D$ , are found from the matrix product of Eq. (22):

$$\begin{bmatrix} A & B \\ C & D \end{bmatrix} = \begin{bmatrix} 1 & 0 \\ jB & 1 \end{bmatrix} \begin{bmatrix} \cosh \gamma_3 l_3 & \frac{\sinh \gamma_3 l_3}{Y_3} \\ Y_3 \sinh \gamma_3 l_3 & \cosh \gamma_3 l_3 \end{bmatrix} \times \begin{bmatrix} 1 & 0 \\ jB & 1 \end{bmatrix} . \quad (22)$$

The power transmission coefficient,  $T^2$ , and the insertion delay,  $\psi$ , can then be calculated using Eqs. (23) and (24), respectively:

$$T^2 = \frac{4}{[A + BY_1 + C/Y_1 + D]^2} \quad (23)$$

$$\psi = \tan^{-1} \frac{\text{Im}(A + BY_1 + C/Y_1 + D)}{\text{Re}(A + BY_1 + C/Y_1 + D)} - \frac{360L}{\lambda} \cos \theta \text{ (degrees)} \quad (24)$$

where

$Y_1$  = characteristic admittance of free space

$L$  = total physical thickness of the radome

$\theta$  = incidence angle measured in free space between the incident ray and the normal to the radome surface.

The characteristic admittance of free space for waves polarized perpendicular to the plane of incidence is

$$Y_1 = \frac{\cos \theta}{377} \quad , \quad (25)$$

and for waves polarized parallel to the plane of incidence,

$$Y_1 = \frac{1}{377 \cos \theta} \quad . \quad (26)$$

The electrical performance calculated using the simplest assumptions regarding the values of the equivalent-circuit parameters will be considered first. Specifically, the nonpropagating modes within the cavities are neglected, hence Eq. (15) is used to calculate the reactive discontinuities at the surfaces of the radome. In calculating the characteristic admittance of the metal plate from Eq. (16), the value  $C_s = 1.522$  is used. This value is based on the constant given by Marcuvitz,<sup>4</sup> as explained in Appendix B. Subject to these assumptions, the curves of Figs. 21 and 22 were calculated. It is significant to note from these curves that for perpendicularly polarized waves the resonance frequencies change only slightly with changes in incidence angle. For parallel-polarized waves, however, the resonance frequencies shift rapidly with changes in incidence angle at wide angles. Also, the transmission between resonances for parallel-polarized waves increases with incidence angle up to approximately 80 degrees, and then decreases rapidly as the incidence angle is increased.

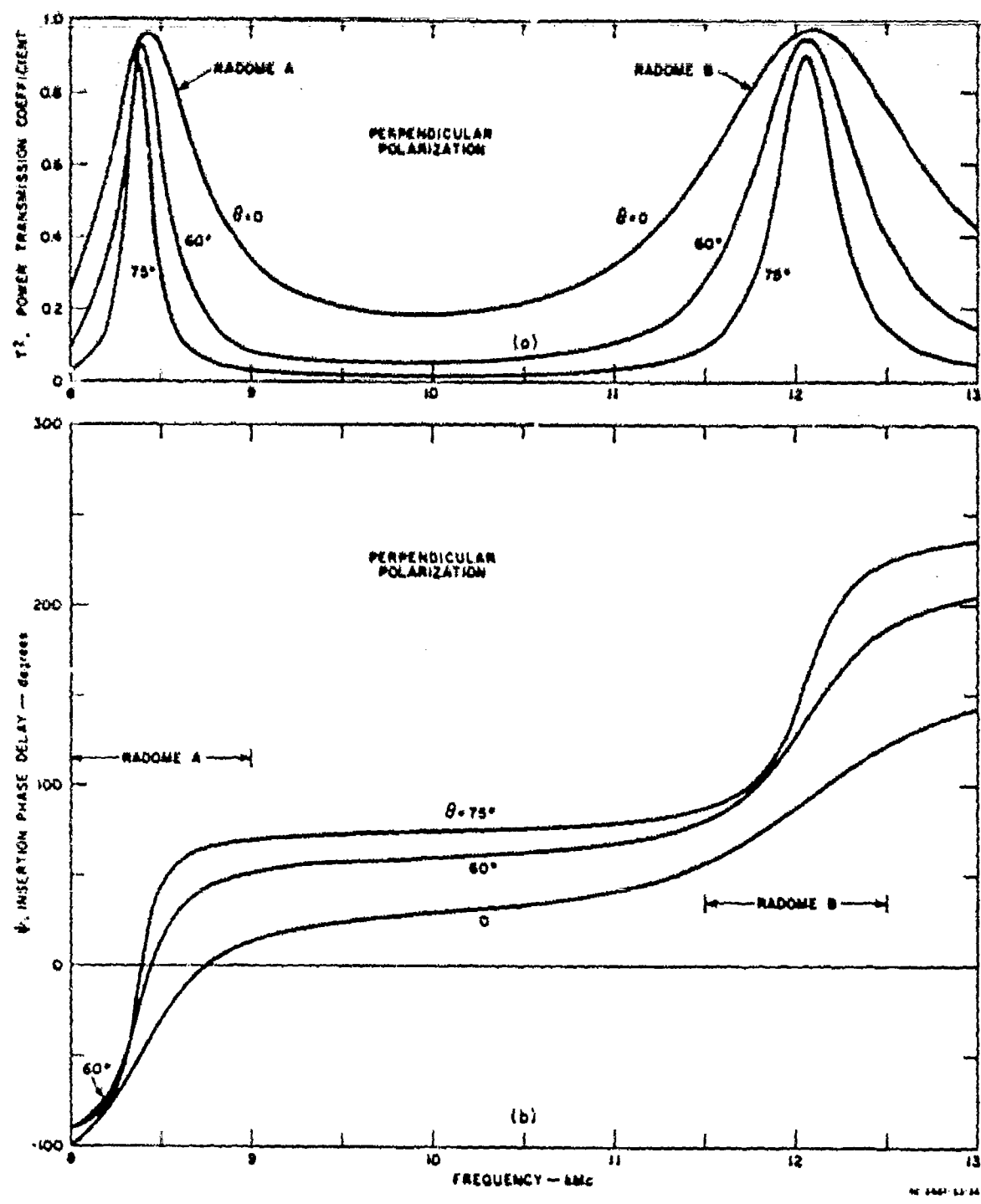


FIG. 21  
CALCULATED PERFORMANCE OF A RESONANT-WALL RADOME SAMPLE FOR  
PERPENDICULARLY POLARIZED WAVES

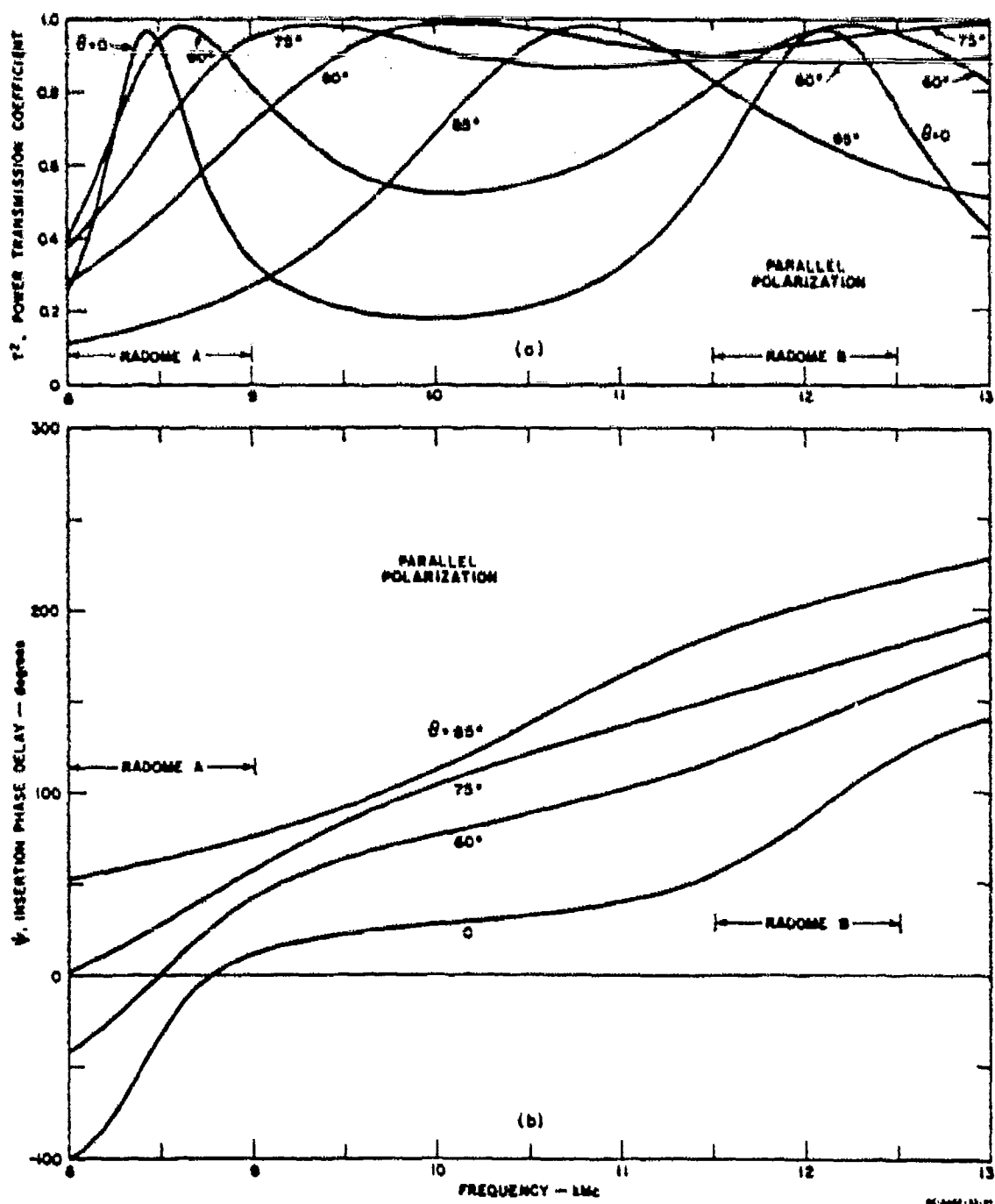


FIG. 22  
CALCULATED PERFORMANCE OF A RESONANT-WALL RADOME SAMPLE FOR  
PARALLEL-POLARIZED WAVES

The incidence angle where the transmission between resonances is maximum corresponds to Brewster's angle for uniform dielectrics, i.e., the characteristic admittance of the metal plate and that of free space are equal.\* As a result of this behavior of the resonance frequencies, the maximum incidence angle at which Radome A gives high transmission for both parallel and perpendicularly polarized waves at a fixed frequency is about 70 degrees. This maximum incidence angle for Radome B, on the other hand, is about 80 degrees.

At present, it does not appear possible to completely eliminate the variation of the resonance frequencies with changing incidence angle.<sup>†</sup> It is likely, however, that the resonance frequencies of resonant-wall radomes using different design parameters than the particular examples presented here, would vary in a slightly different manner with incidence angle. Thus it might be possible to design resonant-wall radomes to have electrical performance that is even better than Radomes A and B. It would be a cumbersome task to empirically determine the optimum design for a radome with as many independent parameters as the resonant-wall radomes. Using the approximate equivalent circuit proposed here, however, the optimum design for a particular application could be determined with a reasonable expenditure of effort.

The calculated curves in the regions near the resonance peaks for perpendicularly polarized waves are compared with measured points for Radome A (first-order resonance) and Radome B (second-order resonance) in Figs. 23 and 24, respectively. It is seen from these figures that the assumed values for the equivalent circuit parameters predict the resonance frequencies within 0.5 percent at the first-order resonance, and 1.3 percent at the second-order resonance. Although these errors are small, closer agreement between calculated and measured performance would be desirable for applications where perpendicularly polarized waves are incident at wide angles, since the bandwidth is small for these waves. It is also seen from Figs. 23 and 24 that the calculated curves satisfactorily

\* For this particular radome sample, and for  $f = 12.2 \text{ kMc}$ ,  $Y_3 = Y_1$  for parallel-polarized waves incident at  $\theta = 76.8^\circ$ .

<sup>†</sup> The variation in resonance frequencies with changing incidence angle and polarization is related to the presence of the reactive discontinuities at the ends of the cavities. For the resonant-wall radomes described here, these discontinuities are inductive in nature. Perhaps if these inductive susceptances were compensated by shunt capacitive susceptances, the wide-angle performance of the radomes could be improved. These capacitive elements might take the form of metal tabs extending from the surface of the metal plate over the end of each cavity, or insulated metal disks of diameter less than  $D$ , bonded to the ends of each dielectric plug. These possibilities have not, however, been investigated.

predict the bandwidth, effect of dissipation loss, and the shift in resonance frequency as functions of the incidence angle and the polarization.

Closer agreement between the calculated curves and the measured points can be obtained by using values for  $B_1$  and  $Y_3$  slightly different from those given by Eqs. (15) and (16). For example, the values of  $C_3$  in Eq. (16) can be reduced in such a way that the calculated values for the resonance frequencies agree with the measured values at either the first-order or the second-order resonance; however, no single value of  $C_3$  will give agreement at both resonances. When the value of  $C_3$  is made less than

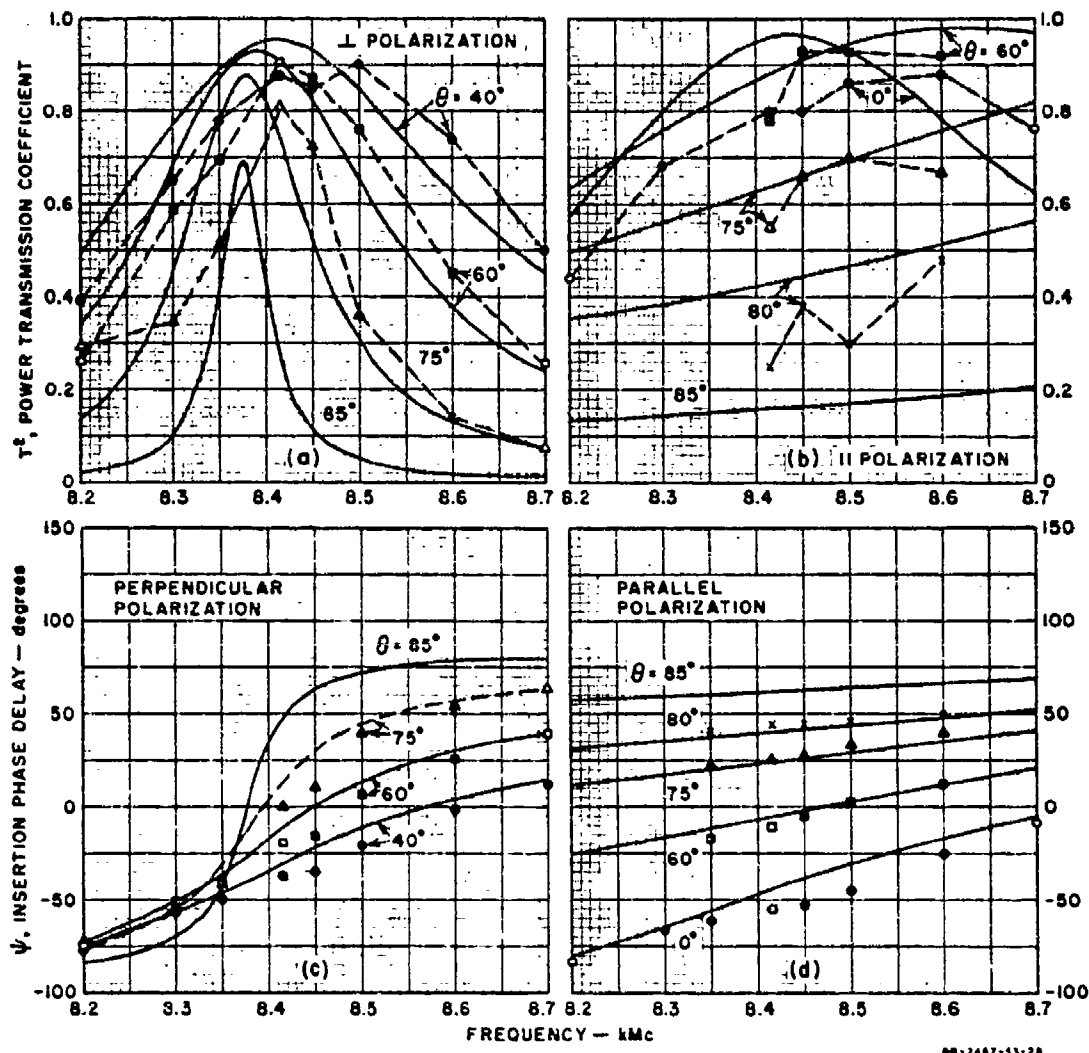


FIG. 23  
COMPARISON OF CALCULATED AND MEASURED PERFORMANCE OF RESONANT-WALL RADOME SAMPLE A (SIMPLEST CIRCUIT)

$C_3 = 1.522$ , in order to obtain better agreement for the resonance frequencies, it is found that the agreement between the calculated and the measured bandwidths deteriorates. Since the bandwidth is determined primarily by the characteristic admittance of the metal plate, it appears that the use of  $C_3 = 1.522$  in Eq. (16) gives a fairly good approximation to  $Y_3$ . Thus it appears that the calculated values for the resonance frequencies differ from the measured values because the values assumed for the reactive discontinuities at the ends of the cavities are inaccurate. It will be recalled that for the curves of Figs. 21 through 24, the nonpropagating

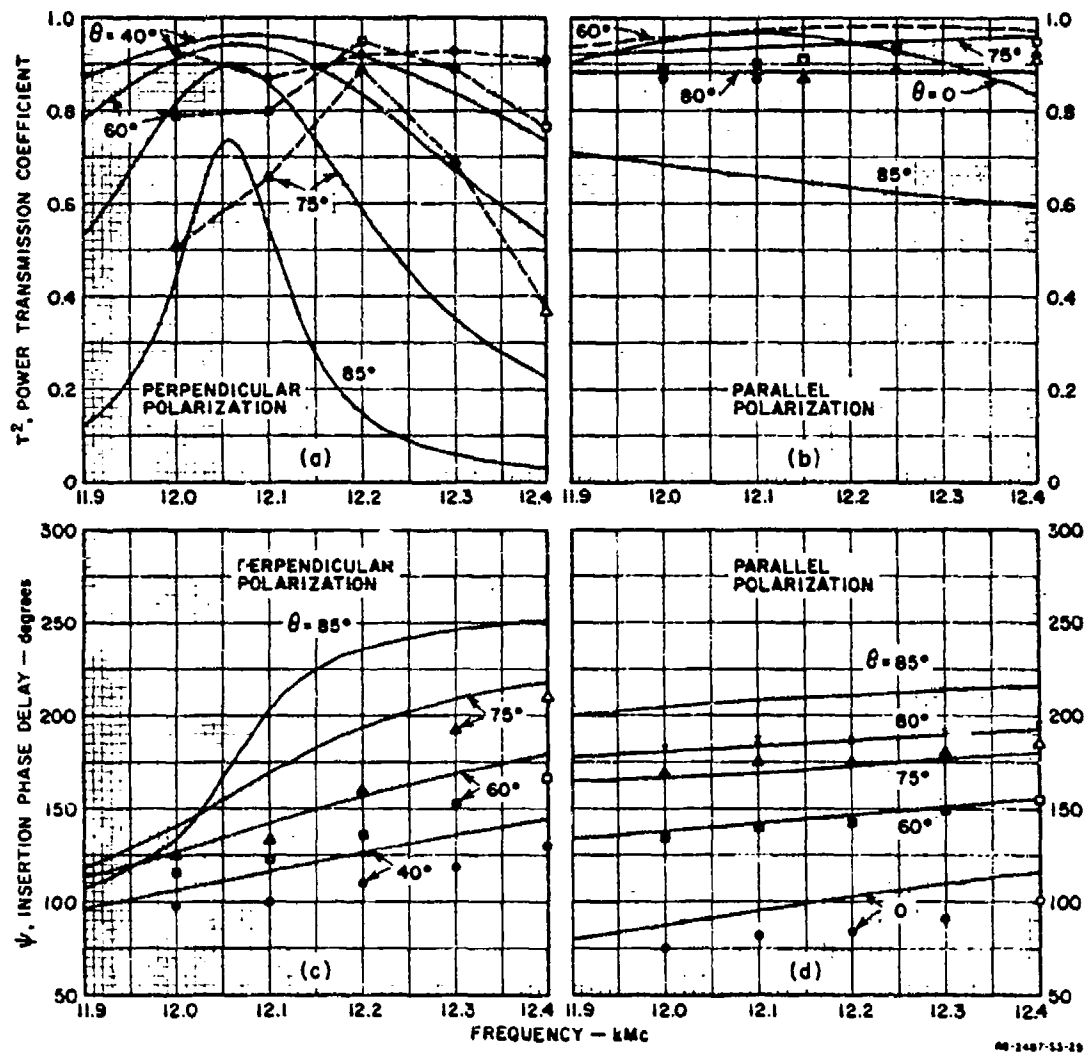


FIG. 24

COMPARISON OF CALCULATED AND MEASURED PERFORMANCE OF RESONANT-WALL RADOME SAMPLE B (SIMPLEST CIRCUIT)

modes inside the ends of the cavities were neglected. These modes can be taken into account by adding a second term to Eq. (15) in calculating  $B_3$ . An alternative is to use Eq. (15) for calculating  $B_3$ , but to shift the reference planes—at which the terminals of the equivalent circuit are considered to exist—out of the planes of the radome panel surfaces. Theoretical formulas do not exist for either of these approaches; however, either the correction term for  $B_3$  or the reference-plane position can be calculated for resonant-wall radome samples whose resonance frequencies have been measured.

Using simple Smith-chart calculations, the reference-plane positions have been evaluated for Radomes A and B, assuming that Eqs. (15) and (16), with  $C_3 = 1.522$ , give the correct values for  $B_3$  and  $Y_3$ . The resonance frequencies measured with perpendicularly polarized waves incident at  $\theta = 75$  degrees were used in these calculations. It was found that for Radome A (first-order resonance) the reference planes are a distance  $\tau = 0.0058 \lambda_{g3}$  inside the radome surfaces. For Radome B (second-order resonance), the reference planes are a distance  $\tau = 0.0074 \lambda_{g3}$  inside the radome surfaces. The location of the reference planes was not determined at other frequencies, but since this quantity is relatively unimportant at frequencies far from resonance, the simplifying assumption was made that  $\tau/\lambda_{g3}$  varies linearly with frequency as given by Eq. (27):

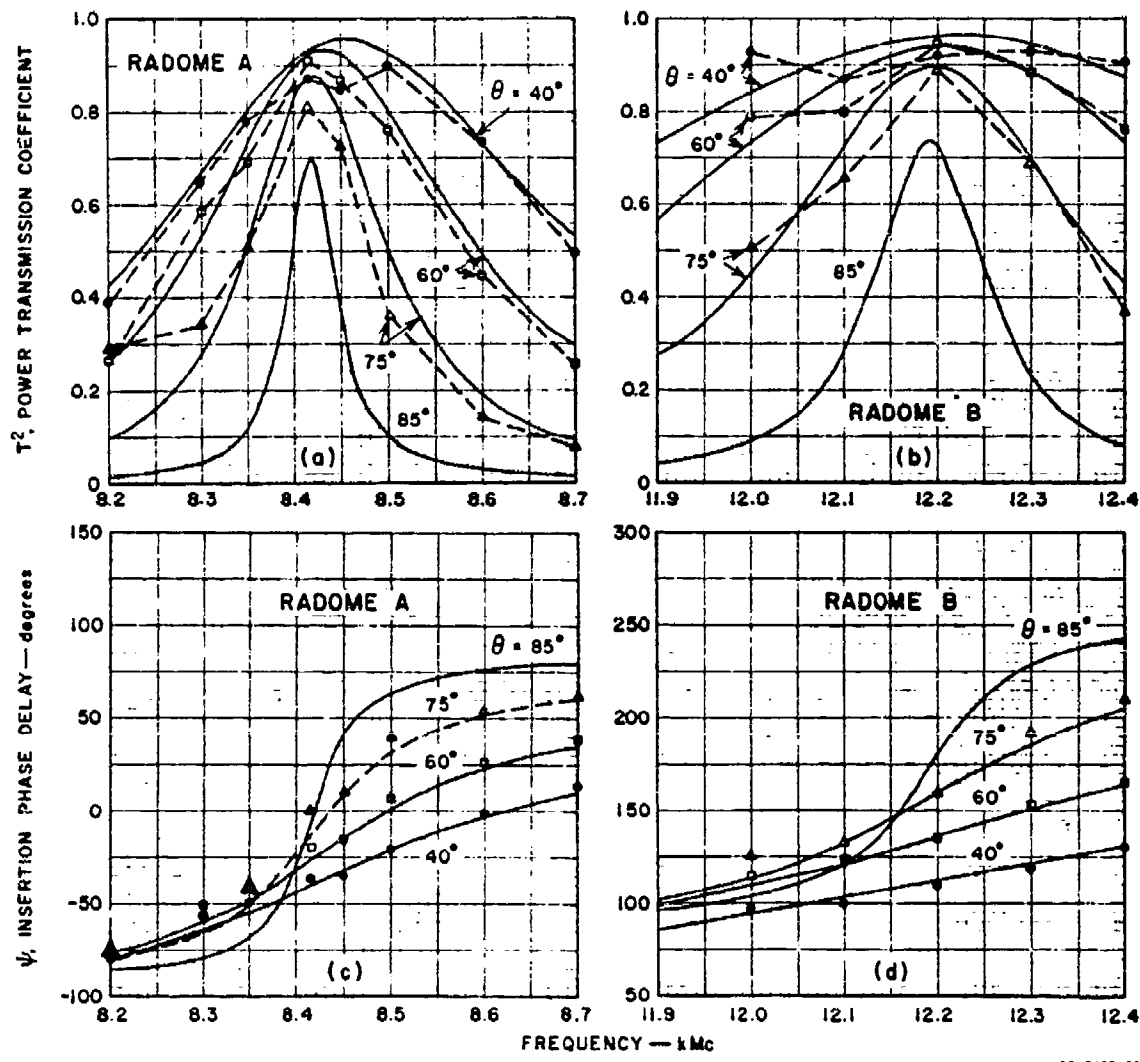
$$\frac{\tau}{\lambda_{g3}} = 0.0022 + 0.0055 \left( \frac{B}{\lambda_3} \right) . \quad (27)$$

It was also assumed that the ratio  $\tau/\lambda_{g3}$  is independent of incidence angle and polarization of the incident waves. The agreement between the calculated and measured electrical performance of Radomes A and B seems to justify this assumption. Shifting the reference planes to within the surfaces of the radome sample is equivalent to calculating the electrical length of the cavities using a value ( $l_3 - 2\tau$ ) in place of the actual physical length,  $l_3$ , of the cavities. Thus, in Eq. (17) and in Fig. 19,  $\phi_3$  should be replaced by  $\phi'_3$ , where

$$\phi'_3 = \phi_3 - 2\pi \frac{2\tau}{\lambda_{g3}} \text{ radians.} \quad (28)$$

The performance calculated taking the reference-plane shift into account is shown by the curves in Fig. 25 for Radomes A and B with

perpendicularly polarized waves incident on them. It is seen that there is good agreement between these calculated curves and the measured points with respect to the values of the resonance frequencies, the shift of the resonances with changing incidence angle, the bandwidth, and the less-than-unity transmission at resonance due to dissipation loss. The calculated curves for parallel-polarized waves incident at  $\theta \geq 60$  degrees were essentially the same as those shown in Figs. 23 and 24, thus they were not repeated.



SC-2487-30

FIG. 25

COMPARISON OF CALCULATED AND MEASURED PERFORMANCE OF RESONANT-WALL RADOME SAMPLES A AND B FOR PERPENDICULARLY POLARIZED WAVES (MODIFIED CIRCUIT)

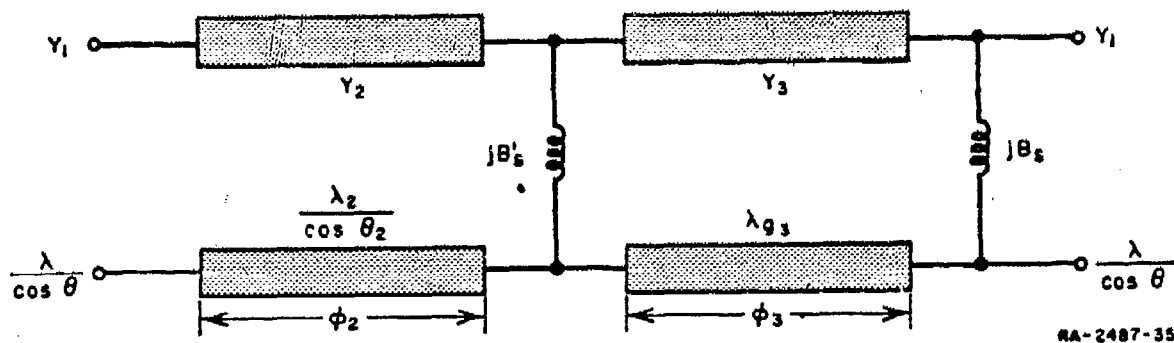
The expression of Eq. (27) gives the shift in the reference planes with sufficient accuracy for Radomes A and B; however, it was possible to obtain this expression only after the radomes were built and their resonance frequencies measured. The empirically derived relation in Eq. (27) does not generally apply to other resonant-wall radomes. For example, the reference-plane shift calculated at the second-order resonance of one of the waveguide-samples of resonant-wall radomes described in Table 1 was about twice the value given by Eq. (27).\* It should be emphasized, however, that the shift in the reference planes is a second-order correction on the equivalent circuit required in order to shift the calculated resonance frequencies slightly. If the reference planes are taken at the surfaces of the radome, the calculated curves still predict the bandwidth, the effect of dissipation loss, and the shift in resonance frequency with changes in incidence angle, with sufficient accuracy.

It is seen from the above discussion that the simple equivalent circuit of Fig. 19, together with Eqs. (15) through (26), is useful for calculating the performance of resonant-wall radomes that do not have dielectric layers in contact with either surface. For example, calculations based on this equivalent circuit could be used to determine the set of design parameters that gave the best performance for a particular application. A test panel could then be built and tested, and the thickness modified slightly to obtain the required resonance frequency. The tolerance required on a particular radome could also be determined by calculations based on the equivalent circuit.

#### RESONANT-WALL RADOMES WITH DIELECTRIC ON ONE SURFACE

Following the same line of reasoning as was presented on pp. 38 to 42, the equivalent circuit of a resonant-wall radome with dielectric on one surface can be shown to be as in Fig. 26. To the circuit of Fig. 19 has been added a length of transmission line of characteristic admittance  $Y_2$  and electrical length  $\phi_2$  to account for the dielectric layer. The fact that the reactive discontinuities at the two surfaces of the perforated metal plate are not equal has also been taken into account. The parameters  $B_s$ ,  $Y_3$ ,  $\phi_3$ , and  $\alpha_3$  are the same as for a resonant-wall radome without

\* Small errors in the radome dimensions, and in the dielectric constant of the material filling the cavities, can result in relatively large errors in the calculated shift in the reference planes. It is not felt, however, that this completely accounts for the difference noted for the two radome samples.



RA-2487-35

FIG. 26

**EQUIVALENT CIRCUIT OF RESONANT-WALL RADOMES WITH DIELECTRIC  
IN CONTACT WITH ONE SURFACE**

surface dielectric, and can be calculated approximately from Eqs. (15) through (21).

The susceptance  $B'_s$  at the interface between the metal plate and the dielectric layer can be calculated approximately using Eq. (29):

$$B'_s = - \frac{A}{377} \cdot \frac{3}{2\pi} \cdot \left(\frac{s}{D}\right)^2 \left(\frac{\lambda_2}{D}\right) \left[1 - \left(\frac{1.706 D}{\lambda_2}\right)^2\right] \quad (29)$$

where

$\lambda_2 = \lambda/\sqrt{\epsilon_2}$  = wavelength in the dielectric layer in contact with the surface of the metal plate

$\epsilon_2$  = relative dielectric constant of the dielectric in contact with the surface of the metal plate.

The parameters  $A$ ,  $s$ ,  $D$ , and  $\lambda$  are as defined under Eq. (15). Equation (29) is just half the theoretical formula for the susceptance of a zero-thickness perforated metal sheet in a uniform dielectric of relative dielectric constant  $\epsilon_2$ . It was shown earlier in the report that Eq. (15) gave a fairly good approximation to the susceptance at the surfaces of a resonant-wall radome without surface dielectric. It was shown in Ref. 1, however, that the theoretical formula for a thin perforated metal sheet becomes less accurate as the aperture diameter becomes an appreciable fraction of the wavelength in the medium surrounding the sheet. Thus, Eq. (29) is not expected to give an accurate approximation to the susceptance at the surface of the metal plate next to the dielectric layer.

The susceptance  $B_2'$  is smaller than  $B_2$ , thus the percent accuracy required is not as great for  $B_2'$  as for  $B_2$  for a given accuracy of the calculated electrical performance.

The characteristic admittance of the dielectric layer is taken as the ratio of the magnetic and electric field components parallel to surface of the dielectric, and is

$$Y_2 = \frac{\sqrt{\epsilon_2}}{377} \cos \theta_2 \quad (30)$$

for waves polarized perpendicular to the plane of incidence, and

$$Y_2 = \frac{\sqrt{\epsilon_2}}{377 \cos \theta_2} \quad (31)$$

for waves polarized parallel to the plane of incidence. The angle of incidence,  $\theta_2$ , measured in the dielectric between the incident ray and the normal to the radome surface is given by Eq. (32):

$$\theta_2 = \sin^{-1} \left( \frac{\sin \theta}{\sqrt{\epsilon_2}} \right) \quad . \quad (32)$$

The product of the complex propagation constant within the dielectric and the physical thickness,  $l_2$ , of the dielectric is

$$\gamma_2 l_2 = a_2 l_2 + j\phi_2 \quad (33)$$

where

$$a_2 = \frac{\pi \tan \delta_2}{\lambda_2 \cos \theta_2} \quad (34)$$

$$\phi_2 = \frac{2\pi l_2 \cos \theta_2}{\lambda_2} \quad \text{radians} \quad (35)$$

$a_2$  = attenuation constant in the dielectric layer

$\tan \delta_2$  = loss tangent of the dielectric layer

$\phi_2$  = electrical thickness of the dielectric layer.

The power transmission coefficient and insertion phase delay of a resonant-wall radome with dielectric in contact with one surface can be readily calculated from its equivalent circuit. A convenient method for performing these calculations is to substitute the general circuit parameters of the radome, as found from the matrix product of Eq. (36), into Eqs. (23) and (24):

$$\begin{bmatrix} A & B \\ C & D \end{bmatrix} = \begin{bmatrix} \cosh \gamma_2 l_2 & \frac{\sinh \gamma_2 l_2}{Y_2} \\ Y_2 \sinh \gamma_2 l_2 & \cosh \gamma_2 l_2 \end{bmatrix} \begin{bmatrix} 1 & 0 \\ jB'_s & 1 \end{bmatrix} \\ \times \begin{bmatrix} \cosh \gamma_3 l_3 & \frac{\sinh \gamma_3 l_3}{Y_3} \\ Y_3 \sinh \gamma_3 l_3 & \cosh \gamma_3 l_3 \end{bmatrix} \begin{bmatrix} 1 & 0 \\ jB_s & 1 \end{bmatrix} . \quad (36)$$

These calculations were carried out for an 0.223-inch-thick layer of alumina ceramic on one surface of the perforated metal plate also used as Radomes A and B. The resulting flat-strip radome sample will be designated Radome C in this discussion. The calculated electrical performance of Radome C is compared in Fig. 27 with the performance of the sample measured in the parallel-plate transmission line described in Appendix A. It is seen that the calculated resonance frequency for perpendicularly polarized waves incident at wide angles is about 1.8 percent lower than the measured value. This discrepancy is probably due to the fact that the nonpropagating waves within the radome cavities were neglected for these calculations, and Eq. (29) does not accurately account for the nonpropagating waves within the dielectric near the surface of the metal plate.

Examination of Fig. 27 shows that there is considerable scatter in the measured points, and that the data could not be reproduced. This is attributed to poor contact between the metal portion of the sample and the parallel-plate transmission line, which would prevent proper mirror-imaging of the sample in the surfaces of the transmission line. It was found that the joints in the dielectric layer (which consists of four strips of ceramic cemented end to end) were slightly misaligned. This would prevent the surfaces of the transmission line from making frequent contact with the perforated plate, even though the height of the individual pieces of ceramic was slightly less than that of the perforated metal plate. This

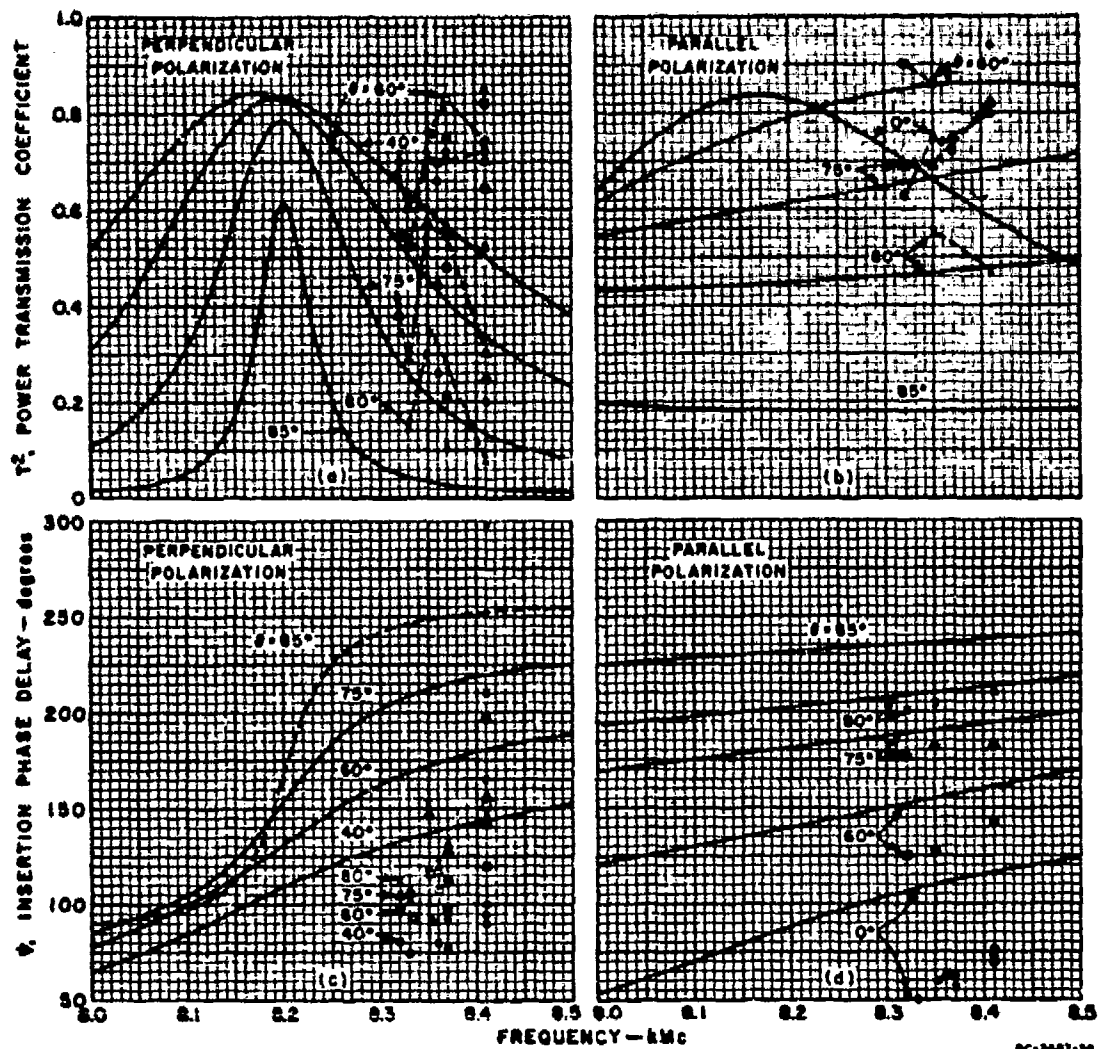


FIG. 27

COMPARISON OF CALCULATED AND MEASURED PERFORMANCE OF  
RESONANT-WALL RADOME SAMPLE C

defect in the sample was not discovered until the series of measurements was completed. Thus, the available data indicate little more than that the resonance frequency for perpendicularly polarized waves incident at wide angles is about 8.35 kMc. The dimensions of the sample are given in terms of wavelength at this frequency in Table 4. Because of the poor quality of the measured data, the remaining discussion concerning this radome will be based on the calculated performance.

Figure 27 shows that the resonance frequency of this resonant-wall radome with dielectric on one surface changes only slightly with incidence

**TABLE 4**  
**DIMENSIONS OF RESONANT-WALL RADOME**  
**SAMPLE C IN TERMS OF WAVELENGTH**

Measured resonance frequency at wide incidence angles (perpendicular polarization)	8.35 kMc
Free-space wavelength at resonance, $\lambda$	1.414 inches
Wavelength in the dielectric at resonance, $\lambda_2, \lambda_3$	0.481 inch
Guide wavelength in cavities at resonance, $\lambda_{g3}$	1.111 inches
Diameter of cavities, $D$	$0.650 \lambda_3$
Thickness of metal plate, $l_3$	$0.520 \lambda_3$
Electrical length of cavities, $l_3/\lambda_{g3}$	0.225
Electrical thickness of dielectric layer at normal incidence, $l_2/\lambda_2$	0.464
Center-to-center spacing of cavities, $s$	$0.255\lambda = 0.749 \lambda_2$
Thickness of radome, $L = l_2 + l_3$	$0.334 \lambda$

angle when the incident waves are polarized perpendicular to the plane of incidence. For waves polarized parallel to the plane of incidence, however, the resonance frequency changes greatly as the incidence angle varies. This variation in resonance frequency is similar to that observed for the resonant-wall radomes without surface dielectric. This variation in resonance frequency limits somewhat the range of incidence angles over which high transmission can be obtained for waves of any polarization. At a frequency of 8.23 kMc, the calculated power transmission is greater than 70 percent for either perpendicularly or parallel polarized waves incident at angles up to about 70 degrees.

Also at 8.23 kMc, the variation in insertion phase delay as the incidence angle varies from 0 to 70 degrees is 69 degrees for perpendicularly polarized waves, and 74 degrees for parallel-polarized waves. These variations are 9 degrees and 4 degrees less, respectively, than the variation in the electrical thickness of a layer of air of the same physical thickness as the radome. On the basis of the particular examples considered in this report, it would appear that for resonant-wall radomes of a given total physical thickness, the boresight error would be slightly smaller for a radome with dielectric in contact with one surface of the metal plate than for a radome without surface dielectric.\* The boresight error of

\* It was shown previously that the insertion phase delay of Radomes A and B varied more with changes in the angle of incidence than does the electrical thickness of an air layer of the same physical thickness.

either resonant-wall radome configuration would probably be slightly greater than that of a uniform-dielectric radome of the same physical thickness.

Comparing Figs. 15 and 18 with Fig. 28, it is seen that the 3-db bandwidth of Radome C for perpendicularly polarized waves is slightly greater than that of Radome A, but smaller than that of Radome B. The bandwidth for at least 70-percent power transmission of either perpendicularly or parallel-polarized waves is smaller for Radome C than for both Radomes A and B. Since the physical thickness of Radome C is of the same order as that of a conventional uniform-dielectric, full-wavelength radome, it is of interest to compare the bandwidths of the two types of radomes. For perpendicularly polarized waves incident at wide angles, it is found that the 3-db bandwidth of Radome C is smaller by a factor of 0.34 than that of a full-wavelength radome with  $\epsilon = 8.66$ .

It is worth noting that most radomes, including conventional half-wavelength radomes, full-wavelength radomes, A-sandwich radomes, multilayer radomes, and Radomes A and B in this report are physically and electrically symmetrical about the midplane of each radome. Thus, when the same medium is present on both sides of the radome (usually air), these symmetrical radomes have low reflection coefficients at their frequencies of maximum transmission. For radomes that are not symmetrical about their midplane, such as Radome C, the reflection coefficient is not necessarily low under conditions of maximum transmission. The calculated power reflection coefficient,  $R^2$ , of Radome C is plotted at the bottom of Fig. 28, from which it is seen that up to 11 percent of the incident power is reflected from the radome at its resonance frequency. Off resonance, of course, the reflection will be higher. This curve and the curve of  $T^2$  at the top of Fig. 28 do not apply at a fixed frequency, but rather at the resonance frequency, which is also a function

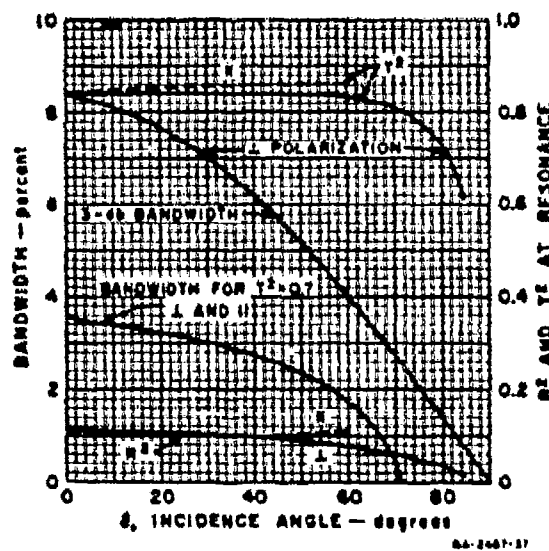


FIG. 28

CALCULATED POWER REFLECTION AND  
TRANSMISSION OF RESONANT-WALL RADOME  
SAMPLE C

of the incidence angle. The power reflection coefficient was calculated by substituting Eq. (25), (26), and (36) into Eq. (37):

$$R^2 = \left| \frac{A + BY_1 - C/Y_1 - D}{A + BY_1 + C/Y_1 + D} \right|^2 \quad . \quad (37)$$

The calculated transmission of Radome C at resonance, as shown in Fig. 28, is lower than that of Radomes A and B, as shown in Figs. 15 and 18. Near normal incidence, this can be mostly accounted for by the relatively high reflection from Radome C. At wide angles of incidence, the difference in the calculated transmission coefficients is largely due to the higher dissipation loss in the thickest radome, Radome C.

## SECTION III

### OTHER METAL-LOADED RADOMES

#### CERAMIC A-SANDWICH RADOMES

One of the objections to the use of ceramic radome materials to obtain high-temperature stability and good rain-erosion resistance is the relatively great weight of these materials. A ceramic A-sandwich radome, consisting of dense ceramic skins separated by a foamed ceramic core, would have a higher strength-to-weight ratio than a uniform, dense ceramic radome, although its strength would not be as great. The strength of these A-sandwich radomes might be increased by embedding thin perforated metal sheets or wire grids within them.

It was shown previously that it is electrically feasible to embed wire grids in A-sandwich radomes with relative dielectric constants of  $\epsilon_r = 4.5$  for the skins, and  $\epsilon_r = 1.3$  for the core. The calculations presented in Ref. 1 showed that there would be electrical advantages to the use of wire grids in A-sandwich radomes, and it was indicated that there might also be mechanical advantages. A brief investigation was conducted on the present contract to determine the electrical feasibility of using metal inclusions in A-sandwich radomes using dielectric constants typical of dense ceramic skins and foamed ceramic cores.

Sections of A-sandwich radomes containing perforated metal sheets and wire grids are illustrated in Fig. 29. In this figure, the metal inclusions are shown at the skin-to-core interfaces; however, they could also be embedded within the skins or slightly within the core. The perforated metal sheets might be better from the mechanical standpoint since they provide more nearly uniform strength in all directions in the plane of the sheet than do wire grids. For calculating the electrical performance, however, the wire grids are better since accurate equivalent-circuit formulas are available. The equivalent circuit parameters of perforated metal sheets located at or near the interface between two dielectrics could be measured. This information could then be used to design and evaluate A-sandwich radomes containing perforated metal sheets. The investigation described here did not go into that great detail.

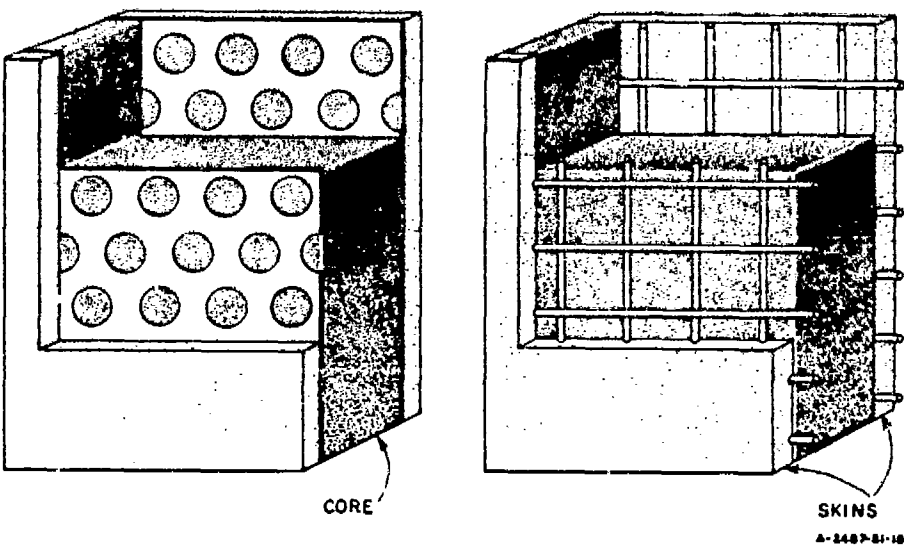


FIG. 29  
A-SANDWICH RADOMES CONTAINING PERFORATED METAL SHEETS AND WIRE GRIDS

The dependence of power transmission coefficient on incidence angle and polarization has been determined approximately for a few dissipationless A-sandwich radomes by Smith chart calculations using the half-section analysis technique described previously.<sup>18</sup> Transmission-coefficient curves are shown in Figs. 30 and 31 for the A-sandwich radomes, which contain wire grids at the skin-to-core interfaces, that are described in Tables 5 and 6. Each of these radomes was designed to be matched at a frequency of 9375 Mc for waves of any polarization incident at an angle of 85 degrees.

To simplify these initial calculations it was assumed that the equivalent shunt susceptance of the wire grids, normalized to the characteristic admittance of the core dielectric, varied as

$$\frac{B}{Y_c} = \frac{-K}{\cos \theta_c} \quad (38)$$

for perpendicularly polarized waves, and as

$$\frac{B}{Y_c} = \frac{-K}{\cos \theta_c} \cdot \frac{\cos^2 \theta_s + \cos^2 \theta_c}{2 \cos^2 \theta_s} \quad (39)$$

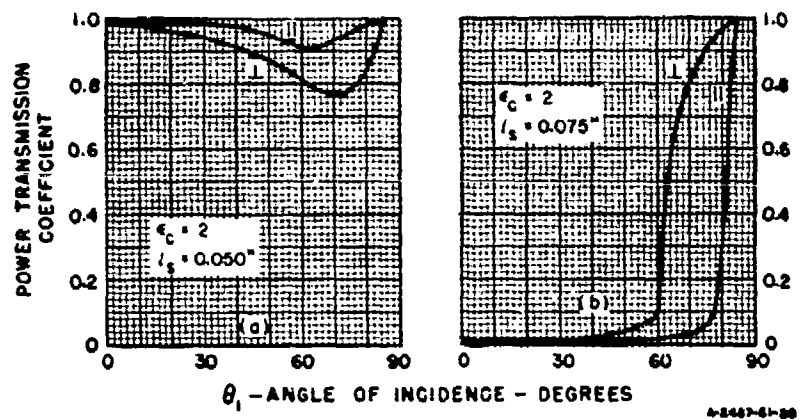
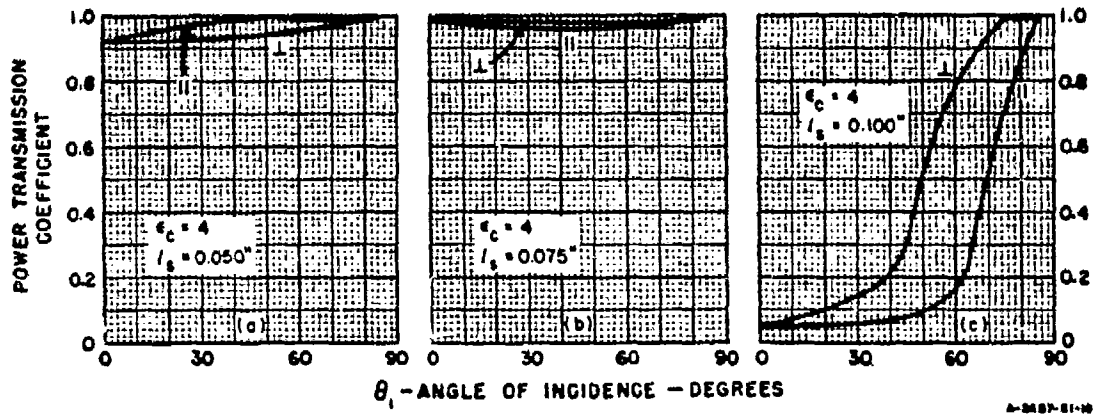


FIG. 31

TRANSMISSION CURVES FOR METAL-LOADED A-SANDWICH RADOMES  
( $\epsilon_c = 2$ )

TABLE 5  
DESIGN PARAMETERS FOR METAL-LOADED A-SANDWICH RADOMES WITH  $\epsilon_c = 4$

	RADOME D	RADOME E	RADOME F
Type of metal inclusions	Wire grids	Wire grids	Wire grids
Position of metal inclusions	At skin-to-core interfaces	At skin-to-core interfaces	At skin-to-core interfaces
Relative dielectric constant, in skins, $\epsilon_s$	9.0	9.0	9.0
in core, $\epsilon_c$	4.0	4.0	4.0
Match angle	85 degrees	85 degrees	85 degrees
Match polarization	$\perp$ and $\parallel$	$\perp$ and $\parallel$	$\perp$ and $\parallel$
Match frequency	9375 Mc	9375 Mc	9375 Mc
Thickness of skins, $l_s$	0.050 inch	0.075 inch	0.100 inch
Thickness of core, $2l_c$	0.273 inch	0.294 inch	0.339 inch
Radome thickness	0.373 inch	0.444 inch	0.539 inch
Normalized shunt susceptance of metal inclusions (at normal incidence), $-K$	-0.85	-2.25	-8.75

TABLE 6  
DESIGN PARAMETERS FOR METAL-LOADED A-SANDWICH RADOMES WITH  $\epsilon_c = 2$

	RADOME G	RADOME H
Type of metal inclusions	Wire grids	Wire grids
Position of metal inclusions	At skin-to-core interfaces	At skin-to-core interfaces
Relative dielectric constant, in skins, $\epsilon_s$	9.0	9.0
in core, $\epsilon_c$	2.0	2.0
Match angle	85 degrees	85 degrees
Match polarization	$\perp$ and $\parallel$	$\perp$ and $\parallel$
Match frequency	9375 Mc	9375 Mc
Thickness of skins, $l_s$	0.050 inch	0.075 inch
Thickness of core, $2l_c$	0.510 inch	0.599 inch
Radome thickness	0.610 inch	0.749 inch
Normalized shunt susceptance of metal inclusions (at normal incidence), $-K$	-1.35	-12.5

for parallel polarized waves, where

$K$  = a constant of proportionality

$\theta_c$  = angle of incidence measured within the core dielectric with respect to the normal to the radome surface

$\theta_s$  = angle of incidence measured within the skin dielectric with respect to the normal to the radome surface.

This assumption amounts to neglecting a correction term in the denominators of Eqs. (38) and (39). This correction term takes into account the energy stored in the nonpropagating waves corresponding to diffracted waves scattered at imaginary angles, and is a rather involved series depending on wire spacing, incidence angle, and polarization as given in Refs. 9 and 10.

Since the correction term was neglected, it was not necessary to specify any particular wire diameter and spacing in order to make the calculations. Combinations of wire diameter and wire spacing that will give approximately the assumed susceptances at normal incidence, neglecting the correction term, are shown in Fig. 32. These curves were calculated using Eq. (40),<sup>9</sup> and the values of the constant  $K$  given in Tables 5 and 6:

$$K = \left( \frac{s}{\lambda_c} \ln \frac{s}{\pi D} \right)^{-1} \quad (40)$$

where

$D$  = wire diameter

$s$  = center-to-center spacing of the wires in each grid

$\lambda_c$  =  $\lambda/\sqrt{\epsilon_c}$  = wavelength in the core dielectric

$\epsilon_c$  = relative dielectric constant of the core material

$\lambda$  = free-space wavelength.

The difference between the actual susceptibility of these wire grids and the assumed susceptances will increase with increasing incidence angle for perpendicularly polarized waves, and will decrease with increasing incidence angle for parallel polarized waves. The maximum wire spacing for no diffraction within the skin dielectric is 0.315 inch for  $\epsilon_s = 9$  and  $f = 9375$  Mc. As the spacing approaches this maximum value, the curves of

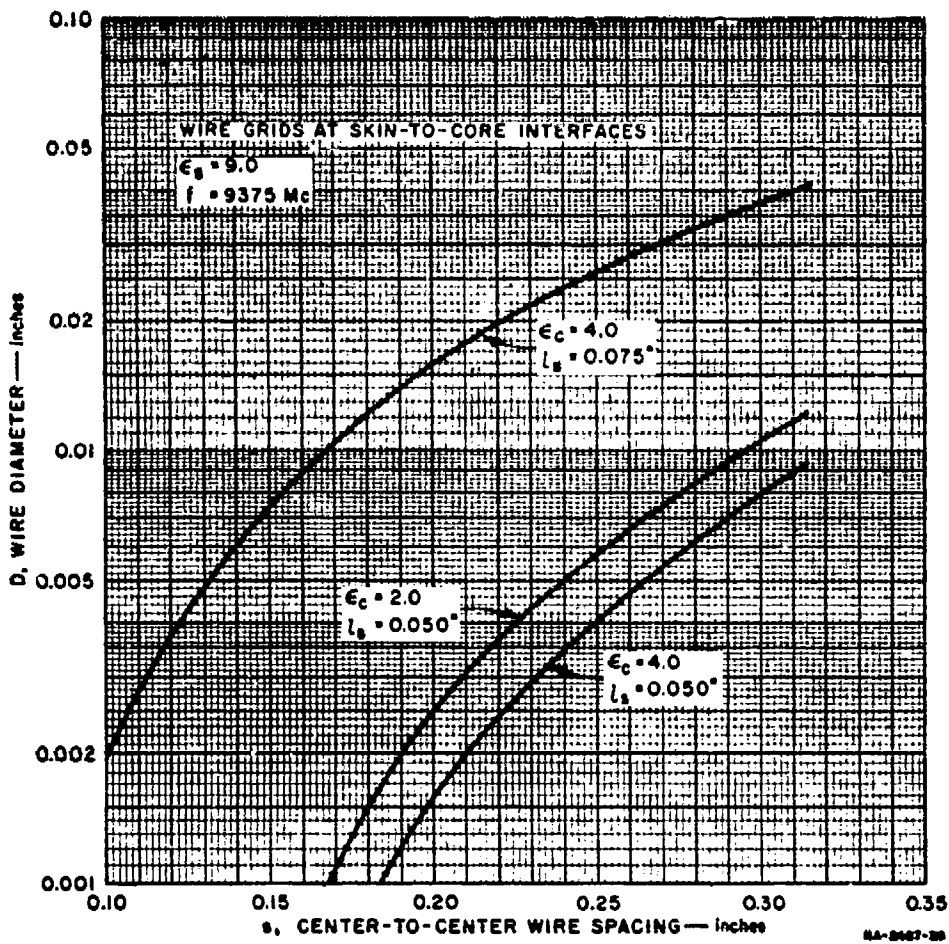


FIG. 32  
APPROXIMATE WIRE GRID DIMENSIONS FOR RADOMES D, E, AND G

Fig. 32 become less accurate since the neglected correction term becomes larger as the wire spacing is increased.

Although the curves of Figs. 30 and 31 were calculated using simplifying assumptions, they are sufficiently accurate that the following conclusions can be drawn:

- (1) A-sandwich radomes loaded with wire grids can be designed to have high transmission for both perpendicularly and parallel polarized waves incident over a wide range of angles, even out to 85 degrees. This is in contrast to conventional unloaded A-sandwich radomes, for which the transmission for parallel polarized waves falls off rapidly as the

- incidence angle exceeds Brewster's angle for the skin dielectric.
- (2) The magnitude of the susceptance, and thus the amount of metal in the grid, increases as the skin thickness increases.
  - (3) There is a limit to the skin thickness that can be used and still obtain high transmission over a wide range of incidence angles; however, it is likely that the skins can be made at least as thick as those of unloaded A-sandwich radomes. For a core dielectric constant  $\epsilon_c = 4$ , this limit on skin thickness is between 0.075 and 0.100 inch, and for  $\epsilon_c = 2$ , it is between 0.050 and 0.075 inch. There will be a corresponding limit on the amount of metal that can be used in A-sandwich radomes.

It is also evident from the calculations carried out on the Smith chart that the metal-loaded A-sandwich radomes will require significantly less stringent tolerances on the core thickness than unloaded A-sandwich radomes using the same dielectric material. Presumably the tolerance on core dielectric constant would also be less stringent for the metal-loaded A-sandwich radomes.

Note that as the skin thickness approaches the maximum value, the equivalent shunt susceptance required of the wire grids becomes sufficiently large in magnitude that it might be practical to use inductive perforated metal sheets rather than wire grids. As pointed out before, however, there are no accurate formulas available for calculating the equivalent circuit parameters of a perforated metal sheet located at or near an interface between two dielectrics. Another structure that shows promise for inclusion in A-sandwich radomes is the self-resonant perforated-metal sheet, discussed in the next section. It would probably be possible to embed more metal in the radomes by using these resonant perforated metal sheets than by using either inductive perforated metal sheets or wire grids.

## RESONANT PERFORATED-METAL SHEETS

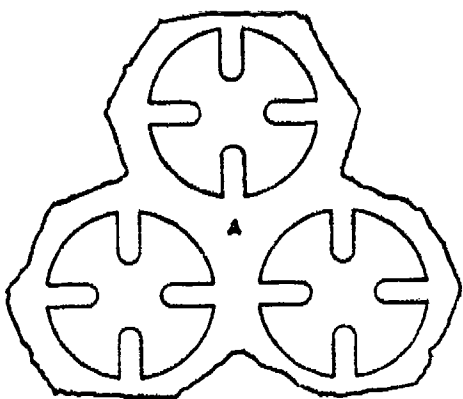
### GENERAL

The design of resonant-wall radomes centers around a thick metal plate, which is electrically equivalent to a distributed-constant resonator, as was explained in Sec. II. Another approach to the design of metal-loaded radomes, which was used extensively in Ref. 1, is to use thin metal structures that are electrically equivalent to shunt susceptances. These

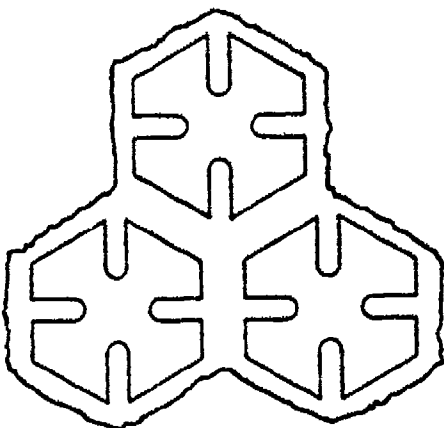
are used to tune a layer or layers of dielectric to obtain the desired resonance frequency and the best electrical performance as a function of incidence angle. A third approach would be to use thin metal structures that are self-resonant, i.e., metal structures that transmit all of the energy incident on them. Ideally, these thin resonant structures could be embedded within a radome without affecting its electrical performance, and the location of the metal structures within the radome would not be critical. An investigation of the mechanical properties of some metal-loaded radomes indicated that thin metal structures might be useful as reinforcement elements in low-density ceramics, such as would be used in the core of an inorganic A-sandwich radome.<sup>11</sup> To investigate the electrical feasibility of using perforated metal sheets for this application, the resonance characteristics of a few samples of perforated metal sheets were measured, as will be described in this section.

Experience with resonant coupling apertures in waveguide has shown that, at least for some aperture shapes, the resonance frequency of an aperture is very nearly the same as the cut-off frequency of a waveguide of the same cross section as the aperture.<sup>12</sup> Assuming this relationship to hold for a perforated metal sheet, initial calculations can be made to determine the amount of metal that can remain between the apertures. The diameter of a resonant circular aperture would be approximately  $D = \lambda_2 / 1.706 = 0.586\lambda_2$ , where  $\lambda_2 = \lambda/\sqrt{\epsilon_2}$  is the wavelength in the medium of relative dielectric constant  $\epsilon_2$  surrounding the metal sheet. In order that the perforated metal sheet not excite diffracted waves, the center-to-center spacing,  $s$ , of the apertures must satisfy Eq. (3). As an example, for a metal sheet embedded in a dielectric with  $\epsilon_2 = 3$ , the incidence angle in the dielectric cannot exceed  $\theta_2 = 35.3$  degrees. Thus, the spacing must satisfy  $s < 0.634\lambda_2$ , and the maximum amount of metal left between the apertures is  $(s - D) = 0.075 s$ . That is, the metal between circular apertures would be only about 7.5 percent of the center-to-center spacing of the apertures. The amount of metal left between the apertures can be increased by decreasing the aperture diameter, and at the same time loading the apertures in some manner to keep the resonance frequency the same.

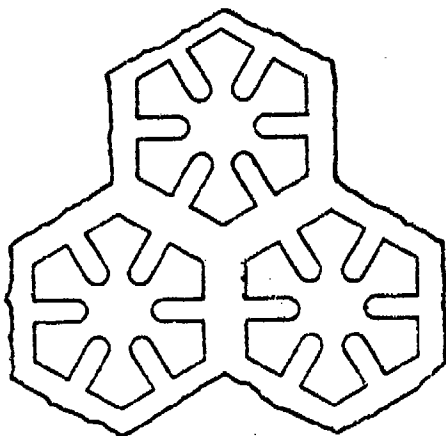
A convenient way to load circular apertures is by ridges, such as shown in Fig. 33(a). Quadruply ridged circular apertures were used in the investigation described here, since the cut-off wavelengths for waveguides of similar shape have been measured and reported in the open literature.<sup>13</sup> Two other aperture shapes that might be considered for the present



(a) QUADRUPLY RIDGED CIRCULAR APERTURES



(b) QUADRUPLY RIDGED HEXAGONAL APERTURES



(c) SEXTUPLY RIDGED HEXAGONAL APERTURES

NS-2467-3

FIG. 33

FIG. 33 shows various ridge-loaded apertures with centers forming hexagonal arrays. Application are also shown in Fig. 33. It is stated on p. 35 of Ref. 11 that perforated metal sheets do not bond to a ceramic as well as do wire grids because of the smooth surfaces of the metal sheets. This difficulty can be partially overcome by placing the apertures closer together than is usually done in metal sheets perforated for other purposes. In addition, the area of the smooth region marked by the letter A in Fig. 33(a) can be reduced slightly by using hexagonal apertures rather than round apertures. There might be electrical advantages to using six rather than four ridges in each aperture, as will be discussed later in this section.

Details of the ridge-loaded aperture shape used in the present investigation are shown in Fig. 34. The cut-off wavelengths of several ridged circular waveguides without fillets at the bases of the ridges, i.e.,

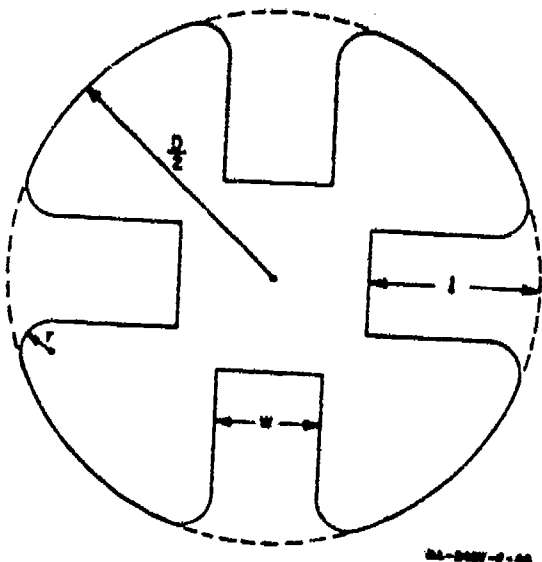


FIG. 34

RIDGE-LOADED CIRCULAR APERTURE SHAPE  
USED FOR SAMPLES

$r = 0$  in Fig. 34, have been measured by Chait and Sakiotis.<sup>13</sup> Their data are replotted in Fig. 35 along with some data taken at Stanford Research Institute.\* The cut-off wavelengths of three ridge-loaded circular waveguides with fillets at the bases of the ridges were also measured at Stanford Research Institute. One of the resonant cavities used to obtain this data is shown in Fig. 36, along with the coupling loops that were inserted through short-circuits at each end of the cavity in order to couple to the cavity. Maximum transmission through the cavity is obtained at frequencies such that the cavity is  $n\lambda_g/2$  long. Here,  $n$  is any positive integer, and  $\lambda_g$  is the guide wavelength in the ridge-loaded circular waveguide

forming the cavity. The coupling loops are sufficiently small that they produce negligible reactive loading at the ends of the cavities, as indicated by the fact that data taken for  $n = 1, 2$ , and 3 gave values of cut-off wavelength that were in agreement within 0.16 percent. The values of cut-off wavelength were calculated using Eq. (41) which is the well known relation between the free-space wavelength, cut-off wavelength, and guide wavelength for any waveguide:

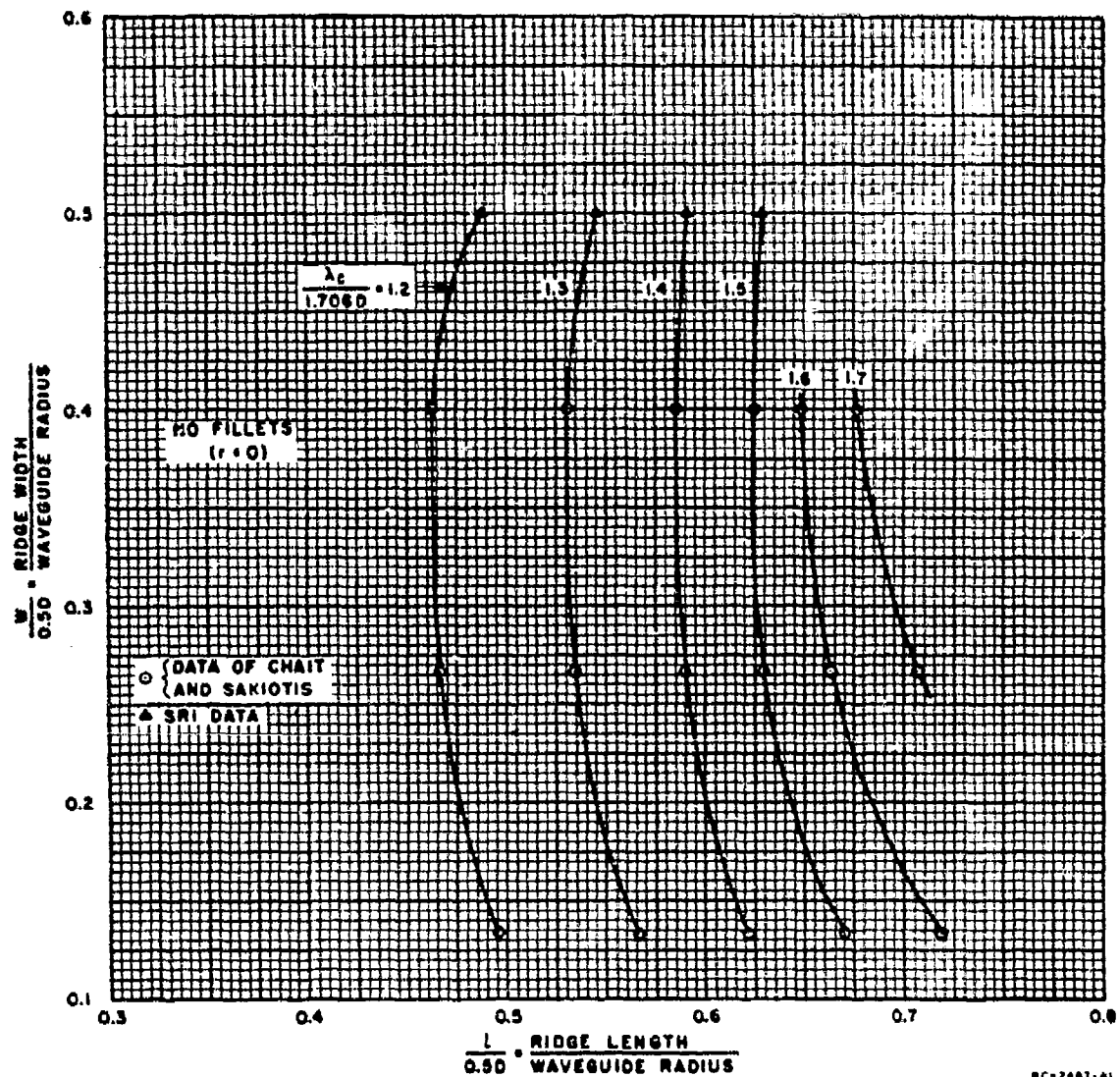
$$\lambda_c = \left[ \frac{1}{\lambda_r^2} - \frac{1}{\lambda_g^2} \right]^{-\frac{1}{2}} \quad (41)$$

where

$\lambda_c$  = cut-off wavelength of the waveguide

$\lambda_r$  = free-space wavelength at the resonance frequency

\* The points shown in Fig. 35 were derived from the measured data in the following manner. Values of cut-off wavelength were measured for several combinations of ridge width and length. These values were plotted as functions of the ridge length, with ridge width as a parameter, and smooth curves were drawn through the points. The combinations of ridge width and length required to give specific values of cut-off wavelength were read from these curves, and then plotted as the points in Fig. 35.



SC-2487-41

FIG. 35  
CUT-OFF WAVELENGTH OF QUADRUPLY RIDGED CIRCULAR WAVEGUIDE

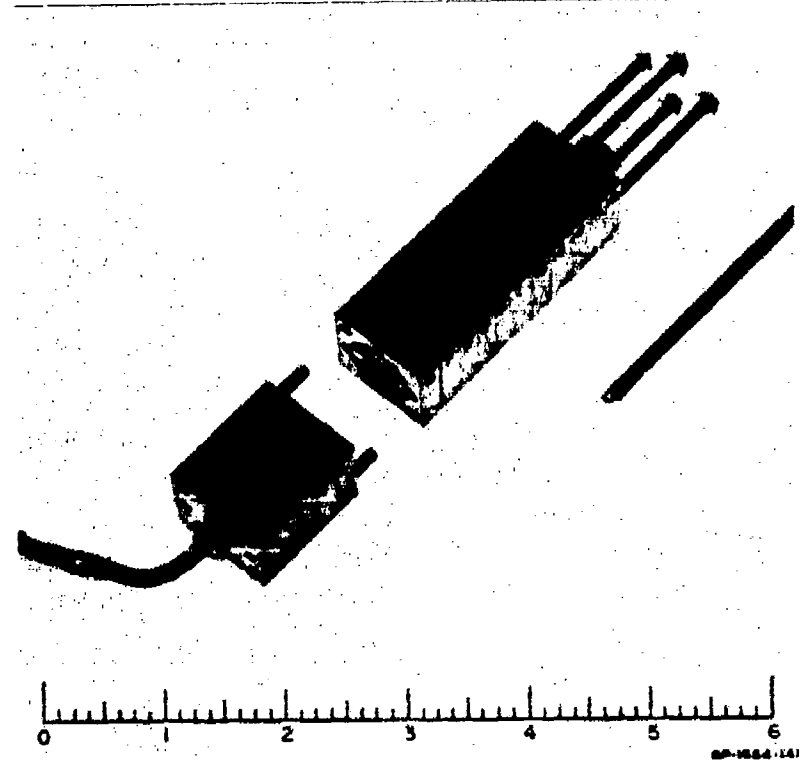


FIG. 36  
WAVEGUIDE CAVITY USING RIDGE-LOADED CIRCULAR WAVEGUIDE

$\lambda_s = 2L/n$  = guide wavelength in the cavity at resonance

$L$  = physical length of the cavity

$n$  = a positive integer.

The results of these measurements are shown in Fig. 37 from which it is seen that the presence of the fillets can change the cut-off wavelength several percent. Points are shown for two values of ridge width, and it is seen that the effect of the fillets depends on the ridge width—and probably also on the ridge length. It was not felt necessary to obtain more detailed data on the effect of the fillets on the cut-off frequencies of waveguides, since there is no exact correspondence between these frequencies and the resonance frequencies of perforated metal sheets.

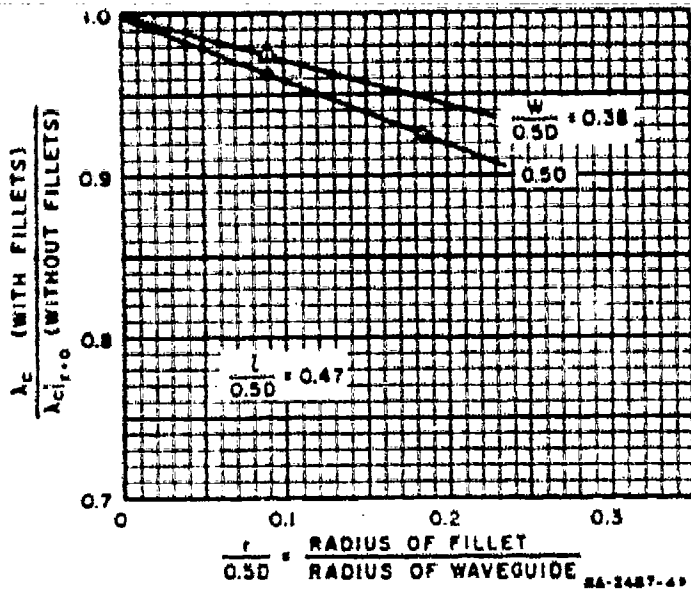


FIG. 37

CORRECTION ON CUT-OFF WAVELENGTH DUE TO THE PRESENCE OF  
FILLETS AT RIDGE BASES

EXPERIMENTAL RESULTS

A few samples of perforated metal sheets were built and their transmission measured as a function of frequency to determine their resonance frequencies and bandwidths. A block diagram of the equipment set-up used for obtaining these data is shown in Fig. 38. The frequency of the signal source was swept as a function of time, and pictures taken of the oscilloscope screen when the sample was between the two horns, and when the sample was removed. For most of the samples, the oscilloscope traces with and without the sample coincide at the resonance frequency, indicating that all the incident energy was transmitted through the sample.

For simplicity in manufacture, the first samples constructed were in the form of flat strips with semicircular apertures along their edges. Three of these are shown in the upper portion of Fig. 39,\* and the sample dimensions are given in Table 7. When mounted in the parallel-plate transmission line described in Appendix A, each sample is mirrored in the

\* The small holes between the apertures were used to dowel the samples to a jig during fabrication. These holes are well below cut-off for all modes that could propagate through them, so their presence should have negligible effect on the electrical performance of the sample.

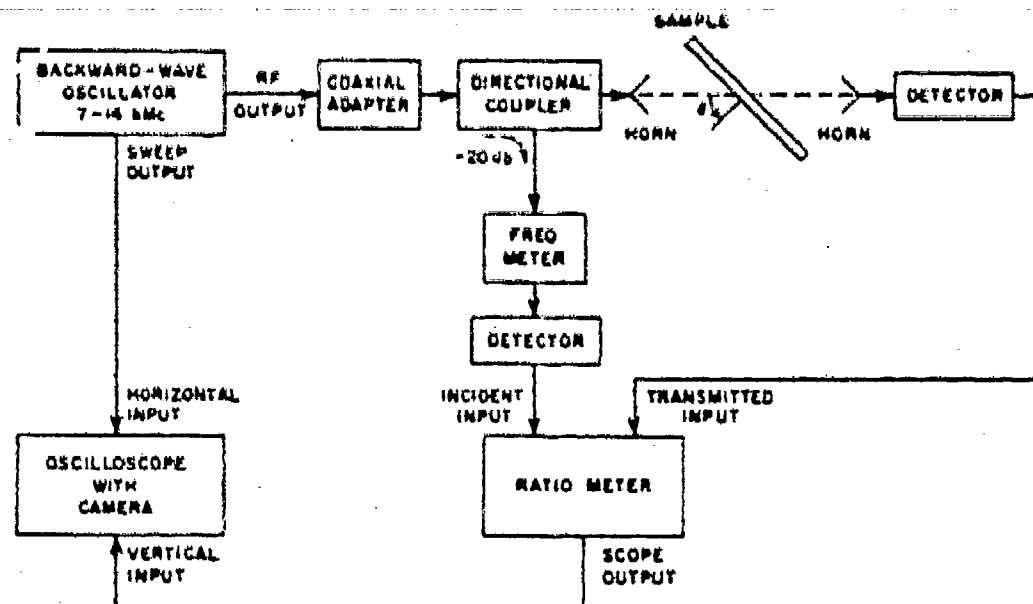


FIG. 38

BLOCK DIAGRAM OF EQUIPMENT TO MEASURE TRANSMISSION VS. FREQUENCY

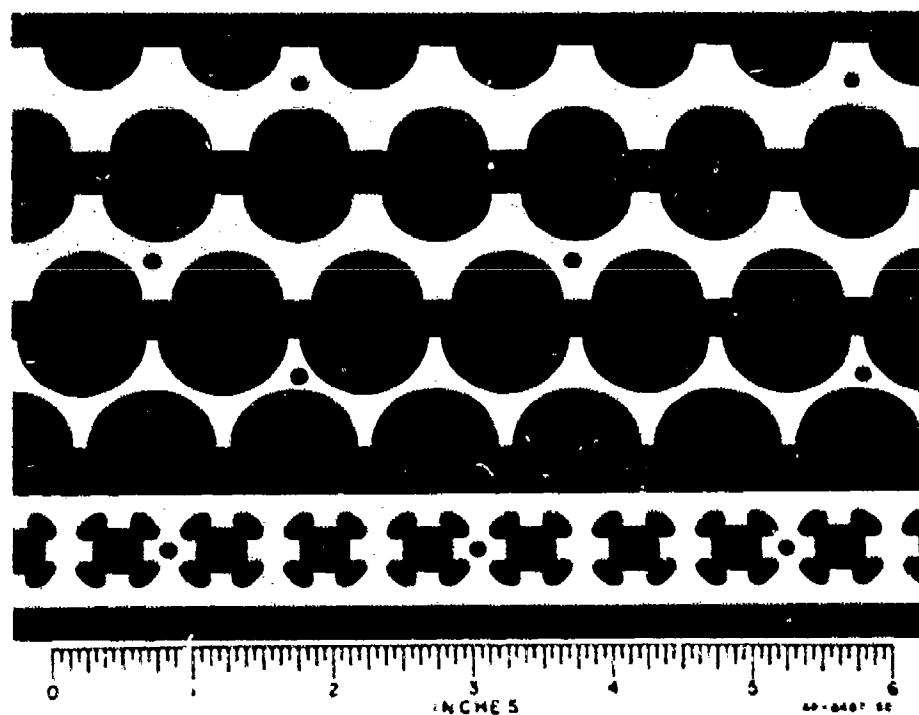


FIG. 39

FLAT-STRIP SAMPLES OF RESONANT PERFORATED-METAL SHEETS

TABLE 7  
DIMENSIONS OF FLAT-STRIP SAMPLES PERFORATED BY CIRCULAR APERTURES

	A	B	C
Layout of apertures	Hexagonal array	Hexagonal array	Hexagonal array
Aperture diameter, $D$	0.750 inch	0.812 inch	0.938 inch
Aperture center-to-center spacing, $s$	1.039 inches	1.039 inches	1.039 inches
Wall thickness between apertures, $(s - D)$	0.289 inch = 0.278 $\pm$	0.227 inch = 0.218 $\pm$	0.101 inch = 0.097 $\pm$
Percent metal remaining between apertures, $100(s - D)/s$	27.8 percent	21.8 percent	9.7 percent
Thickness of samples, $t$	0.080, 0.125, 0.192, and 0.246 inch	0.001, 0.080, 0.125, 0.192, and 0.247 inch	0.102, 0.125, and 0.192 inch
Height of samples	0.900 inch	0.900 inch	0.900 inch
Width of samples	24 inches	24 inches	24 inches

conducting plates to be equivalent to a flat metal sheet perforated by a hexagonal array of circular apertures. For each aperture diameter, samples of different thickness were made, and these were tested individually or in cascade to determine the effect of sample thickness on the electrical performance. The measured resonance frequencies of the samples with 0.812-inch diameter apertures\* are plotted in Fig. 40 for two values of sample thickness. Most of the points for intermediate values of thickness fall on or between the points shown. The curves for  $D = 0.750$  inch are of nearly the same shape, and lie only two percent above these in Fig. 40 even though the cut-off frequency  $f_{c,0}$  of a circular waveguide, is 8.3 percent higher for a diameter of  $D = 0.750$  inch than for  $D = 0.812$  inch. The curves for  $D = 0.938$  inch lie only about three percent below those in Fig. 40 even though  $f_{c,0}$  of a circular waveguide is 13.3 percent lower for  $D = 0.938$  inch than for  $D = 0.812$  inch. Thus, for all the samples tested with circular apertures, the resonance frequency changes about 25 percent as the incidence angle varies 25 degrees.<sup>†</sup> This variation in resonance

\* These samples were tested in air. If a sheet of this type was embedded in a uniform dielectric of relative dielectric constant  $\epsilon$ , all the sample dimensions would be divided by  $\sqrt{\epsilon}$  to obtain the same resonance frequency, and the abscissa in Figs. 40, 41, 43, and 44 would be the incidence angle measured in the dielectric.

† Flat-panel samples perforated by circular apertures and tested in free space also exhibit this rapid variation of resonance frequency as the incidence angle is changed.<sup>14</sup> Associated with this angular-sensitivity of the resonance of both the flat-strip and the flat-panel samples was a focusing of the incident waves, which departed slightly from plane waves. This focusing action was indicated by greater-than-unity transmission coefficient at resonance, up to 180 percent indicated power transmission coefficient being obtained for one flat-strip sample.

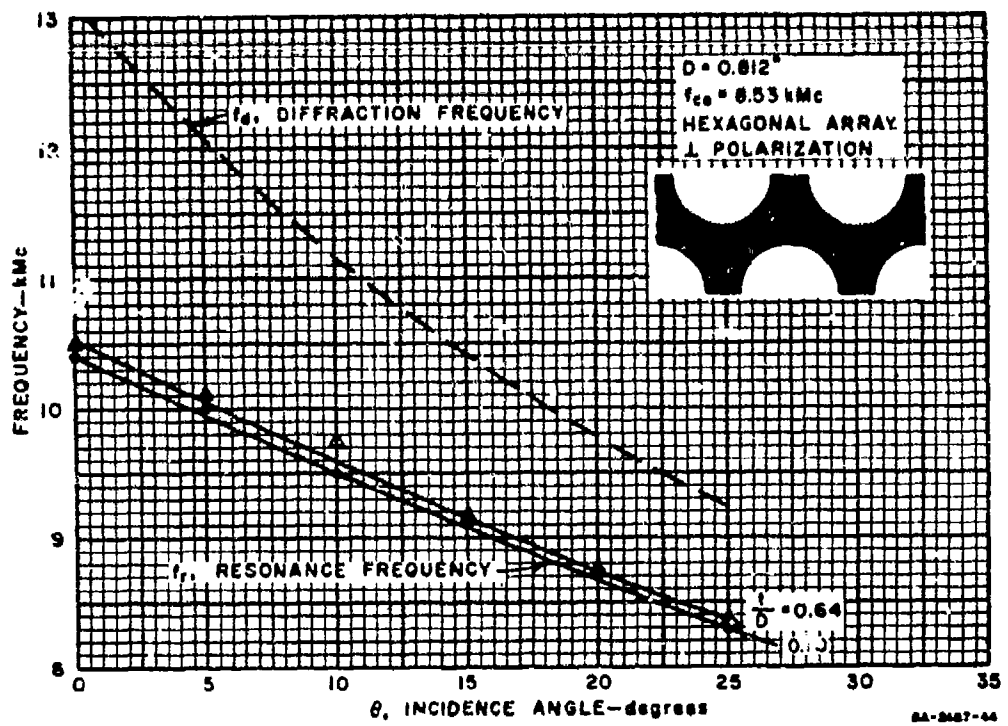


FIG. 40  
MEASURED RESONANCE FREQUENCY OF FLAT METAL STRIPS  
PERFORATED BY CIRCULAR APERTURES

frequency is significantly greater than the bandwidth of the resonance, thus, when operated at a fixed frequency, none of these samples would give high transmission even over the restricted range of incidence angles encountered in a radome dielectric.\* Therefore, it appears that a circle is not a suitable aperture shape to use in resonant metal sheets for the proposed radome application.

Flat-strip samples were also perforated by ridge-loaded apertures. One of these samples is shown at the bottom of Fig. 39, and the dimensions are given in Column A of Table 8. Several thicknesses were tested for a single aperture shape, and resonance frequencies for three thicknesses are shown in Fig. 41(a). For these samples, the resonance frequency is independent of incidence angle out to  $\theta = 30$  degrees, and changes only 2.5 percent as the incidence angle increases to 40 degrees. It is also significant to note that the points shown out to  $\theta = 40$  degrees are within 1.5 percent of the cut-off frequency of a waveguide of the same cross section as the apertures. The value  $f_{c0} = 9.26$  kMc was measured using a

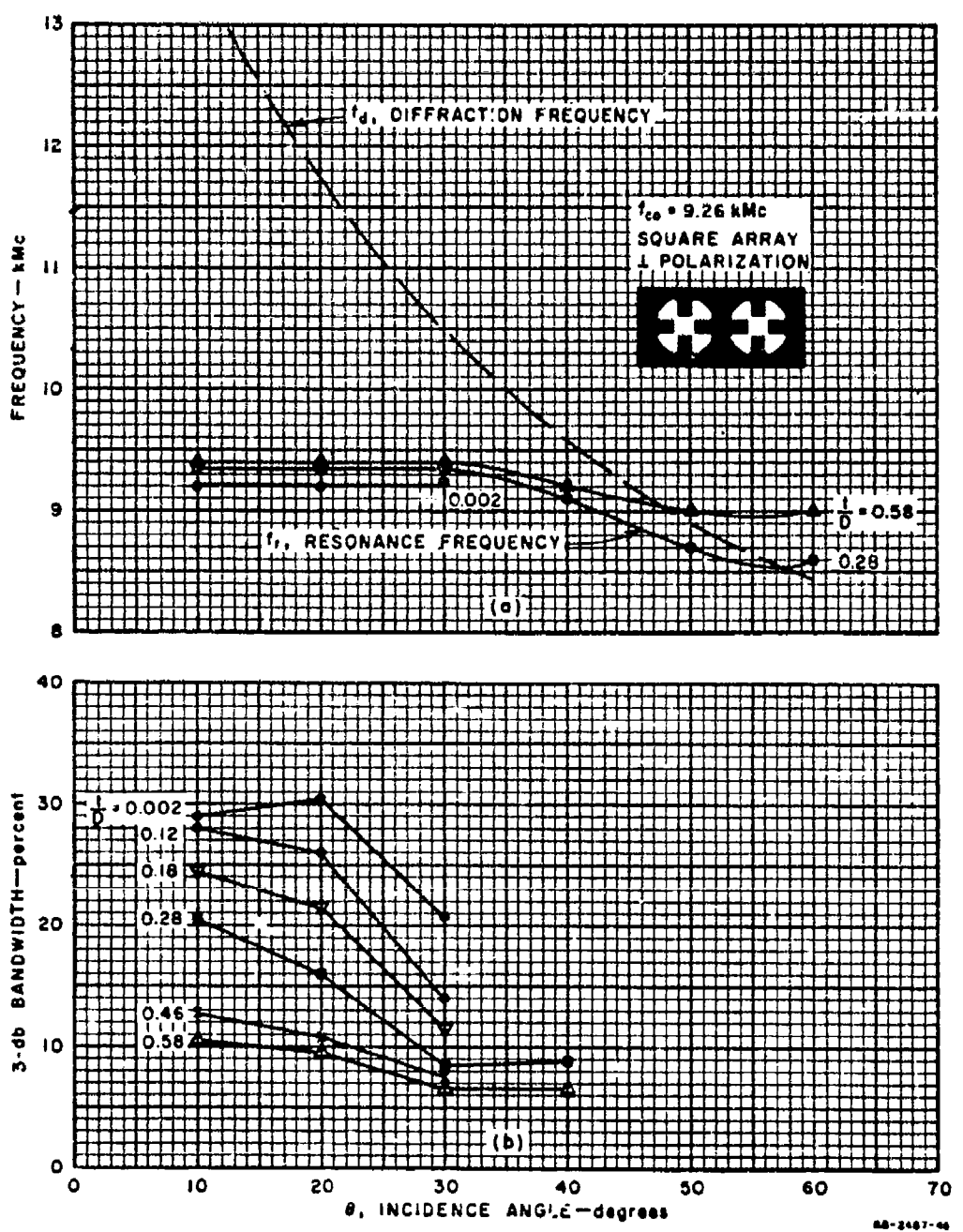
\* The 3-db bandwidth was measured for a few of the flat-strip samples, and was found to be about 10 percent. The bandwidth appeared to be nearly independent of aperture diameter, sample thickness, and the angle of incidence.

TABLE 8  
DIMENSIONS OF SAMPLES PERFORATED BY RIDGE-LOADED CIRCULAR APERTURES

	A	B
Sample type	Flat-strip	Flat-panel
Shape of aperture	Quadruply ridged circles	Quadruply ridged circles
Layout of apertures	Rectangular array	Hexagonal array
Aperture diameter, $D$	0.688 inch	0.500 inch
Ridge width, $w$	0.172 inch = 0.25 $D$	0.077 inch = 0.154 $D$
Ridge length, $l$	0.162 inch = 0.236 $D$	0.161 inch = 0.322 $D$
Fillet radius, $r$	0.062 inch = 0.091 $D$	0.031 inch = 0.062 $D$
Aperture center-to-center spacing, $s$	0.750 inch	0.688 inch
Ratio $(s - D)/s$	0.083	0.273
Minimum width of metal between apertures	0.146 inch = 0.195 $s$	0.188 inch = 0.273 $s$
Thickness of samples, $t$	0.084, 0.124 and 0.192 inch	0.064 inch
Height of sample	0.900 inch	12 inches
Width of sample	24 inches	24 inches

waveguide cavity similar to that shown in Fig. 36. The dashed curve in Fig. 41(a) shows the lowest frequency,  $f_d$ , for which diffracted waves can be radiated from the sample, i.e.,  $f_d$  is the frequency for which the inequality of Eq. (3) becomes an equality. For the measured points lying below the dashed curve, 100-percent transmission was obtained at the resonance frequency of each of these samples. For the points above the dashed curve, however, only 25 to 50 percent power transmission was obtained at resonance, indicating that energy was indeed being taken from the transmitted wave and being radiated as diffracted waves.

The bandwidth of the flat-strip samples perforated by ridge-loaded apertures is plotted in Fig. 41(b). The 3-db bandwidth is shown since this is a parameter commonly used to describe resonant structures. For a resonant perforated-metal sheet embedded within a radome, the bandwidth over which its presence would not affect the electrical performance of the radome would be significantly smaller than the 3-db bandwidth. The usable bandwidth of a radome containing a resonant-perforated metal sheet, would of course, depend on the type of radome, the dielectric constants of the materials used, and the polarization and range of incidence angles over which the radome is used, as well as on the metal sheet itself. The electrical performance of radomes containing resonant perforated-metal sheets has not been calculated or measured.



MEASURED RESONANCE FREQUENCY AND BANDWIDTH OF FLAT METAL STRIPS  
PERFORATED BY RIDGE-LOADED APERTURES

The parallel-plate transmission line cannot be used to measure the electrical performance of samples for the case of parallel-polarized waves incident on the sample at near-normal incidence. Thus, a flat metal sheet was perforated by a hexagonal array of ridge-loaded apertures, as shown in Fig. 42, and described under Column B of Table 8. The transmission of this flat-panel sample was measured as a function of frequency using the equipment set-up outlined in Fig. 38. The resonance frequency and bandwidth of the sample are shown in Fig. 43 as functions of incidence angle for the cases where the incident waves are polarized either perpendicular or parallel to the plane of incidence. The cut-off frequency,  $f_{c_0}$ , of a waveguide of the same cross section as the apertures was not measured, and there is not sufficient information in Fig. 37 that the effect of the

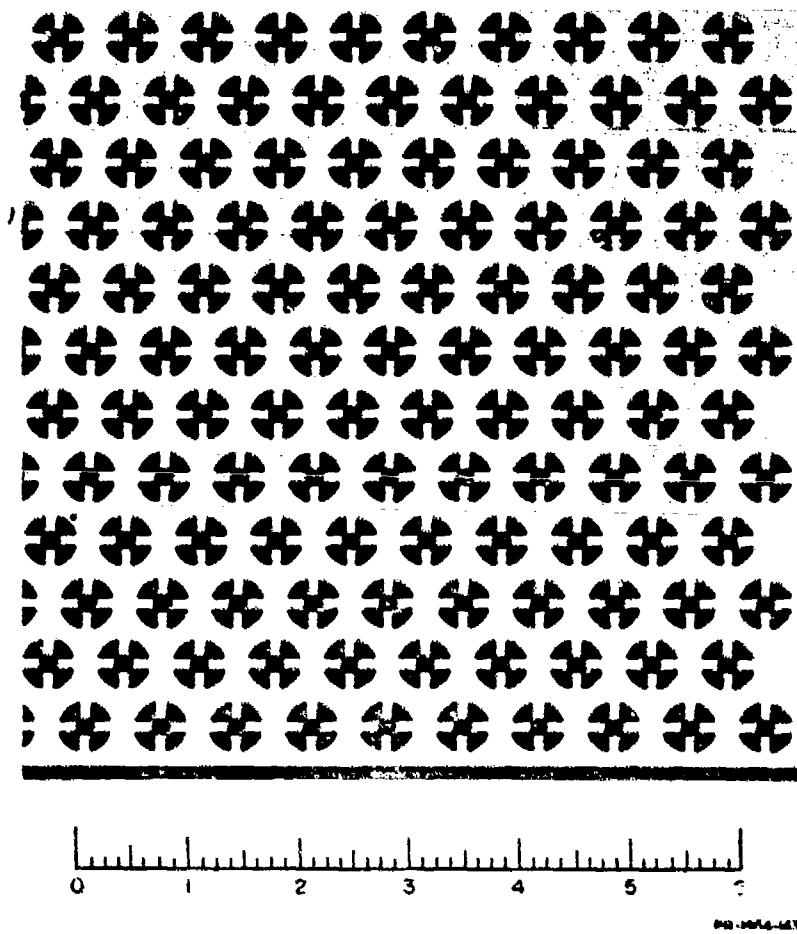
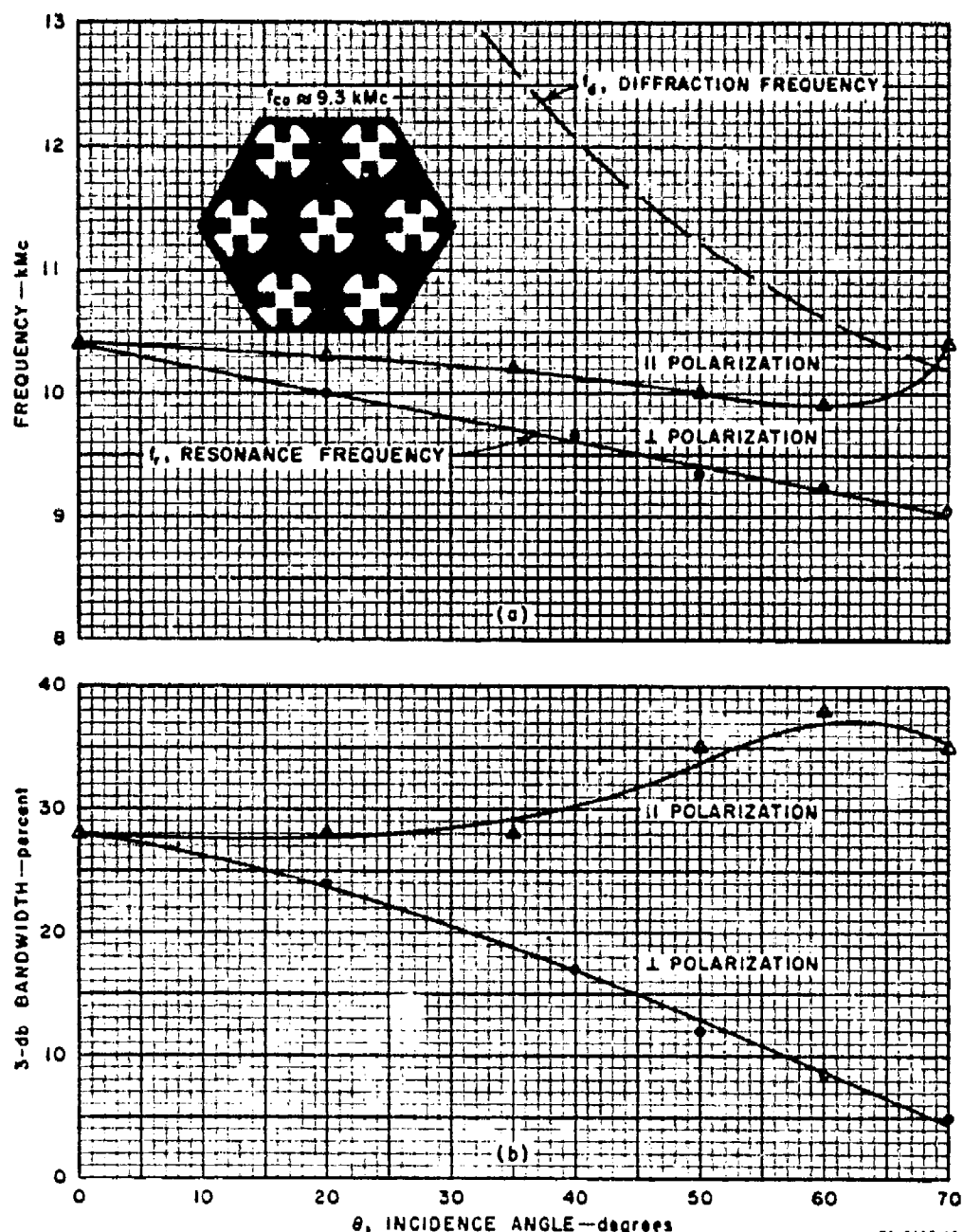


FIG. 42  
FLAT-PANEL SAMPLE OF A RESONANT PERFORATED METAL SHEET



fillets at the base of each ridge can be accounted for exactly. Using the upper curve of Fig. 37, however, and the curves of Fig. 35, one may estimate the cut-off frequency of the waveguide to be 9.3 kMc. Thus, the resonance frequency of the perforated metal sheet is within about 12 percent of  $f_{c_0}$ . The resonance frequency of this sample changes slightly with angle, even near normal incidence. The frequency variation is small enough compared to the bandwidth, however, that high transmission can be obtained over a usable range of incidence angles. The transmission for waves of both polarizations are plotted in Fig. 44 for a single frequency. From this figure it is seen that at least 93 percent power transmission can be obtained for either perpendicularly or parallel polarized waves incident at any angle out to  $\theta = 40$  degrees. The incidence angle within a radome for a wave passing through the radome cannot exceed 40 degrees for radome materials of relative dielectric constant greater than 2.4.

In addition to the desired resonance, at which all the incident energy is transmitted, a spurious resonance of the flat-panel sample was

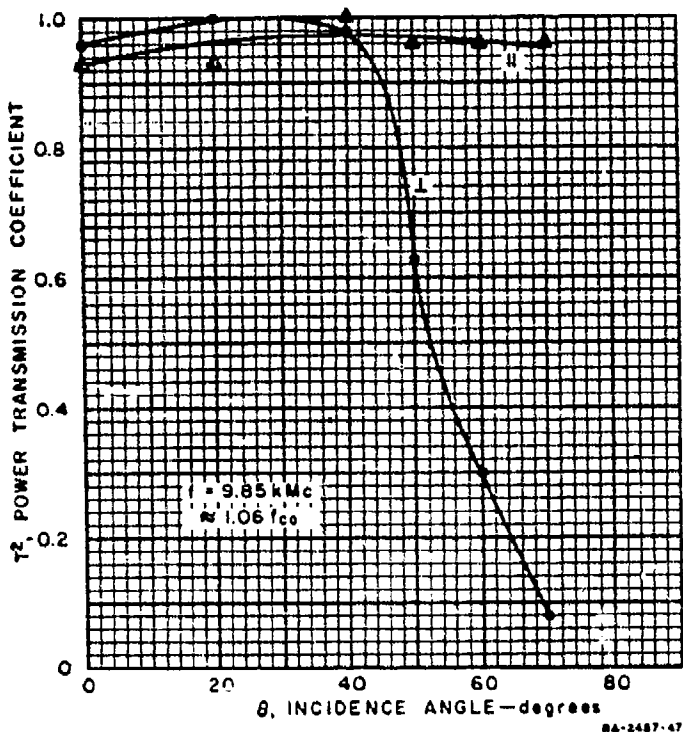


FIG. 44  
MEASURED TRANSMISSION VS. INCIDENCE ANGLE FOR THE  
FLAT-PANEL PERFORATED METAL SHEET

observed at which nearly all of the incident energy is reflected.\* The frequency of the spurious resonance is only a few percent above that of the desired resonance, and it is relatively narrow-band compared to the desired resonance. Thus, the spurious resonance appears as a deep notch in the frequency response of the sample. This notch is observed for oblique incidence for some orientations of the fields of the incident wave with respect to the plane of incidence and with respect to the pattern of apertures, but it is not observed for all orientations. Time did not permit the origin of the spurious resonance to be determined on this contract. The transmission properties of perforated metal sheets are also of interest with respect to an antenna application.<sup>15</sup> It is anticipated that the origin of the spurious resonance will be investigated further in the course of the antenna study. Presently available information indicates that perhaps the spurious resonance is due to a higher-order mode in the apertures. If this is the correct explanation, then the frequency of the spurious resonance could be moved away from that of the desired resonance by using different loading than was used with the flat-panel in Fig. 42. It might be possible to change the loading sufficiently by simply changing the length of the ridges, or it might be necessary to use an aperture shape with more than four ridges, such as shown in Fig. 33(c).

Returning to the consideration of the desired resonance of perforated metal sheets, it was stated previously that the resonance frequency was expected to be simply related to the cut-off frequency of a waveguide that has the same cross section as the apertures in the metal sheet. This was found to apply to some of the samples tested, but not to others. Thus, the cut-off frequency of the apertures must be only one of the factors that influences the resonance frequency of a perforated metal sheet. Another factor that might influence the resonance frequency is the energy stored in the nonpropagating modes corresponding to waves diffracted at imaginary angles. It is known, for instance, that these modes can influence the reactance of a parallel array of wires. The effect of these modes is taken into account by the correction term, consisting of an infinite summation, used in the theoretical formulas for the reactance of wire grids.<sup>16,17</sup> For a given wire spacing and incidence angle, the correction term is relatively unimportant until the frequency approaches that at which diffracted waves are radiated at real angles.

---

\* The space around the sample was explored with a horn and detector, and it was found that the energy was in specular reflected waves rather than in diffracted waves or in surface waves.

That these nonpropagating modes may also influence the resonance frequency of a perforated metal sheet is suggested by the curves of Fig. 45, where the data have been summarized for the various samples of perforated metal sheets.\* If the resonance frequency of each sample depended only on the cut-off frequency of its apertures, the curves in Fig. 45 would be horizontal lines. If, on the other hand, the resonance frequencies were constant fractions of the frequency  $f_s$ , at which diffraction occurs, the curves would be vertical lines. The curves shown in Fig. 45 indicate that the resonance frequency of a perforated metal sheet depends both on the cut-off frequency of its apertures, and on the frequency at which diffraction can occur. Also note that the slope of the curves for four of the six samples increases as the ratio  $f_r/f_s$  approaches unity. This indicates that the closer the condition for diffraction is approached, the more strongly the resonance frequency depends on the energy stored in the nonpropagating modes, and thus the more the resonance frequency changes with incidence angle. There is not any clear-cut criterion, however, that can be applied to all samples to determine how far  $f_r$  must be from  $f_s$  in order that the resonance frequency be independent of the incidence angle. The resonance frequency of a metal sheet perforated by circular apertures depends much more on the incidence angle than does that of a metal sheet perforated by ridge-loaded apertures. It is not evident why the electrical performance of a perforated metal sheet depends so much on the shape of the apertures.

It can be seen from the results of the limited number of measurements made on this program, that resonant perforated-metal sheets show promise as inclusions for radomes. It is also seen that care must be used in the choice of the dimensions and shape of the perforations. If these metal inclusions turn out to be mechanically promising also, further effort should be devoted to obtaining additional electrical design data.

#### RESONANT-WALL RADOMES WITH AIR-FILLED CAVITIES

Resonant-wall radomes, as were described in Sec. II, consist of a thick metal plate perforated by a number of resonant cavities. The condition for no diffraction from the radome determines the maximum center-to-center spacing between the cavities, which also places an upper bound

---

\* For the sake of clarity, not all the points for the various thicknesses of each type of sample have been shown. Also, points have been omitted for resonance frequencies such that diffraction can occur, since the energy in the diffracted waves changes from reactive stored energy to radiated energy for  $f_r > f_d$ .

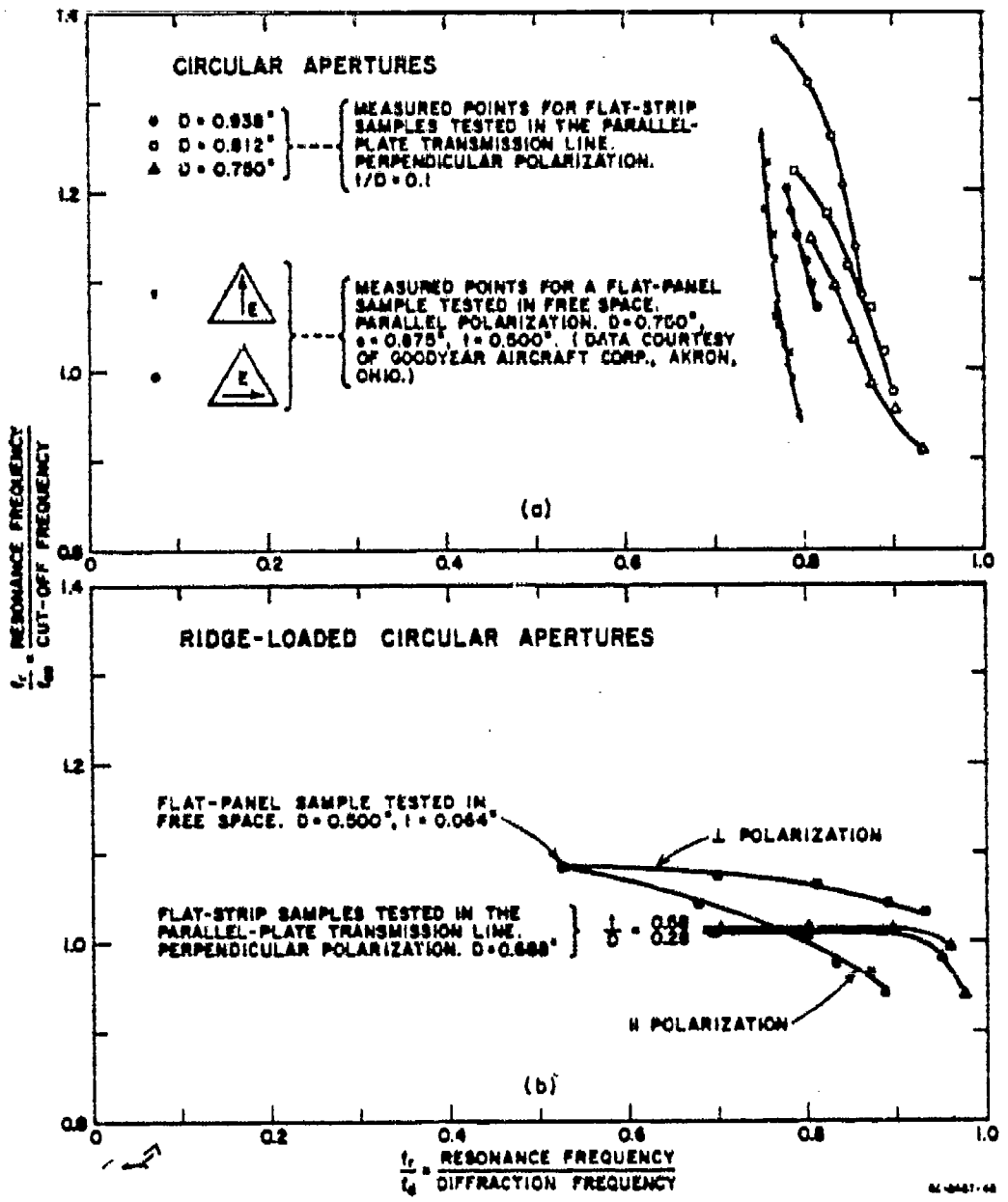


FIG. 45  
SUMMARY OF RESONANCE-FREQUENCY DATA FOR RESONANT  
PERFORATED-METAL SHEET SAMPLES

on the diameter of the cavities. Except for applications where the incidence angle is small, the cavity diameter turns out to be too small for energy to propagate through circular air-filled cavities. One way to lower the cut-off frequency so that energy can propagate through closely-spaced cavities is to fill the cavities with dielectric, as was shown in Fig. 1. For resonant-wall radomes such as in Fig. 1(a), the dielectric plugs also preserve the physical continuity of the radome surface. If the outer surface of the radome is covered by a layer of uniform dielectric, such as in Figs. 1(b), 1(c), and 1(d), the dielectric plugs are not necessary from a mechanical standpoint. In fact, use of the dielectric plugs presents mechanical problems with respect to the initial mounting of the plugs, and with respect to differential thermal expansion between the dielectric and the metal. The use of the dielectric plugs also presents electrical problems, such as excessive dissipation loss in the dielectric, and detuning of the cavities with variation of dielectric constant from plug to plug and variation of the dielectric constant with temperature.

Since the dielectric plugs in the cavities of resonant-wall radomes present several problems, it would be desirable to eliminate them when they are not required to complete the surface of the radome. It is now proposed that instead of using dielectric in the cavities, that ridge loading of the cavities be used to lower their cut-off frequency below the operating frequency of the radome. The ridges would take the form of metal strips running lengthwise through the cavities, so that the cavities would have cross sections similar to those shown in Fig. 33. This approach to the construction of resonant-wall radomes is suggested by the results for metal sheets perforated by ridge-loaded apertures, as reported in the preceding pages. Although the emphasis there was on relatively thin metal sheets, data were taken using flat-strip samples up to 0.400 inch thick. The transmission of these flat-strip samples was measured in the parallel-plate transmission line using perpendicularly polarized waves. As shown in Fig. 41 the resonance frequency was independent of incidence angle until the condition where diffraction could occur was approached. The bandwidth of the thickest sample is of the same order of magnitude as those of the resonant-wall radome samples Radomes A, B, and C, described in Sec. II. The concept of using air-filled, ridge-loaded cavities for dielectric-covered, resonant-wall radomes was originated too late to be developed further on the present contract. It is recommended that additional design data be obtained, and a radome panel built and tested in free space.

## SECTION IV

### CONCLUSIONS AND RECOMMENDATIONS

#### CONCLUSIONS OF THE STUDY

Of the metal-loaded radomes studied on this contract, as well as those studied on a previous contract,<sup>1</sup> the resonant-wall radomes appear most promising as high-strength radomes, since these radomes contain a relatively high percentage of metal. Thus, emphasis during the present program has been placed on investigating the electrical properties of resonant-wall radomes. The basic element in these resonant-wall radomes is a relatively thick metal plate perforated by resonant cavities. In general, it has been found that resonant-wall radomes can be designed to give high transmission over a wide range of incidence angles, but over a more restricted frequency bandwidth, and with slightly larger insertion-phase-delay variation as a function of incidence angle than is obtained with conventional half-wavelength and full-wavelength radomes. Other phases of this contract have shown that it is electrically feasible to embed wire grids within A-sandwich radomes with dielectric constants typical of ceramic skins and cores, and they indicate that it might be electrically feasible to embed self-resonant perforated metal sheets within A-sandwich radomes. An initial investigation indicates that it may be possible to use air-filled rather than dielectric-filled cavities in some resonant-wall radomes. More specific conclusions regarding metal-loaded radomes studied on this contract are given in the following paragraphs.

The empirical design data presented in this report can be used to design several configurations of resonant-wall radomes. The metal structure in each of these radomes consists of a thick metal plate perforated by a number of dielectric-filled circular waveguides, which form resonant cavities. For the configurations where a layer of dielectric is in contact with one surface of the metal plate, or where the metal plate is used by itself, the data cover a fairly large range of metal plate and surface dielectric thicknesses. The data can also be used to design resonant-wall radomes with a layer of dielectric in contact with each surface of the metal plate, for which case only a very limited range of dielectric

## SECTION IV

### CONCLUSIONS AND RECOMMENDATIONS

#### CONCLUSIONS OF THE STUDY

Of the metal-loaded radomes studied on this contract, as well as those studied on a previous contract,<sup>1</sup> the resonant-wall radomes appear most promising as high-strength radomes, since these radomes contain a relatively high percentage of metal. Thus, emphasis during the present program has been placed on investigating the electrical properties of resonant-wall radomes. The basic element in these resonant-wall radomes is a relatively thick metal plate perforated by resonant cavities. In general, it has been found that resonant-wall radomes can be designed to give high transmission over a wide range of incidence angles, but over a more restricted frequency bandwidth, and with slightly larger insertion-phase-delay variation as a function of incidence angle than is obtained with conventional half-wavelength and full-wavelength radomes. Other phases of this contract have shown that it is electrically feasible to embed wire grids within A-sandwich radomes with dielectric constants typical of ceramic skins and cores, and they indicate that it might be electrically feasible to embed self-resonant perforated metal sheets within A-sandwich radomes. An initial investigation indicates that it may be possible to use air-filled rather than dielectric-filled cavities in some resonant-wall radomes. More specific conclusions regarding metal-loaded radomes studied on this contract are given in the following paragraphs.

The empirical design data presented in this report can be used to design several configurations of resonant-wall radomes. The metal structure in each of these radomes consists of a thick metal plate perforated by a number of dielectric-filled circular waveguides, which form resonant cavities. For the configurations where a layer of dielectric is in contact with one surface of the metal plate, or where the metal plate is used by itself, the data cover a fairly large range of metal plate and surface dielectric thicknesses. The data can also be used to design resonant-wall radomes with a layer of dielectric in contact with each surface of the metal plate, for which case only a very limited range of dielectric

thickness is covered. (It has been suggested that a layer of uniform dielectric might be required on the outer surface of the radome to prevent rain erosion at the dielectric-to-metal joints in the perforated metal plate.) The data can, of course, also be used to design radomes consisting of any of the resonant-wall radome configurations mentioned covered by a conventional half-wavelength radome spaced from the resonant-wall radome.

For values of cavity diameter sufficiently large that the  $TE_{11}$  circular-waveguide mode can propagate through the cavities, the bandwidth of a resonant-wall radome increases as the cavity diameter is increased. For resonant-wall radomes of a given thickness without dielectric in contact with either surface, wider bandwidth is obtained by operating the radome at the second-order resonance than at the first-order resonance. (The first-order and second-order resonances are defined as those at which the cavities are approximately  $0.5 \lambda_{gj}$  and  $\lambda_{gj}$  in length, respectively. These resonances are analogous to those of the conventional half-wavelength and full-wavelength radomes. Here  $\lambda_{gj}$  is the guide wavelength in a circular waveguide of the same diameter and filled with the same dielectric as the cavities.) It is expected that the bandwidth of a resonant-wall radome will always be less than that of a conventional uniform-dielectric radome of the same physical thickness, and constructed of the same dielectric as the resonant-wall radome. (For example, the 3-db bandwidth of a particular resonant-wall radome operated at its first-order resonance, Radome A, was smaller than that of a comparable half-wavelength radome by a factor of 0.17. The 3-db bandwidth of a particular resonant-wall radome, Radome B, was smaller than that of a comparable full-wavelength radome by a factor of 0.47.) Resonant-wall radomes are intrinsically narrow-bandwidth devices when they are used with perpendicularly polarized waves incident on the radome at wide angles.

It is possible to represent the perforated metal plate of resonant-wall radomes as being equivalent to a length of transmission line terminated at each end by a reactive discontinuity plus the equivalent conductance of the medium at each surface of the metal plate. (Dielectric layers in the radomes are of course, also equivalent to lengths of transmission line.) Formulas for the parameters of this equivalent circuit have not been rigorously derived. These parameters can, however, be calculated approximately from formulas in the open literature that were derived for structures having some physical resemblance to various regions of the resonant-wall radome. Using the approximate circuit values for two resonant-wall radomes without surface dielectric, Radomes A and B, the calculated

electrical performance satisfactorily predicted the radome bandwidth, the effect of dissipation loss, and the change in resonance frequency as the incidence angle and polarization change. The resonance frequencies are also predicted with only a small error, the error in resonance frequencies for Radomes A and B being only 0.4 percent and 1.3 percent, respectively. The calculated resonance frequency of a resonant-wall radome with dielectric in contact with one surface, Radome C, agreed with the measured value within 1.8 percent. Even these small discrepancies can be eliminated by properly locating the reference planes at which the terminals of the equivalent circuit are taken. A general formula for determining the reference plane locations has not, however, been developed.

Resonant-wall radomes give high transmission over a fairly wide range of incidence angles over a limited frequency range, as demonstrated by both the calculated and measured data presented in this report. At its first-order resonance, a sample without surface dielectric, Radome A, gives at least 70 percent power transmission out to an incidence angle of 74 degrees for waves polarized either perpendicular or parallel to the plane of incidence. When the maximum incidence angle is limited to 60 degrees, the power transmission is at least 70 percent for waves of either polarization over a 2.2-percent frequency bandwidth. When operated at its second-order resonance, this radome sample is designated as Radome B, and gives at least 80-percent power transmission out to an incidence angle of 80 degrees for waves of either polarization. The bandwidth for 70 percent power transmission of waves of either polarization is 2.1-percent or 3.3-percent when the maximum incidence angle is limited to 70 degrees or 60 degrees, respectively. The calculated power transmission of a resonant-wall radome with dielectric in contact with one surface, Radome C, is at least 70 percent out to an incidence angle of 70 degrees for waves of either polarization. The calculated bandwidth for 70 percent power transmission of waves of either polarization is 1.7 percent when the maximum incidence angle is limited to 60 degrees.

It appears that curved resonant-wall radomes would have slightly higher boresight error than uniform-dielectric radomes of the same physical thickness. This conclusion is based on a comparison of the insertion-phase-delay characteristics of the various radomes as the incidence angle changes. Since the insertion phase delay depends on the thickness of a radome, as well as on the type of radome, the radomes were not compared directly. Rather, the variation in insertion phase delay of each radome was compared with the variation in electrical thickness of a layer of air of the same

physical thickness as the respective radome. (See the footnote at the bottom of p. 25.)

A brief study of the transmission properties of ceramic A-sandwich radomes has shown that it is electrically feasible to embed wire grids within these radomes. These metal-loaded A-sandwich radomes have the electrical advantages over conventional, unloaded A-sandwich radomes that they give high transmission out to wider incidence angles, and the tolerance required on core thickness is less stringent. These results are the same as reported in Ref. 1 for metal-loaded A-sandwich radomes using lower-dielectric-constant materials. For the present study, the wire grids were located at the skin-to-core interfaces, but it seems likely that it would also be electrically feasible to locate the grids within the skins or within the core. There is a limit to the reactive discontinuity that can be introduced by the wire grids if high transmission over a wide range of incidence angles is required. Thus, there is a limit on the amount of metal that can be included in the radome. It might be possible to substitute inductive perforated metal sheets for the wire grids in some designs. The electrical performance of A-sandwich radomes containing perforated metal sheets cannot be calculated, however, since the equivalent circuit of a perforated metal sheet located at or near a discontinuity in dielectric constant is not known.

A self-resonant perforated-metal sheet also appears promising for inclusion within A-sandwich radomes. The apertures in this metal structure are resonant, analogous to the resonant coupling apertures used in wave-guide structures such as TR tubes, and thus all the incident energy is transmitted through the metal sheet. The data quoted in this report show that it is possible to obtain high transmission through a resonant perforated-metal sheet over the range of incidence angles likely to be encountered within the core of a ceramic A-sandwich radome. The electrical performance of a radome containing this type of metal inclusion has not been determined to date.

For resonant-wall radome configurations where the metal plate is covered by a layer of dielectric, it appears possible to eliminate the dielectric from the resonant cavities in the metal plate. When the perforated metal plate is covered with dielectric, the dielectric plugs in the resonant cavities are not required to maintain the physical continuity of the radome surface. They do serve the electrical function, however, of lowering the cut-off frequency of the cavities in the metal plate below

the operating frequency of the radome. Another commonly used technique for lowering the cut-off frequency of a waveguide is to ridge-load the waveguide. The data available to date indicate that it may be possible to use ridge-loading rather than dielectric-loading in the cavities of some resonant-wall radomes. This concept requires further development.

#### RECOMMENDATIONS FOR FUTURE WORK

The investigations described here have been primarily concerned with radomes that contain thick metal inclusions and that have good electrical performance over a range of incidence angles from 0 to 85 degrees for waves polarized either perpendicular or parallel to the plane of incidence. There are a number of applications, however, where radomes operate over a more restricted range of angles, or for only one polarization. Metal-loaded radomes should be investigated for these applications also.

Most of the effort on the present program was devoted to an experimental investigation of the electrical properties of resonant-wall radomes. To thoroughly explore the properties of a radome with as many independent parameters as the various resonant-wall radome configurations have would take a much larger experimental program than was possible on the present contract. Late in the contract, some fairly accurate equivalent circuits were developed for resonant-wall radomes. Calculations based on these equivalent circuits could be carried out using an electronic digital computer to investigate a wide range of design parameters. Additional information about the properties of resonant-wall radomes could be obtained this way with much less effort than by an extensive experimental program.

The limited amount of data available to date indicates that thin metal sheets perforated by ridge-loaded circular apertures appear electrically promising for inclusion within A-sandwich radomes. Also, thick metal plates perforated by the same aperture shape appear promising as the metal element in resonant-wall radomes that are covered with a layer of dielectric. Both of these topics should be investigated further.

APPENDIX A

**PARALLEL-PLATE TRANSMISSION-LINE SET-UP FOR MEASURING THE  
ELECTRICAL PERFORMANCE OF FLAT-STRIP RADOME SAMPLES**

**DESCRIPTION OF EQUIPMENT**

Equipment for measuring the power transmission coefficient and insertion phase delay of flat-strip radome samples, such as shown in Fig. 12, at any frequency between 8.2 and 12.4 kilomegacycles is shown in Figs. 46 and 47. This equipment is a microwave bridge circuit in which

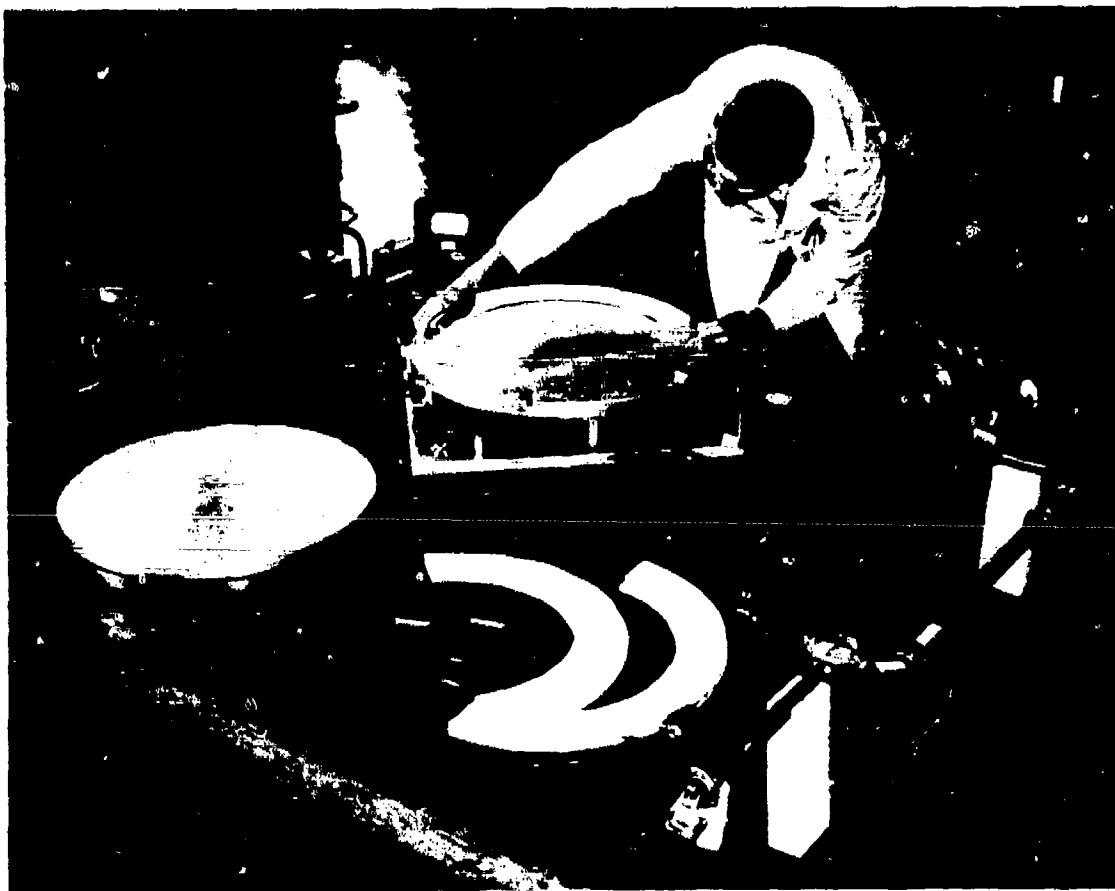
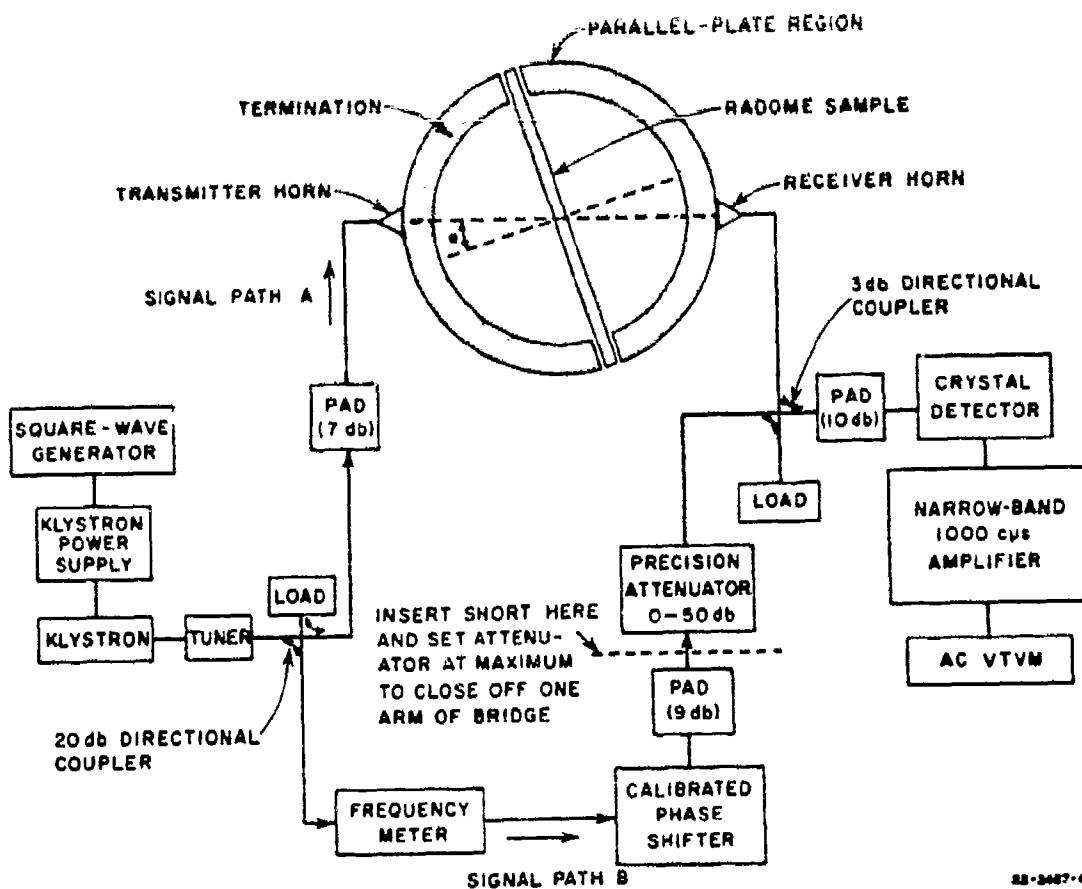


FIG. 46  
PARALLEL-PLATE TRANSMISSION-LINE SET-UP



22-3487-44

FIG. 47  
BLOCK DIAGRAM OF THE PARALLEL-PLATE TRANSMISSION-LINE SET-UP

the amplitude and phase of a signal passing through the radome sample are compared with the amplitude and phase of a reference signal. The bridge is balanced with and without the sample present using a precision attenuator and phase shifter. The differences in the readings give the insertion loss and insertion phase delay of the sample. The equipment set-up and measurement procedures are essentially the same as more familiar free-space measurement set-ups, except that the free-space region is replaced by the parallel-plate transmission line described in Table 9.

The parallel-plate transmission line consists of two plane conducting plates between which energy is transmitted by a horn at the edge of the plates. A portion of this energy is received by a second horn diametrically across the conducting plates from the transmitting horn. A flat-strip radome sample inserted in the transmission line is mirrored in the

TABLE 9  
DIMENSIONS OF PARALLEL-PLATE TRANSMISSION-LINE SET-UP

Diameter of conducting plates	24 inches
Material used to construct conducting plates	Aluminum tool and jig plate
Spacing between conducting plates, $a$	0.900 inch
Uniformity of conducting-plate spacing	
Over entire surfaces	$\pm 0.002$ inch
At location of radome samples	$\pm 0.0005$ inch
Inside height of horns	0.90 inch
Inside width of horns, $w$	2.40 inches
Operating frequency range	8.2 to 12.4 kMc
Far-field region of horns, $2w^2/\lambda$	8.0 to 12.1 inches

conducting plates so that it is equivalent to a flat-panel radome sample of infinite height. The edges of the conducting plates were made in a circular shape so that the angle at which energy is incident on the radome samples can be varied by rotating the conducting plates about their centers. Waves may be excited between the conducting plates with the electric field either vertical, i.e., perpendicular to the ground planes, or with the electric field horizontal. The equivalence between these waves and waves in free space will be discussed following the description of the equipment.

The parallel-plate transmission-line set-up was constructed because it combines most of the advantages of free-space set-ups and waveguide set-ups yet retains few of the disadvantages of each. Waveguide set-ups have the advantages that very small samples can be used and accurate data can be obtained, but they have the disadvantages that the incidence angle cannot be varied continuously at a fixed frequency, and it is not convenient to vary the polarization of the incident waves. Free-space set-ups have the advantage that the incidence angle and polarization of the incident waves can be readily varied, but they have the disadvantages that rather large radome samples are required, and inaccuracies are introduced by stray reflections around the set-up and by diffraction from the edges of the sample.

The width of the samples used in the parallel-plate transmission line is comparable to that required for free-space samples, but the height is significantly smaller. A termination is placed around the perimeter of the conducting planes to prevent energy from reaching the receiving horn by reflections from objects near the set-up, and to prevent diffraction

from the ends of the sample. These terminations also eliminate standing waves between the sample and the two horns since the horns are outside the terminations. Thus, these sources of error are minimized without displacing the sample with respect to the horns, as is commonly done with free-space set-ups.\*

Terminations used for vertically polarized waves are different than those used for horizontally polarized waves. Both are shown in Fig. 46. Each termination consists of appropriate lossy elements supported parallel to the electric fields by rings of Styrofoam. Gaps are provided in these rings through which the radome samples can be inserted. The lossy elements used with vertically polarized waves are wedges of resistance paper  $3\frac{1}{2}$  inches long and tapered from a point at the inside of the termination to 0.9 inch in height at the outside. There are 230 of these wedges spaced less than a half-wavelength apart so that diffraction will not occur from the array of wedges. Alternate wedges were made of 2400-ohm-per-square and 1200-ohm-per-square material to give an attenuation of about 10 db for waves passing through the termination once. The lossy element used with horizontally polarized waves consists of a ring of 1200-ohm-per-square resistance paper  $2\frac{1}{4}$  inches wide with 0.75-inch-deep serrations on the inner edge. This termination also has an attenuation of about 10 db over the frequency band. If the magnitude of the amplitude reflection coefficient for waves incident on the edges of the parallel-plate transmission line is of the same order as that for an open-ended rectangular waveguide (\* e., about 0.2), 10 db of attenuation would give an input VSWR of the terminations of 1.05. The actual VSWR's of the terminations have not been determined, but they seem to be satisfactory.

## EQUIVALENCE TO FREE SPACE

### VERTICAL POLARIZATION

For this polarization, the dominant mode that can propagate in the parallel-plate transmission line is the TEM mode, which is independent of the spacing between the conducting plates. Because of the symmetry of the horns, only the dominant mode will be set up. The electric field is perpendicular to the conducting plates, which are in turn parallel to the plane of incidence. Thus, vertically polarized waves incident on a radome

\* It might be possible to use a similar termination to improve the accuracy of and facilitate free-space measurements, but this is not common practice. Such a termination might be in the form of a spherical shell of variable-density rubberized horsehair or tapered wedges of absorbing material.

sample mounted in the parallel-plate transmission line are exactly equivalent to perpendicularly polarized waves incident on a radome sample in free space. The incidence angle for this case is the angle between the normal to the radome surface and the line between the two horns. A scale is provided on the top plate for reading this angle opposite an index mark on one of the horns.

#### HORIZONTAL POLARIZATION

For this polarization, the dominant mode that can propagate in the parallel-plate transmission line is a TE mode equivalent to the  $TE_{10}$  mode in a rectangular waveguide of infinite height whose side walls correspond to the conducting plates of the parallel-plate line. This TE mode can be resolved into two TEM waves whose directions of propagation make angles  $\beta$  and  $-\beta$  with the line joining the centers of the two horns, as was explained in Appendix B of Ref. 1. The angle  $\beta$  is given by Eq. (42).

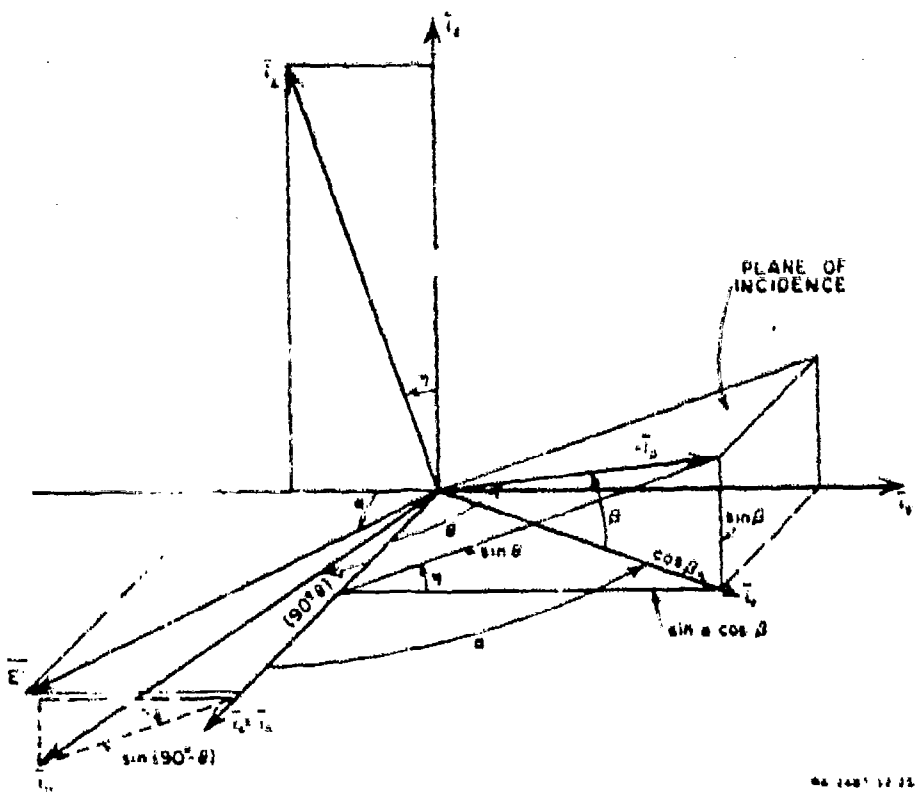
$$\beta = \sin^{-1} \left( \frac{\lambda}{2a} \right) . \quad (42)$$

As a simplification, one of these TEM waves will be considered as the incident wave in the following discussion.

The plane of incidence is defined by the unit vector  $\bar{i}_n$ , which is normal to the surface of the radome sample, and the unit vector  $\bar{i}_p$ , which is in the direction of propagation of one of the above mentioned TEM waves, as indicated in Fig. 48. In Fig. 48, the xy-plane is parallel to the ground planes, and the yz-plane is taken as the face of the radome sample, therefore  $\bar{i}_n = \bar{i}_z$ , and the electric vector  $\bar{E}'$  of the incident wave lies in the xy-plane. The angle measured from  $\bar{i}_n$  to  $\bar{i}_p$  is defined as  $\alpha$ , where  $\bar{i}_p$  is a unit vector in the direction of a reference line from the center of the receiving horn to the center of the transmitting horn. The angle  $\beta$  given by Eq. (42) is measured from  $\bar{i}_p$  to  $-\bar{i}_p$  in Fig. 48. The angle of incidence,  $\theta$ , is measured from  $\bar{i}_n$  to  $-\bar{i}_p$ , and is given by Eq. (43):

$$\cos \theta = \cos \alpha \cos \beta . \quad (43)$$

When the angle  $\alpha$  is zero, the plane of incidence lies in the  $xz$ -plane, thus the incidence angle is  $\beta$ , and the incident wave is polarized perpendicular to the plane of incidence. For  $\alpha$  different from zero, the plane



66-1487-17-22

FIG. 48  
COORDINATE SYSTEM FOR HORIZONTALLY POLARIZED WAVES IN THE  
PARALLEL-PLATE TRANSMISSION-LINE

of incidence is inclined from the  $xy$ -plane and thus the incident wave can be resolved into a component  $E_{\parallel}$  polarized parallel to the plane of incidence, and a component  $E_{\perp}$  polarized perpendicular to the plane of incidence. The electric vector,  $\bar{E}'$ , of the incident wave can be written in terms of these components and in terms of its  $x$ - and  $y$ -components as in Eq. 44:

$$\bar{E}' = \bar{i}_1 E_{\perp} + \bar{i}_{\parallel} E_{\parallel} = \bar{i}_y E' \sin \alpha - \bar{i}_x E' \cos \alpha \quad (44)$$

where

$E'$  = the amplitude of the incident wave

$\bar{i}_1$  = a unit vector perpendicular to the plane of incidence

$\bar{i}_{\parallel}$  = a unit vector parallel to the plane of incidence and perpendicular to  $i_p$

The unit vectors  $\bar{t}_x$  and  $\bar{t}_y$  are given in terms of their x-, y-, and z-components by Eqs. (45) and (46).

$$\bar{t}_x = \bar{i}_x \sin \eta + \bar{i}_y \cos \eta = \bar{i}_x \frac{\sin \beta}{\sin \theta} + \bar{i}_y \frac{\tan \alpha}{\tan \theta} \quad (45)$$

$$\bar{t}_y = \bar{i}_x \cos (90^\circ - \theta) = \bar{i}_x \sin (90^\circ - \theta) \cos \eta$$

$$= \bar{i}_x \sin (90^\circ - \theta) \sin \eta$$

$$= \bar{i}_x \sin \theta + \bar{i}_y \frac{\sin \alpha \cos \beta}{\tan \theta} = \bar{i}_x \frac{\sin \beta}{\tan \theta} \quad (46)$$

The perpendicularly and parallel polarized components of the incident wave are found using the following scalar products:

$$E_x^i = \bar{t}_x \cdot \bar{E}^i = E^i \frac{\cos \alpha \sin \beta}{\sin \theta} \quad (47)$$

$$E_y^i = \bar{t}_y \cdot \bar{E}^i = E^i \frac{\sin \alpha}{\sin \theta} \quad (48)$$

The perpendicularly and parallel polarized components of the wave at the output plane of the radome are

$$E_x^o = E_x^i T_x e^{-j\psi_x} = E^i \frac{\cos \alpha \sin \beta}{\sin \theta} T_x e^{-j\psi_x} \quad (49)$$

$$E_y^o = E_y^i T_y e^{-j\psi_y} = E^i \frac{\sin \alpha}{\sin \theta} T_y e^{-j\psi_y} \quad (50)$$

where

$T_x, T_y$  = magnitude of the amplitude transmission coefficient for perpendicularly and parallel polarized waves, respectively

$\psi_x, \psi_y$  = phase delay of the amplitude transmission coefficient for perpendicularly and parallel polarized waves, respectively

The resultant output electric vector,  $\bar{E}^o$ , is not, in general horizontal due to differences in magnitude and phase of the transmission coefficients

for the perpendicular and parallel polarized components. The receiving horn, however, measures only the horizontally polarized component,  $E_H^*$ , of the output wave, which is related to the input wave by

$$E_H^* = E^* T_A e^{-j\psi_A} = \bar{t}_A \cdot E^* = \bar{t}_A \cdot (T_{\perp} E_{\perp}^* + T_H E_H^*) \quad (51)$$

where

$T_A$  = the magnitude of the amplitude transmission coefficient measured with horizontally polarized waves in the parallel-plate transmission line

$\psi_A$  = the phase delay of the amplitude transmission coefficient measured with horizontally polarized waves

$\bar{t}_A = \bar{t}_y \sin \alpha - \bar{t}_x \cos \alpha$  = a unit vector parallel to the xy-plane and perpendicular to  $\bar{t}_y$ .

Combining Eqs. (49), (50), and (51) gives

$$T_A e^{-j\psi_A} = \left( \frac{\cos \alpha \sin \beta}{\sin \theta} \right)^2 T_{\perp} e^{-j\psi_{\perp}} + \left( \frac{\sin \alpha}{\sin \theta} \right)^2 T_H e^{-j\psi_H} \quad (52)$$

Multiplying both sides of Eq. (52) by  $\exp [j(2\pi L/\lambda) \cos \theta]$  and solving for  $T_H \exp (-j\psi_H)$  gives Eq. (53):

$$T_H e^{-j\psi_H} = \left( \frac{\sin \theta}{\sin \alpha} \right)^2 T_A e^{-j\psi_A} - \left( \frac{\sin \beta}{\tan \alpha} \right)^2 T_{\perp} e^{-j\psi_{\perp}} \quad (53)$$

where  $\psi_H$ ,  $\psi_A$ , and  $\psi_{\perp}$  are the insertion phase delays of the radome sample for incident waves of the respective polarizations. Using the parallel-plate transmission-line set-up,  $T_A$  and  $\psi_A$  are measured as functions of incidence angle using horizontally polarized waves, and  $T_{\perp}$  and  $\psi_{\perp}$  are measured as functions of incidence angle using vertically polarized waves. From these data the transmission coefficient and insertion phase delay for waves polarized parallel to the plane of incidence can be calculated at various incidence angles using Eq. (53).\*

---

\* The above derivation holds only for isotropic radome surfaces. It is assumed that the space between the cavities in the resonant-wall radome is sufficiently small in terms of free-space wavelengths that the radome surfaces appear isotropic.

## ACCURACY AND LIMITATIONS

The accuracy of the data obtained with the parallel-plate transmission-line set-up is limited by the accuracy of the precision attenuator and phase shifter used in the bridge, the frequency stability of the signal source, and the residual mismatches between components of the set-up.

The precision attenuator used to balance the bridge has a rated accuracy within plus or minus two percent of the reading in decibels, thus, between two readings on the dial there might be an error of four percent. For radome samples with power transmission coefficient greater than  $T^2 = 0.5$ , this error would amount to less than 0.12 db, or three percent error in  $T^2$ . The attenuation of the precision phase shifter has a rated variation of less than 0.3 db at frequencies from 8.2 to 10 kMc, and less than 0.4 at frequencies 10 to 12.4 kMc. Thus the maximum expected error in insertion loss due to errors in the attenuator and phase shifter is plus or minus 0.52 db. The consistency of the data suggests that the error is significantly smaller than this maximum value.

The precision phase shifter used to balance the bridge has a rated maximum error of 2.0 degrees at frequencies from 8.2 to 10 kMc, and 3.0 degrees from 10 to 12.4 kMc. The phase shift of the precision attenuator has a rated variation of less than 1.0 degree over the attenuation range used. Thus the maximum expected error in insertion phase delay due to errors in the attenuator and phase shifter is plus or minus 4.0 degrees.

The signal source used with the bridge circuit is a Varian Associates X-13 klystron oscillator stabilized against rapid temperature variations by being immersed in an oil bath. This klystron provides sufficient power that the null at balance of the bridge is not obscured by the noise of the receiver circuits.\* As a result, reference readings could be repeated at the end of most experiments within an accuracy of plus or minus 0.05 db and 0.5 degrees.

Errors due to mismatch between components in the set-up were reduced by placing a termination around the edges of the parallel-plate transmission line, by placing fixed pads between the horns and the other wave-guide components, and by having the precision attenuator and phase shifter

\* The set-up can also be used to measure insertion loss directly by blocking off signal path B of the bridge and noting the level of the received signal before and after the sample is inserted. For this type of measurement, a microwave signal generator such as that shown in Fig. 46 provides sufficient power.

work with matched source and load impedances. The smoothness of the measured curves suggests that errors due to mismatch are small.

When horizontally polarized waves are used, the incidence angle approaches a minimum value of  $\beta$  as the angle  $\alpha$  approaches zero, as shown by Eq. (43). Furthermore, Eq. (48) shows that as  $\alpha$  goes to zero the parallel-polarized component goes to zero. Thus it is not possible to obtain data for horizontally polarized waves incident at angles smaller than  $\beta$ . The accuracy of the calculated transmission coefficient and insertion phase delay for waves polarized parallel to the plane of incidence is poor for incidence angles near the minimum value, since Eq. (53) then involves the difference between quantities of nearly the same amplitude and phase.

Consideration should also be given to the fact that resonant-wall radome samples such as that shown in Fig. 12 have some cavities that are semicircular rather than circular in cross section. If a circular waveguide supporting the  $TE_{11}$  mode is bisected by a plane conducting surface that is perpendicular to the electric field, the fields in the waveguide are not affected. On the other hand, if the plane conducting surface is parallel to the electric field, the  $TE_{11}$  mode will be cut off. It is seen by analogy that the semicircular cavities will propagate energy when the waves incident on the radome sample are vertically polarized, but that they will not propagate energy when the incident waves are horizontally polarized. This does not significantly affect the measured electrical performance, however, since the power flow for horizontally polarized waves goes to zero at the conducting plates forming the parallel-plate transmission line. Thus, very little energy would be transferred through the semicircular cavities even if they were not below cut-off, as can be verified by referring to the curves for perpendicularly polarized waves in Figs. 13 and 16. For each of these curves there is one point for which the incidence angle is not a multiple of five degrees. These points were obtained using horizontally polarized waves with  $\alpha = 0$ , and it is seen that they are in good agreement with the other points, which were obtained using vertically polarized waves.

Good fit between the radome sample and the conducting plates of the parallel-plate transmission line is also important. In order to obtain proper mirror-imaging of metal inclusions embedded in the radome, it is necessary for current to flow between most metal inclusions and the conducting plates. For the resonant-wall radomes discussed in this report,

no difficulty was encountered in obtaining satisfactory fit of the samples. The height of the samples was readily held to sufficiently close tolerances that contact between the conducting plates and the samples was obtained at closely spaced points, except as noted for the resonant-wall radome sample designated as Radome C. Any gap between the sample and the conducting plates is a waveguide below cut-off when horizontally polarized waves are incident on the samples tested, thus energy will not propagate through the gap. For vertically polarized waves, however, a gap will be a low-impedance transmission line, through which significant energy may propagate at resonances of this length of transmission line. Erratic behavior of the radome performance was observed due to such resonances, but it was usually possible to damp out these resonances by placing a lossy dielectric in the gaps. The particular lossy dielectric used was Liqui-moly NV grease, a suspension of molybdenum particles in a grease-like glycol vehicle. The dielectric constant and loss tangent of this material was measured by the thin-sample technique described in Ref. 18, and found to be  $\epsilon = 2.9$ , and  $\tan \delta = 0.13$ . Uncertainty as to the exact thickness of the sample could contribute plus or minus 30 percent error to these figures.

## APPENDIX B

### CHARACTERISTIC ADMITTANCE OF RESONANT-WALL RADOMES

A variational solution is given by Marcuvitz<sup>4</sup> for the problem of a rectangular waveguide terminated by a circular waveguide as shown in Fig. 49(a). The manner in which this solution can be used to calculate the characteristic admittance of resonant-wall radomes will be described in this appendix. The exact analogy that exists between the dominant  $TE_{10}$  mode in rectangular waveguide and perpendicularly polarized TEM waves in free space has been pointed out in Appendix B of Ref. 1, as well as in many microwave textbooks. Thus, some similarity between the problem considered by Marcuvitz and the resonant-wall radome is immediately apparent. The greatest differences are that for the problem solved by Marcuvitz, the circular waveguide is not filled with dielectric, and its diameter is small enough that it is below cut-off for all modes.

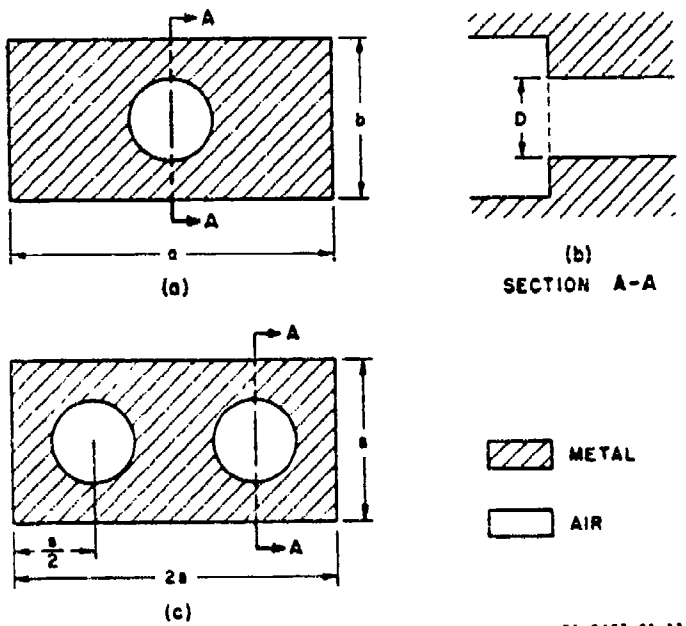


FIG. 49  
RECTANGULAR WAVEGUIDES TERMINATED BY  
CIRCULAR WAVEGUIDES

The formula given in Ref. 4 for the characteristic admittance,  $Y_0'$ , of the single circular waveguide below cut-off terminating a rectangular waveguide is

$$\frac{Y_0'}{Y_0} = -j \frac{0.446 ab\lambda_s}{D^3} \sqrt{1 - \left(\frac{1.706 D}{\lambda}\right)^2} \left[ \frac{1 - \left(0.853 \frac{D}{a}\right)}{2J'_1 \left(\frac{\pi D}{2a}\right)} \right]^2 \quad (54)$$

where

$Y_0$  = the characteristic admittance of the rectangular waveguide

$\lambda_s$  = the guide wavelength in the rectangular waveguide

$\lambda$  = free-space wavelength

$J'_1$  = the first derivative of the Bessel function of the first kind of the first order.

The dimensions  $a$ ,  $b$ , and  $D$  are defined on Fig. 49. If two circular waveguides below cut-off are used to terminate a rectangular waveguide, as in Fig. 49(c), Eq. (54) still applies, since each of these circular waveguides couples less strongly to the rectangular waveguide than does the circular waveguide in Fig. 49(a). The unnormalized admittance of the circular waveguides can be obtained, recalling that in the rectangular guide

$$\lambda_s = \frac{\lambda}{\cos \theta} \quad (55)$$

and taking the definition of  $Y_0$  as

$$Y_0 = \frac{\cos \theta}{377} \quad (56)$$

The incidence angle for the two TEM components of the  $TE_{10}$  rectangular-waveguide mode is found from Eq. (57):

$$\theta = \sin^{-1} \left( \frac{\lambda}{2a} \right) \quad (57)$$

Combining Eqs. (54), (55), and (56), Eq. (58) results:

$$Y_0 = -j \frac{0.892}{377} \left( \frac{s}{D} \right)^2 \frac{\lambda}{D} \sqrt{1 - \left( \frac{1.706 D}{\lambda} \right)^2} \left[ \frac{1 - \left( 0.426 \frac{D}{s} \right)^2}{2J_1' \left( \frac{\pi D}{4s} \right)} \right]^2 \quad (58)$$

Equation (58) is written for the case of a rectangular waveguide of height  $s$  and width  $2s$ . For this special case, the images of the two circular waveguides formed in the walls of the rectangular waveguide lie in a square array with center-to-center spacing  $s$ .

For circular waveguides filled with dielectric of relative dielectric constant  $\epsilon_3$ , the  $\lambda$  in the radical of Eq. (58) is replaced by  $\lambda_3 = \lambda/\sqrt{\epsilon_3}$ . Equation (58) can then be simplified by carrying out the following algebraic manipulations:

$$\begin{aligned} -j \frac{\lambda}{D} \sqrt{1 - \left( \frac{1.706 D}{\lambda_3} \right)^2} &= \left( 1.706 \sqrt{\epsilon_3} \right) \frac{\lambda}{1.706 D \sqrt{\epsilon_3}} \sqrt{\left( \frac{1.706 D}{\lambda_3} \right)^2 - 1} \\ &\approx 1.706 \sqrt{\epsilon_3} \sqrt{1 - \left( \frac{\lambda_3}{1.706 D} \right)^2} \\ &= 1.706 \sqrt{\epsilon_3} \frac{\lambda_3}{\lambda_{\epsilon_3}} \\ &= 1.706 \frac{\lambda}{\lambda_{\epsilon_3}} \end{aligned} \quad (59)$$

where  $\lambda_{\epsilon_3}$  is the guide wavelength in the circular waveguides, as given by Eq. (7) of the text. Combining Eqs. (58) and (59), the characteristic admittance of a thick metal plate perforated by a square array of dielectric-filled circular waveguides is given by Eq. (60):

$$Y_0 = \frac{1.522}{377} \left( \frac{s}{D} \right)^2 \left[ \frac{1 - \left( 0.426 \frac{D}{s} \right)^2}{2J_1' \left( \frac{\pi D}{4s} \right)} \right]^2 \cdot \frac{\lambda}{\lambda_{\epsilon_3}} \quad (60)$$

Equation (16) of the text is obtained from Eq. (60) by replacing the factor 1.522 by the symbol  $C_3$ , and including a factor  $A = 1$  or  $0.5\sqrt{3}$  for the circular waveguides in a square array or a hexagonal array, respectively. It seems somewhat fortuitous that Marcuvitz's formula, which was derived for an air-filled circular waveguide below cut-off, could be extended with any degree of accuracy to apply to a dielectric-filled waveguide propagating the dominant mode. Although the use of Eq. (16) gave good results in calculating the performance of Radomes A and B, it is felt that Eq. (16) should be proven over a wider range of dielectric constants, cavity diameters, and cavity arrangements before it can be used with complete confidence.

## BIBLIOGRAPHY

1. L. A. Robinson and E. M. T. Jones, "Research and Development on the Electrical Properties of Metal Inclusions for Radomes," WADC TR 57-658, Wright Air Development Center, Wright-Patterson Air Force Base, Ohio (May 1958) CONFIDENTIAL.
2. A. von Hippel, "Tables of Dielectric Materials, Vol. V," Technical Report 119, Contract Nonr-1841(10), Laboratory for Insulation Research, Massachusetts Institute of Technology, Cambridge, Massachusetts (April 1957).
3. C. G. Montgomery, *Technique of Microwave Measurements*, p. 301 (McGraw-Hill Book Company, Inc., New York, 1947).
4. N. Marcuvitz, *Waveguide Handbook*, p. 327 (McGraw-Hill Book Company, Inc., New York, N.Y. 1951).
5. G. C. Southworth, *Principles and Applications of Waveguide Transmission*, pp. 124, 125 (D. Van Nostrand Company, Inc., New York, N.Y., 1950).
6. J. Allison and F. A. Benson, "Surface Roughness and Attenuation of Precision Drawn, Chemically Polished, Electropolished, Electroplated, and Electroformed Waveguides," Proceedings of the Institute of Electrical Engineers (London), Vol. 102, Part B, p. 251 (March 1955).
7. S. P. Morgan, "Effect of Surface Roughness on Eddy Current Losses at Microwave Frequencies," *Journal of Applied Physics*, 20, 4, pp. 352-362 (April 1949).
8. E. M. T. Jones and S. B. Cohn, "Two Theorems for Dissipationless Symmetrical Networks," Proceedings of the Institute of Radio Engineers, 45, 7, p. 1016 (July 1957).
9. J. R. Wait, "On the Theory of Reflections from a Wire Grid Parallel to an Interface Between Homogeneous Media," *Applied Scientific Research*, Sec. B, Vol. 6, No. 4, pp. 259-275 (1957).
10. J. R. Wait, "On the Theory of Reflection from a Wire Grid Parallel to an Interface Between Homogeneous Media (II)," *Applied Scientific Research*, Sec. B, Vol. 7, No. 5, pp. 355-360 (1959).
11. L. M. Atlas, "Metal Reinforced Ceramic Radome," WADC TR 58-329, Wright Air Development Center, Wright-Patterson Air Force Base, Ohio (October 1958).
12. S. B. Cohn, "Microwave Coupling by Large Apertures," *Proceedings of the Institute of Radio Engineers* 40, 6 pp. 696-699 (June 1952).
13. H. N. Chait and N. G. Sakiochia, "Broad Band Ferrite Rotators Using Quadruply Ridged Circular Waveguide," *Transactions of the Institute of Radio Engineers*, Vol. MTT-7, No. 1, pp. 38-41 (January 1959).
14. Unpublished communication with J. T. Dorsey of Goodyear Aircraft Corporation, Akron, Ohio.
15. R. C. Honey, L. A. Robinson, and J. K. Shimizu, "Antenna Design Parameters," Quarterly Progress Report 10, SRI Project 1954, Contract DA 36-039 SC-73106, Stanford Research Institute, Menlo Park, California (June 1959).
16. G. G. MacFarlane, "Surface Impedance of an Infinite Parallel-Wire Grid at Oblique Angles of Incidence," *Journal of the Institute of Electrical Engineers (London)*, 93, Part IIIA, pp. 1523-1527 (1946).
17. N. Marcuvitz, *op cit.*, p. 286.
18. W. B. Westphal, *Dielectric Materials and Application*, A. von Hippel ed., Chapter II-A-2, p. 68 (John Wiley and Sons, Inc., New York, 1954).